

**Lakehead University**

**EXPERIMENTAL CHARACTERIZATION OF A HYBRID  
PHOTOVOLTAIC-THERMAL SYSTEM WITH  
REGENERATION**

A Thesis by

Amos Jose

MASTER OF SCIENCE IN MECHANICAL ENGINEERING

Submitted to the Faculty of Graduate Studies in Partial Fulfillment of the  
Requirements for the Master's Degree in Mechanical Engineering

Supervised by

Dr. BASEL I. ISMAIL, P.Eng.

August 2018



**Lakehead**  
UNIVERSITY

## **FACULTY OF GRADUATE STUDIES**

Name of student: Amos Jose

Degree: Master of Science

Academic unit: Mechanical Engineering

Title of thesis: Experimental Characterization of a Hybrid  
Photovoltaic-Thermal System with Regeneration

This thesis has been prepared under my supervision and the candidate has complied with the Master's thesis process regulations.

---

Signature of Supervisor

September 17, 2018

Supervisor's Name: Dr. Basel I. Ismail, P. Eng.

## **Copyright Exceptions**

It is understood that the copyright for the material in this thesis is reserved to the supervisor and author. No parts of this publication may be reproduced, stored in a retrievable system, or transmitted in any form by any means, electronic, mechanical, photocopy, recording, scanning, or otherwise, except as permitted by the main supervisor of this thesis. The non-exclusive right granted to Lakehead University, and moreover, Chancellor Paterson Library to archive the completed work in a publicly available manner does not modify the copyright status.

# Acknowledgment

I thank and glorify God Almighty who strengthens me with his abundant graces and his insights with which he guides me all through my life.

I would like to express sincere gratitude to my supervisor Dr. Basel I. Ismail, P.Eng. Associate Professor and Chair, Mechanical Engineering Department for his full support, expert guidance, understanding and encouragement throughout my study and research. Without his incredible patience and timely wisdom and counsel, my thesis work would have been a frustrating and overwhelming pursuit. Also, I express my appreciation to Dr. Birbal Singh (Mechanical Engineering) and Dr. Leila Pakzad (Chemical Engineering) for having served on my committee. Their thoughtful questions and comments were significantly valued.

I would like to thank Mr. Jawad Hazrat and Mr. Joe Ripku for their guide through the laboratory equipment, devices, and instruments at Lakehead University. I thank Mr. Nicholas Wickman of the Hammarskjold school who helped me with the carpentry works for my research. I thank Ms. Pragati Gupta for her help in some of the measurements during the experimental work.

Last but not least, I express my gratitude to my father Kurian Jose, my mother Elsamma Jose, and my sisters and brothers in law for their unconditional love and support throughout my academics; I would not have been able to complete this thesis without their continuous love, support, and inspiration.

## **Abstract**

Currently, enormous quantities of waste energy are continuously discharged into the earth's atmosphere from various sources. For example, in a photovoltaic panel, about 85% of the incident light is either dissipated as heat or reflected from the PV surface accounting huge losses. Reflection losses in a PV panel can be up to 20% even with antireflection layers inbuilt in them. In order to regenerate some of the optical losses in a photovoltaic system, a new hybrid photovoltaic-thermal system with regeneration (HPVT-Regen) is designed and built in this research. The new HPVT-Regen system design allows the photovoltaic and thermal subsystems to function independently while regenerating some of the optical losses by hybridization. The 3-D designs with complete dimensions of the experiment components were made in CATIA V5. The components were then purchased, fabricated and assembled with required instruments for detailed experimental characterization. Detailed experimentation of the HPVT-Regen system was conducted under indoor lab-scale solar simulator as well as under outdoor solar radiation conditions of Thunder Bay, Ontario. The results showed that the HPVT-Regen system regenerated 14% of the incident light, which was reflected from the PV panel and then converted into electrical as well as thermal energy. From the reflected light, the indoor test set up regenerated approximately 17 mW of electric power under lab simulator lights contributing less than 1% more electric power per unit surface area whereas the outdoor test set up regenerated approximately 137 mW of electric power under solar radiation contributing approximately 3% more electric power per unit surface area. The HPVT-Regen system regenerated 34% more thermal power in both indoor testing as well as in outdoor testing raising approximately 2.7 °C of air temperature solely from the reflected light. This research thesis presents and discusses the design and real-time performance characteristics of the HPVT-Regen system under various real-time operating conditions.

# Table of Contents

<b>LIST OF FIGURES</b>	<b>vii</b>
<b>LIST OF TABLES</b>	<b>xiii</b>
<b>NOMENCLATURE</b>	<b>xiv</b>
<b>CHAPTER 1: INTRODUCTION</b>	<b>1</b>
1.1 The Sun and Energy on Earth	1
1.2 Natural Resources in Canada	1
1.3 Global Energy Consumption: US Energy Information	3
1.4 Solar Radiation on Earth's Surface	7
1.5 Solar Collectors	9
1.5.1 Principles of Solar Thermal Collectors	9
1.6 Solar Photovoltaic (PV) Technology	13
1.6.1 Working Principle of Silicon-based PV Device	13
1.6.2 Characteristics of a Solar Panel	15
1.7 Hybrid Photovoltaic-Thermal Systems (HPVT)	19
1.8 Optical Losses in a PV Panel	21
1.9 Thesis Outline	24
<b>CHAPTER 2: LITERATURE REVIEW</b>	<b>25</b>
2.1 History of PV-T Systems	25
2.2 Experimental Studies in HPVT Systems	26

2.3	Numerical Studies on HPVT Systems	28
2.4	Reflection Losses in a PV Panel	30
2.5	Thesis Research Objectives and Outline	32
<b>CHAPTER 3: DESIGN, CONSTRUCTION, AND ASSEMBLY OF THE HYBRID PHOTOVOLTAIC THERMAL SYSTEM WITH REGENERATION (HPVT-REGEN)</b>		<b>35</b>
3.1	Photovoltaic Subsystem of the HPVT-Regen	35
3.2	Thermal Subsystem of the HPVT-Regen	37
3.3	PV Frame: Supporting Structure	37
3.4	Regeneration Subsystem of the HPVT-Regen	40
3.5	Construction of the Wooden PV Frame	44
3.6	Construction of the Thermal Collector	44
3.7	Instrumentation for Testing HPVT-Regen System	46
3.8	Assembly of the HPVT-Regen System	46
3.9	Solar Simulator	48
3.10	Energy Balance of the HPVT-Regen System	48
3.11	Economics of the HPVT-Regen System	49
<b>CHAPTER 4: INDOOR LABORATORY SIMULATIONS, RESULTS &amp; DISCUSSIONS</b>		<b>52</b>
4.1	Measuring I-V Curves: Kelvin Circuit	52
	4.1.1 Analysis of the Curved-PV Panel	54
	4.1.2 Analysis of the Regen-PV Array	55
4.2	Testing of the Thermal Subsystem	57

4.3	Infrared Analysis of the Irradiated Surfaces	62
4.4	Overall Efficiency of HPVT-Regen System under Solar Simulator Lights	64
	4.9.1 Power Regeneration by HPVT-Regen System	64
<b>CHAPTER 5: OUTDOOR ACTUAL EXPERIMENTAL TEST RESULTS &amp; DISCUSSION</b>		<b>65</b>
5.1	Performance of the Curved-PV Panel	65
5.2	Performance of the Regen-PV Array	68
5.3	Performance of the Thermal Subsystem	70
5.4	Overall Efficiency of the HPVT-Regen System under Solar Radiation	74
	5.4.1 Power Regeneration by HPVT-Regen System	74
5.5	Uncertainty Analysis of the Experimental Results	75
<b>CHAPTER 6: CONCLUSION, FUTURE WORK AND RECOMMENDATIONS</b>		<b>76</b>
6.1	Conclusion	77
6.2	Future Work and Recommendations	78
<b>REFERENCES</b>		<b>80</b>
<b>APPENDIX A: SPECIFICATIONS OF THE PVS &amp; BLACK ABSORBER</b>		<b>A</b>
<b>APPENDIX B: SAMPLE OF WORK PUBLICATION-ICCE2018</b>		<b>B</b>



## List of Figures

Figure 1.1	Solar constant at the entry point of earth's atmosphere measured perpendicular to the radiation.	2
Figure 1.2	Electricity generation in Canada by source, 2011.	2
Figure 1.3	World marketed energy use by fuel type from 1990 to 2035 in quadrillion Btu according to US Energy Information Administration 2010.	4
Figure 1.4	World Energy-related carbon dioxide emissions from 2007 to 2035 in billion metric tons according to US Energy Information Administration 2010.	4
Figure 1.5	World net electricity generation by fuel from 2007 to 2035 in trillion kWh according to US Energy Information Administration 2010.	6
Figure 1.6	World renewable electricity generation by energy source, excluding wind and hydropower, 2007 to 2035 according to US Energy Information Administration 2010.	6
Figure 1.7	Solar spectrum at different Air Mass ratio.	8
Figure 1.8	Components of solar radiation segregated by the atmosphere and earth's surface.	8
Figure 1.9	Exploded view of a flat plate solar collector and absorber details.	10
Figure 1.10	The variation of fluid temperature as the fluid passes through the solar collector distance.	12

Figure 1.11	Classification of solar cells based on the materials of manufacturing.	14
Figure 1.12	Electron-hole separation due to sunlight and the current passing through an external circuit in a solar cell.	14
Figure 1.13	Characteristic curves of a PV showing the parameters governing the performance of the PV.	16
Figure 1.14	The equivalent circuit model of a solar cell showing the current flow through inbuilt resistances of the cell.	16
Figure 1.15	A flat plate hybrid photovoltaic-thermal system with Cu pipes circulating working fluid.	20
Figure 1.16	A concentrating photovoltaic-thermal system employing multiple reflectors to focus light on PV panel coupled with the thermal cooling system.	20
Figure 1.17	Sources of optical losses in a solar cell.	22
Figure 1.18	Destructive interference effect by antireflection coating on PV surface.	22
Figure 1.19	The variation of percent reflection with respect to light wavelength for a Si cell ( $n_2 = 3.8$ ) in air ( $n_1 = 1.9$ ) and under glass ( $n_1 = 2.3$ ).	23
Figure 1.20	Scanning electron microscope image of a textured silicon cell surface for reducing surface reflection.	23
Figure 2.1	Various collector concepts (a) sheet-and-tube, (b) channel PVT, (c) free flow PVT, (d) two-absorber PVT.	27

Figure 2.2	A Trough Concentrating PVT (TCPVT) with Supercell, GaAs and Si cell array at receiver and high reflectivity concentrating mirrors.	27
Figure 2.3	CPVT system with PV panel attached to the thermal unit and facing the parabolic concentrator.	29
Figure 2.4	Finite volume model of the MCPVT system with a PTC and a linear triangular receiver.	29
Figure 2.5	The four-layer encapsulation of a PV module used for optical analysis of reflection losses.	31
Figure 2.6	The relation between total transmittance through PV module and the angle of incidence.	31
Figure 2.7	Research flow chart showing major steps in this thesis.	34
Figure 3.1	Flexible monocrystalline silicon PV panel used for the experimentation.	36
Figure 3.2 a	Isometric view of the steel channel of the thermal system designed in CATIA V5.	38
Figure 3.2 b	Orthographic projections of the steel channel drafted in CATIA.	38
Figure 3.3 a	Isometric view of the wooden structure designed in CATIA V5.	39
Figure 3.3 b	Orthographic and isometric draft of the wooden structure.	39
Figure 3.4	The low rating monocrystalline silicon PV module used for regeneration.	41
Figure 3.5	The assembly of the regen-PVs with the thermal system done in CATIA V5.	41

Figure 3.6	Orthographic projections of the regen system.	42
Figure 3.7 a	The final assembly of the HPVT-Regen system without the instruments.	42
Figure 3.7 b	The final assembly of the HPVT-Regen system showing regen-PV modules facing the curved-PV panel.	43
Figure 3.8	The carpentry stages in the construction of wooden PV frame.	45
Figure 3.9	The thermal collector with Cu absorber around steel channel, regen-PV modules, and air blower.	45
Figure 3.10	The real-time fully instrumented experimental test setup of the HPVT-Regen system.	47
Figure 3.11	The photograph of the complete assembly of the HPVT-Regen system for indoor testing.	47
Figure 3.12	A photograph of the solar simulator with halogen lamps used for the indoor testing.	50
Figure 3.13	Pyranometer reading of the solar irradiation on the horizontal plane of the simulator.	50
Figure 3.14	Energy flow diagram of the HPVT-Regen system used in this research.	51
Figure 4.1	Kelvin Configuration or 4 wire circuit for measuring I-V curves of a solar cell.	53
Figure 4.2	I-V characteristics of the curved-PV panel subsystem under indoor solar simulator.	53
Figure 4.3	I-V characteristics of the regen-PV array tested under the reflected light.	56

Figure 4.4	Thermal image of the thermal collector when only air blower is circulating the air.	58
Figure 4.5	Air temperature gain curve between the inlet and outlet of the thermal collector (a) when only air blower is running, (b) when only radiation is heating the thermocouples.	58
Figure 4.6	Air temperature gain between outlet and inlet of the thermal collector measured on actual running without calibration.	60
Figure 4.7	Compilation of the air temperature gain curves obtained in indoor testing showing the calibration.	60
Figure 4.8	Actual air temperature gain under simulator lights after calibration.	61
Figure 4.9	Air temperature gain contributed solely by the reflected light in indoor testing.	61
Figure 4.10a	Infrared image of the top black surface captured with FLIR IR camera calibrated for the surface emissivity for indoor testing.	63
Figure 4.10b	Infrared image of bottom regen-PV array captured with FLIR IR camera calibrated for silicon surface emissivity for indoor testing.	63
Figure 5.1	A photograph of the fully instrumented test set up under solar radiation in Thunder Bay, Ontario.	66
Figure 5.2	Variation in maximum power of the curved-PV panel with respect to solar radiation.	66
Figure 5.3	I-V characteristics of the curved-PV panel for the instant of highest maximum power obtained, measured by Solmetric PVA-600V PV-Analyzer.	67
Figure 5.4	I-V characteristics of the regen-PV array obtained while testing under outdoor solar radiation.	69

Figure 5.5	Compilation of the air temperature gain curves obtained in outdoor testing showing the calibration.	71
Figure 5.6	Actual air temperature gain after calibration obtained in outdoor testing.	71
Figure 5.7	Air temperature gain solely due to reflected light obtained in outdoor testing.	72
Figure 5.8	Thermal images of the top (left) and bottom (right) surfaces of the thermal collector taken with FLIR camera for outdoor simulation.	72
Figure 6.1	Schematic of a concept of combining HPVT-Regen system with a Rankine cycle for preheating the working fluid.	79
Figure A.1	Specifications of the flexible PV panel used in this research.	A-1
Figure A.2	Specifications of the regen-PV panel used in this research.	A-2
Figure A.3	Specifications of the black Cu absorber used in this research.	A-3

## List of Tables

Table 3.1	Specification of the flexible monocrystalline PV panel.	35
Table 3.2	Thermal properties of the materials of thermal subsystem.	37
Table 3.3	Dimensions of the thermal subsystem.	37
Table 3.4	The specifications of the regenerating PV modules.	40
Table 3.5	Total expenditure of the HPVT-Regen system research.	49
Table 5.1	Irradiation and performance parameters of the curved-PV panel measured by Solmetric PVA-600V PV Analyzer.	67
Table 5.2	Comparison of performance parameters of the electrical subsystem of the HPVT-Regen system for indoor and outdoor testing.	69
Table 5.3	Comparison of performance parameters of the thermal subsystem of the HPVT-Regen system for indoor and outdoor testing.	73
Table 5.4	Uncertainty of experimentally measured and calculated parameters of the HPVT-Regen simulation.	76

# Nomenclature

## Greek

$\alpha$	Angle of incidence ( $^{\circ}$ )
$\alpha_t$	Thermal absorptivity (%)
$\gamma$	Optical efficiency (%)
$\varepsilon$	Thermal Emissivity (%)
$\eta$	Efficiency (%)
$\lambda$	Wavelength ( $nm$ )
$\tau$	Optical transmittance (%)
$\mu$	Uncertainty
$\sigma$	Boltzmann constant ( $W/m^2K^4$ )

## Latin

$A$	Area ( $m^2$ )
$C_p$	Specific heat capacity ( $J/Kg.K$ )
$F$	Thermal collector efficiency factor
$FF$	Fill factor
$I$	Current ( $A$ )
$L$	Total thermal collector distance ( $m$ )
$LMTD$	Logarithmic mean temperature difference ( $^{\circ}C$ )
$N$	Number of measurements
$P$	Power ( $W$ )
$R$	Electrical resistance ( $\Omega$ )
$\bar{R}$	Mean optical reflectance ( $^{\circ}$ )
$T$	Temperature ( $^{\circ}C$ )
$U$	Heat loss coefficient ( $W/m^2K$ )
$V$	Voltage ( $V$ )
$a_r$	Angular optical loss coefficient



$d$	Thickness of layer ( $m$ )
$e$	Electron current ( $A$ )
$k$	Boltzmann's constant ( $eV/K$ )
$k_t$	Thermal conductivity ( $W/mK$ )
$\dot{m}$	Mass flow rate ( $Kg/s$ )
$n$	Refractive index
$q$	Heat transfer per unit area ( $W/m^2$ )
$r$	Optical reflection (%)
$z$	Ideality factor of a solar cell

# Chapter 1: Introduction

## 1.1 The Sun and Energy on Earth

The sun is the source of all energy that keeps every inhabitant on earth moving and functioning. Plants convert soil fertile into carbohydrates during photosynthesis with the help of solar energy. Animals rely on plants for food, makeup and maintain the food chain. Fossil fuels on earth are converted naturally from vast plant and animal matter existed in the geological age. Air heated by the sun generates wind that is converted into electricity by wind turbines. Flowing water contributed by rain which is because of evaporation are used to generate hydropower.

The surface of the sun or photosphere is at an average temperature of 5777 K and approximates a blackbody. The sun emits electromagnetic radiation of about  $63 \times 10^6$  W/m<sup>2</sup> according to the Stefan-Boltzmann equation of radiation. The solar constant is the solar radiation per unit area incident on a plane perpendicular to the rays, at a distance of one astronomical unit from the sun (shown in **Figure 1.1**). This extraterrestrial radiation varies with the sun-earth distance within the range of  $\pm 3.3\%$  due to the eccentricity of the earth's orbit and due to tilt of the earth. The World Radiation Center (WRC) has adopted a value of 1367 W/m<sup>2</sup> as solar constant with an uncertainty of 1% [1].

## 1.2 Natural Resources in Canada

Canada is the fifth largest energy producer and eighth largest energy consumer. Significant nonrenewable energy resources in Canada are oil, natural gas, coal, and uranium. Renewable energy resources include hydroelectricity, solar, wind, tidal and biomass. Canada has about 1% of the world's coal resources, 178 billion barrels of crude oil, 58 trillion cubic feet of natural gas as of 2006. Eight percent of the world's unmined uranium resources are reserved in Canada [2]. Renewable energy represents 17% of Canada's total primary energy supply. Hydroelectricity is the most abundant renewable energy supply with 60% of Canada's electricity generation. Resources such as biomass, wind, tidal, and solar contribute 3% of electricity generation (**Figure 1.2**). Over the total electricity generation in Canada, 77% of it does not emit greenhouse gases [3].

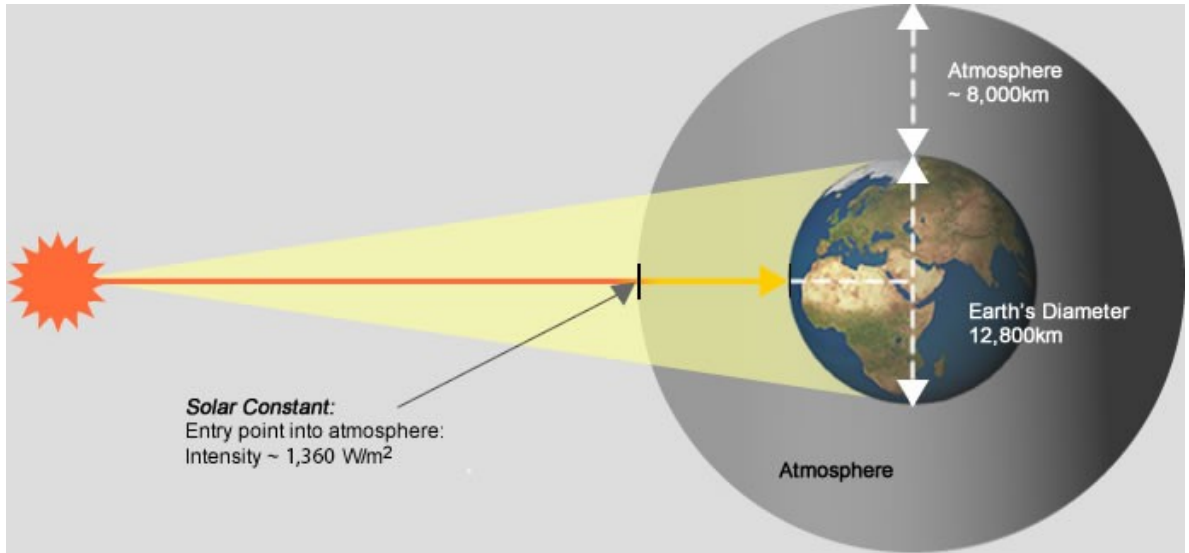


Figure 1.1 Solar constant at the entry point of earth's atmosphere measured perpendicular to the radiation [4].

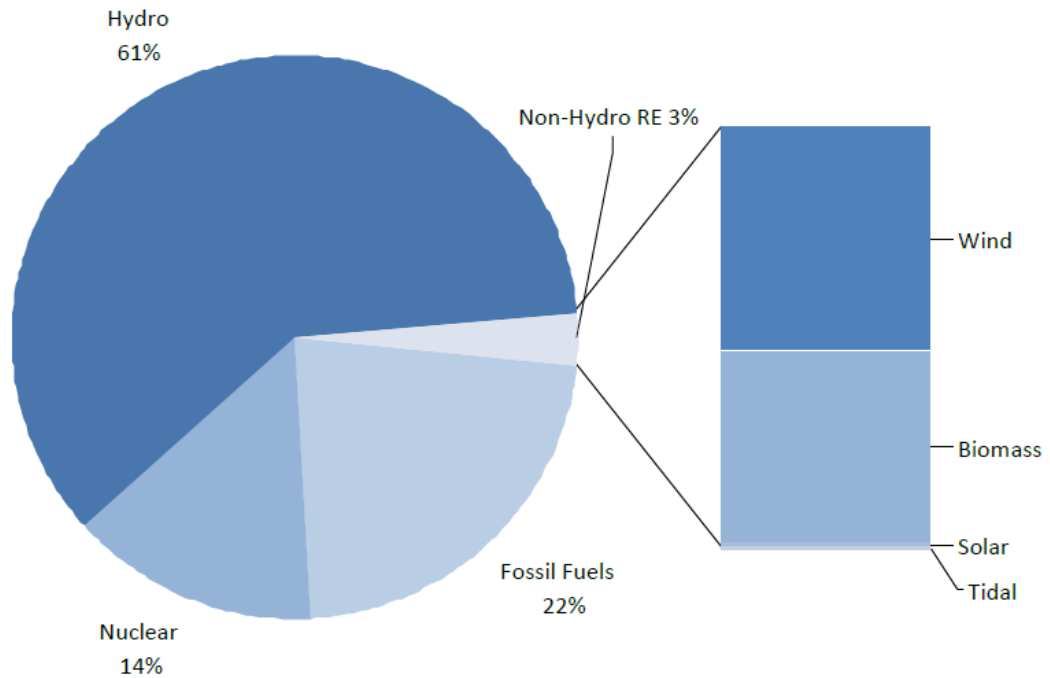


Figure 1.2: Electricity generation in Canada by source, 2011 [3].

### **1.3 Global Energy Consumption: US Energy Information**

According to US Energy Information Administration 2010 report in International Energy Outlook (IEO2010), world marketed energy consumption increases by 49 percent from 2007 to 2035. The IEO 2010 reports that the industrial sector uses more energy globally about 50% of the world's total delivered energy. Various industrial sectors like manufacturing, agriculture, mining, and construction utilize energy for activities like processing and assembly, space conditioning, and lightning. IEO2010 predicts an industrial energy consumption from 184 quadrillion Btu in 2007 to 262 quadrillion Btu in 2035. Transportation consumes almost 30% of the world's total delivered energy. Increase in urbanization and personal incomes have contributed to increases in air travel and motorization. Residential and commercial consumers in the building sector accounted for one-fifth of the world's total delivered energy consumption excluding transportation costs. The energy consumption in building sector varies from countries depending on weather, appliances size of the building and associated heating, lighting and air conditioning. The world marketed energy use by fuel type is shown in **Figure 1.3** [5].

#### ***World carbon dioxide emissions***

The IEO2010 report projects an increase of 43% in carbon dioxide emission from 2007 to 2035. The estimated emission increases from 29.7 billion metric tons in 2007 to 33.8 billion metric tons in 2020 and 42.4 billion metric tons in 2035. The report shows exceeded emission in developing non-OECD<sup>1</sup> nations than OECD nations by 17%. The world energy-related carbon dioxide emissions in billion metric tons are shown in **Figure 1.4**. Carbon dioxide emissions vary by fuel types, with coal has the highest carbon intensity followed by oil and natural gas. Nuclear and most renewable energy sources do not generate carbon dioxide emissions [5].

<sup>1</sup>**OECD: Organization for Economic Cooperation and Development**, which includes US, Canada, Mexico, Austria, Belgium, Czech Republic, Denmark, Finland, France, Germany, Greece, Hungary, Iceland, Italy, Luxembourg, Netherlands, Norway, Poland, Portugal, Slovakia, Spain, Switzerland, Turkey, UK, Japan, South Korea, Australia, and New Zealand.

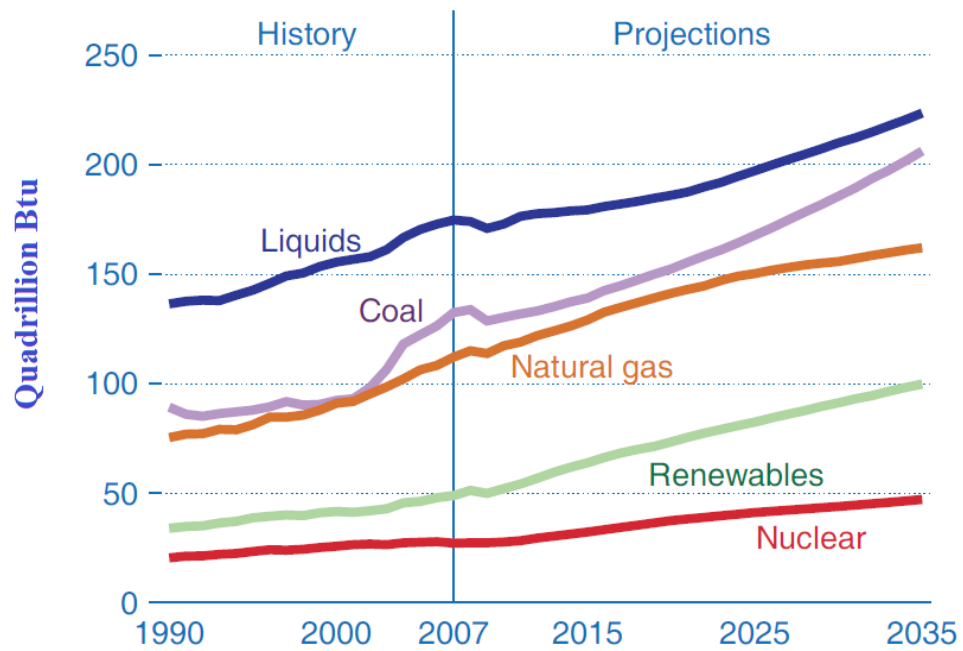


Figure 1.3: World marketed energy use by fuel type from 1990 to 2035 in quadrillion Btu according to US Energy Information Administration 2010 [5].

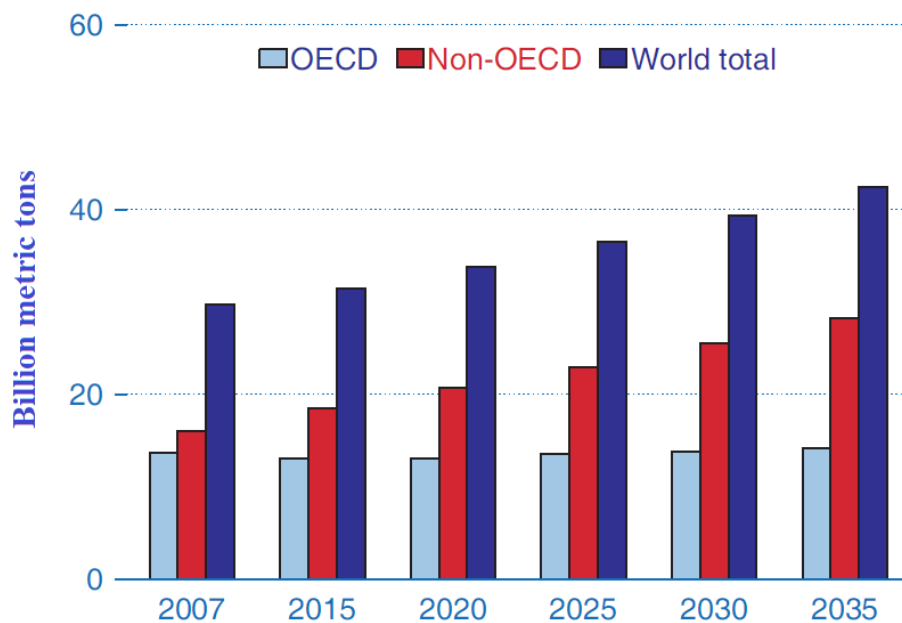


Figure 1.4: World Energy-related carbon dioxide emissions from 2007 to 2035 in billion metric tons according to US Energy Information Administration 2010 [5].

## ***Renewable Energy Consumption***

As per US Energy Information Administration 2010, industrial sectors use a substantial amount of renewable energy (excludes consumption of ‘electricity’ generated from renewable energy sources). Industrial sector used about 7% of total delivered energy from renewable sources in 2007. IEO 2010 predicts an increase in renewable energy consumption from 1.8% a year in 2007 to 8% a year in 2035. Biomass contributes ninety percent of the renewable energy consumed in the industrial sector and is expected to remain as the primary contributor until 2035. Increase in energy price and concerns about environmental consequences like greenhouse gas emissions and climate change leads to interest in alternative sources like renewable and nuclear power sources.

IEO2010 predicts that the world renewable energy use for electricity generation grows by an average of 3% per year reaching 4.5 trillion kilowatt hours from 2007 to 2035 as shown in **Figure 1.5**. Hydroelectric and wind power are the highest contributors to renewable electricity generation with 54% increase by hydroelectric power and 26% increase by wind power. Other renewable energy sources for electricity like solar, geothermal, biomass, waste, and tidal are not economically competitive with fossil fuels. **Figure 1.6** projects the contribution of biomass, solar and geothermal sources in electricity generation from 2007 to 2035 [5].

Energy sources like wind and solar can be used only when the resources are available. The cost of operation is much less after the initial construction cost compared to the conventional renewable sources like biomass and geothermal. Tidal and wave power generators have enough potential but are not efficient due to continuous variations in tides within the day and over seasons. Biomass systems have similar technological aspects to fossil fuels but are less efficient and involves several chemical treatments which causes quick degradation of metallic parts, chemical wastes. The biomass combustion conditions are poor with non-uniform burning with rough explosive sounds. Geothermal systems use extremely hot water from deep wells that can be used to produce steam to run a turbine. However, the geothermal sources are limited to areas that can be reached economically with drilling equipment [6].

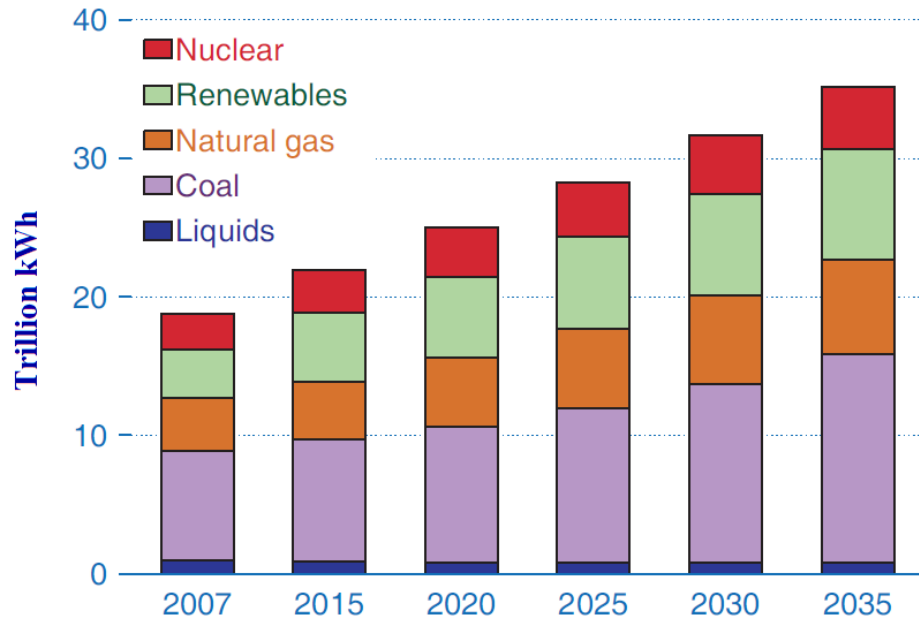


Figure 1.5: World net electricity generation by fuel from 2007 to 2035 in trillion kWh according to US Energy Information Administration 2010 [5].

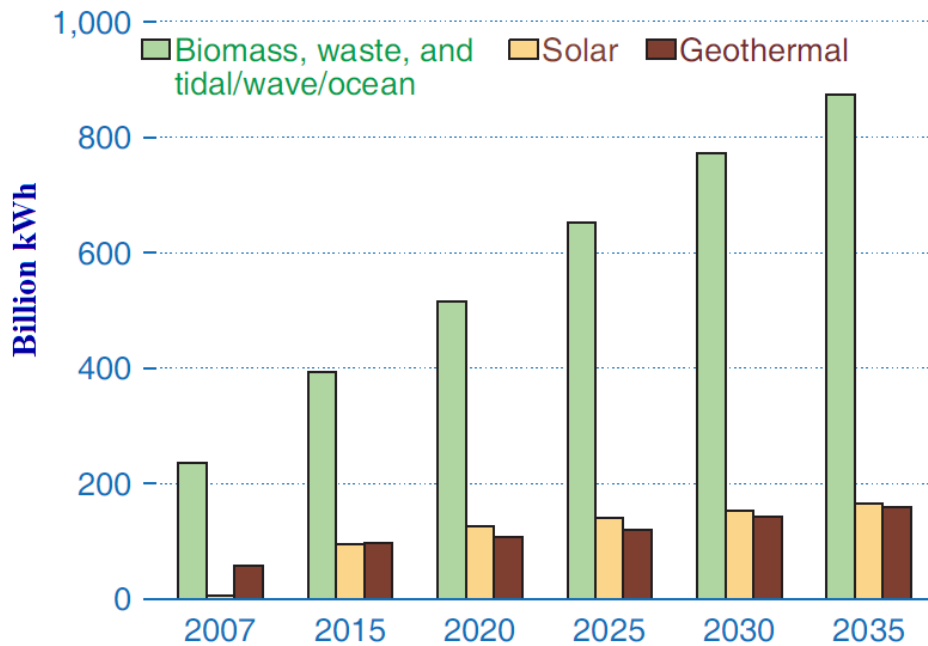


Figure 1.6: World renewable electricity generation by energy source, excluding wind and hydropower, 2007 to 2035 according to US Energy Information Administration 2010 [5].

## 1.4 Solar Radiation on Earth's Surface

On the surface of the earth, the spectral distribution of solar irradiance changes from extraterrestrial spectral distribution as the radiation travels through the atmosphere (shown in **Figure 1.7**). As solar radiation passes through the atmosphere, gases, dust, and aerosols absorb radiations in the range of their bond energies. Water vapor and CO<sub>2</sub> absorb far infrared radiations above 2 $\mu$ m. Ozone (O<sub>3</sub>) absorb most of UV light below 0.3 $\mu$ m. Absorption by gases and water vapor does not reduce the solar power dramatically, but absorption and scattering due to air molecules and dust cause a significant reduction in power [7].

The sun can be treated as a quasi-point source since the intensity of solar radiation varies throughout the year by  $\pm 3.4\%$  because of eccentricity of the earth's elliptical orbit. As the quasi-collimated beam from sun traverses through the atmosphere, scattered photons produce the "diffused sky radiation" often represented by "D" and the remaining unabsorbed and unscattered photons produce "direct beam radiation" ("B"). The total radiation flux on a horizontal surface combining diffused and direct beam radiation is called "total" or "global" radiation ("G"). The earth reflects about 29% of the incident radiation, thus on a tilted surface, additional reflected radiation (Albedo) is received and is called "global tilted" radiation [8]. **Figure 1.8** shows the components of solar radiation on earth's atmosphere.

A Pyrheliometer measures direct solar radiation flux at normal incidence using various radiation sensors based on calorimetric, thermomechanical, thermoelectric and photoelectric principles. The global solar radiation is measured with radiometers with hemispherical fields of view, called Pyranometers. The sensing elements used in a pyranometer are same as those in pyrheliometer except that the sensing elements are flat surface unlike conical absorbers in pyrheliometers. Pyranometer has a sensitivity range between 0.4 and 1.1 $\mu$ m. Ground reflected albedo is determined by employing two horizontally placed identical pyranometers one facing the sky and the other facing the ground [9].



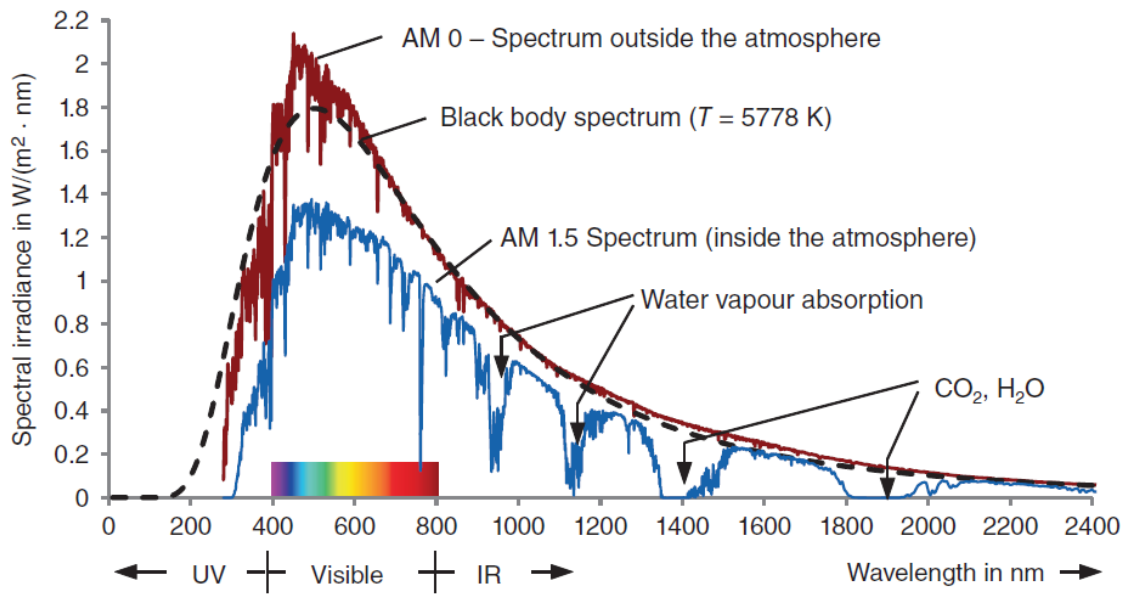


Figure 1.7: Solar spectrum at different Air Mass ratio. The graph shows the wavelengths absorbed by various gases and water vapor corresponding to their bond energy [10].

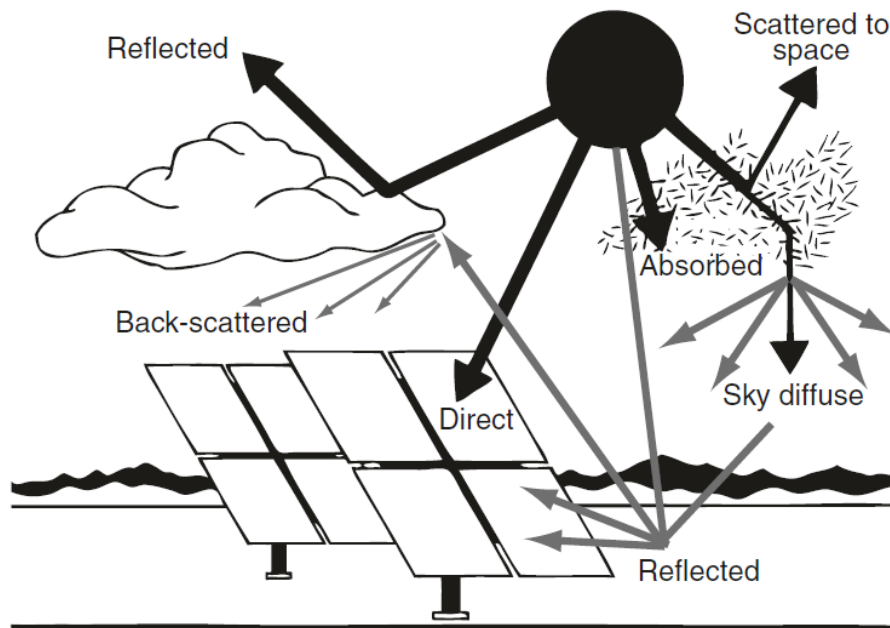


Figure 1.8: Components of solar radiation segregated by the atmosphere and earth's surface [8].

## 1.5 Solar Collectors

Solar collectors are an excellent method of utilizing solar energy coming on the earth. Solar thermal systems are non-polluting and environment-friendly. Solar collectors are heat exchangers that receive solar radiation, converts to heat, and transfers to the internal energy of a flowing medium such as air, water, and oil. The solar energy can be utilized instantaneously for heating water or space or stored in thermal energy storage tanks [11]. There are two types of solar collectors: non-concentrating or stationary and concentrating. A stationary collector has a constant area for intercepting and absorbing solar radiation, whereas a sun-tracking concentrating solar collector has concave reflecting surfaces to intercept and focus the sun's beam radiation to a smaller receiving area and multiplying the radiation flux.

An energy-efficient solar collector should absorb impinging radiation, convert it to thermal energy, and transfer to a working fluid with minimum losses at each step. The collector must absorb as much solar energy as possible at the lowest possible cost and must have a long life. This optimization requires efficient design and quality material. **Figure 1.9** depicts a Flat Plate Solar Collector with details of absorber [12].

### 1.5.1 Principles of Solar Thermal Collectors

R.H.B. Exell gives simplified governing equations of a flat plate solar collector that is considered performing thermal conversions as a heat exchanger. The flat plate solar collector has a selective black plate assumed to be at a uniform temperature,  $T_b$ , single optical efficiency  $\gamma$ , and heat loss coefficient  $U$ . Then the heat extracted per unit area is related to the solar heat input by the equation [13],

$$q_{out} = \gamma q_{in} - U(T_b - T_a) \quad (1.1)$$

where  $T_a$  is the ambient temperature. In practical applications instead of the black plate temperature, mean fluid temperature  $T_f$  is more convenient. Considering a collector area,  $A$ , the total heat extraction rate is given by,

$$Q_{out} = AF[\gamma q_{in} - U(T_f - T_a)] \quad (1.2)$$

where  $F$  is the collector efficiency factor. It must be close to one for good designs.

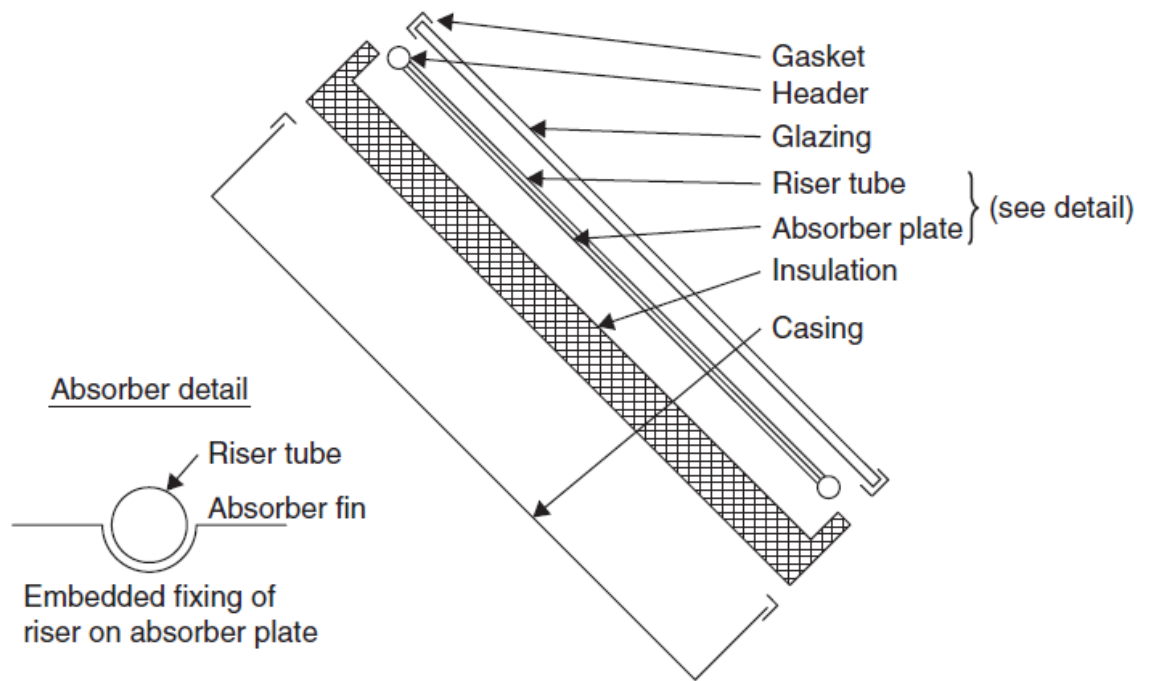


Figure 1.9: Exploded view of a flat plate solar collector and absorber details [12].

When the fluid reaches stagnation temperature, the heat extracted from the collector is zero ( $Q_{out}$ ). Thus, the maximum fluid temperature is given by (from equation 1.1)

$$T_{max} = T_a + \frac{\gamma q_{in}}{U} \quad (1.3)$$

When the fluid has a mass flow rate,  $\dot{m}$  and specific heat capacity,  $C$  flowing through a total collector distance of  $L$  across the area  $A$ , the heating of the fluid at an arbitrary location,  $x$  is given by a first order non-homogeneous linear differential equation,

$$\dot{m}C \frac{dT_f(x)}{dx} = \frac{AF}{L} [\gamma q_{in} - U(T_f(x) - T_a)] \quad (1.4)$$

The solution to the above equation gives the relation between the inlet ( $x = 0$ ) and outlet fluid ( $x = L$ ) temperatures,

$$[\gamma q_{in} - U(T_{in} - T_a)] \exp\left(\frac{-AFU}{\dot{m}C}\right) = [\gamma q_{in} - U(T_{out} - T_a)] \quad (1.5)$$

Based on the inlet and outlet temperature, the heat extracted from the collector is given by

$$Q_{out} = \dot{m}C(T_{out} - T_{in}) \quad (1.6)$$

Substituting the boundary condition of maximum fluid temperature at stagnation fluid temperature given by equations 1.3 and 1.5 in equation 1.6, the heat extracted from the solar collector is given by

$$Q_{out} = AFU \times LMTD \quad (1.7)$$

where  $A$  is the cross-sectional area of the collector,  $F$  is the collector efficiency factor, and  $LMTD$  is the logarithmic mean temperature difference.

$$LMTD = \frac{(T_{out} - T_{in})}{\ln(T_{max} - T_{out}) - \ln(T_{max} - T_{in})} \quad (1.8)$$

This equation validates that a solar collector can be considered as a heat exchanger. The graph showing the variation of fluid temperature across the distance of the solar collector is given in the **Figure 1.10** [13].

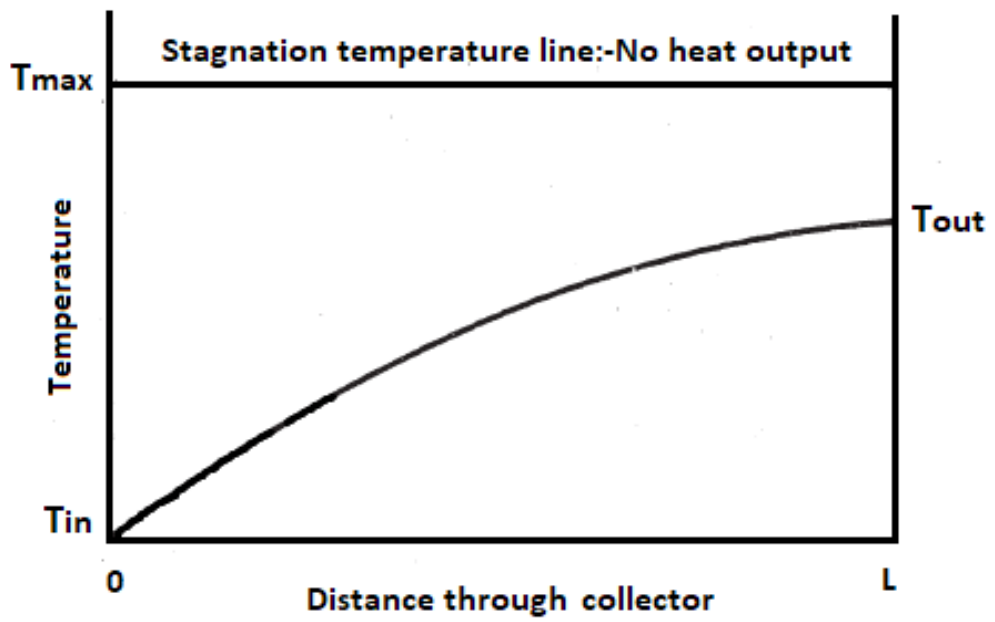


Figure 1.10: The variation of fluid temperature as the fluid passes through the solar collector distance [13].

## 1.6 Solar Photovoltaic (PV) Technology

The history of photovoltaic technology begins from 1839 when Becquerel observed photocurrents while illuminating platinum electrodes coated with silver halide. In 1873 Smith observed photoconductivity in solid selenium followed by in 1877, Adams and Day discovered photovoltaic effect in a selenium rod sealed with platinum contacts. In 1883, Fritts made the first practical PV device, a light meter. The light meter was made of a thin layer of selenium sandwiched between an iron base plate and a semi-transparent gold top layer. In 1885, the German industrialist Werner von Siemens promoted the light meter and demonstrated the direct conversion of light into electricity for the first time [14].

Based on the material, photovoltaic technology is classified into Crystalline, Thin Film, and Nanotechnology. The 1<sup>st</sup> generation PV modules are made of mono and polycrystalline silicon structures which are still being improved in its capability and efficiency. The 2<sup>nd</sup> generation PV have multiple junctions and thinner layers to reduce material cost and space while maintaining and achieving higher efficiencies. The 3<sup>rd</sup> generation PV have double and triple crystalline III-V compounds and nanomaterials [15]. The classification of photovoltaic technology based on materials is shown in **Figure 1.11**.

### 1.6.1 Working Principle of Silicon-Based PV Device

PV cells are semiconductor devices with P-N junctions which can directly convert sunlight into electricity through the photovoltaic effect. An electron from the valence shell of the atom is released by ionization process when sunlight with photons of energy above the threshold energy of the PV bandgap falls on the P-N junction. The ionization process creates an internal electrical field at the P-N junction. This electrical field separates electron-hole pairs drifting holes towards P side and electrons towards N side. Because of the internal electrical field at the P-N junction, these electrons can recombine only through an external circuit providing a useful electrical work [16] (**Figure 1.12**). “Stand-alone” and “grid-connected” systems are the basic types of PV application. Stand-alone systems are implemented in remote areas that are not powered by electricity line. The energy produced is stored in batteries for non-productive times. A grid-connected system works with electricity supply line that can provide power during non-productive times [17].

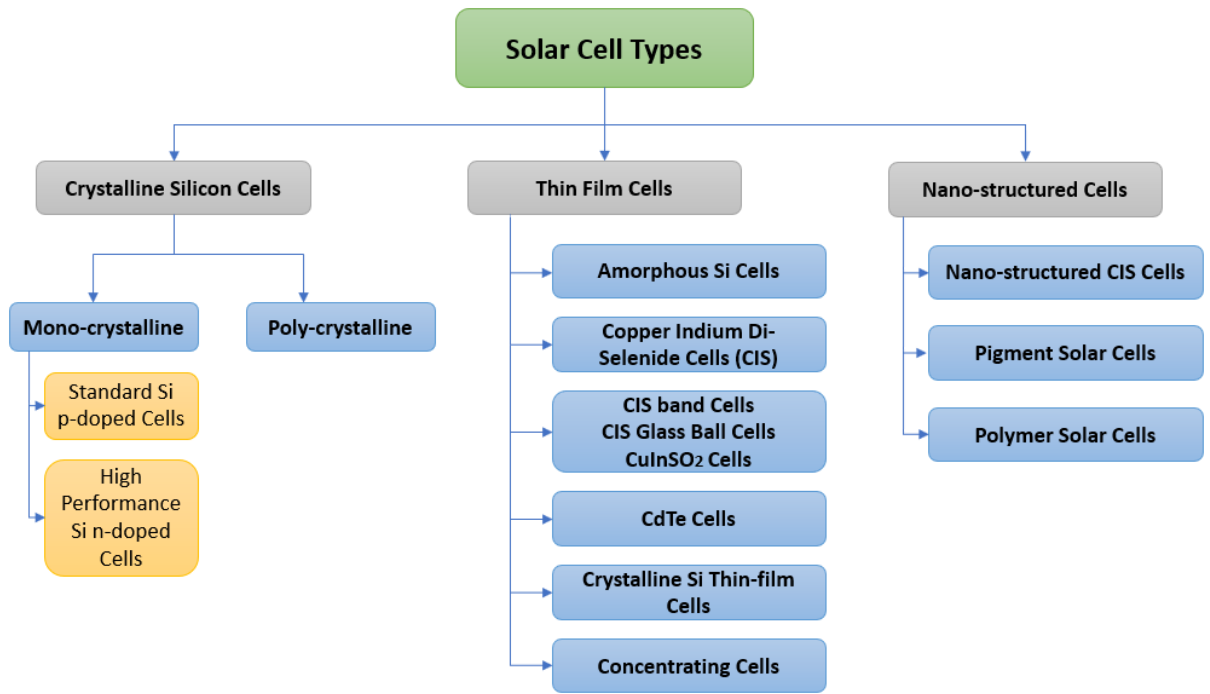


Figure 1.11: Classification of solar cells based on the materials of manufacturing [18].

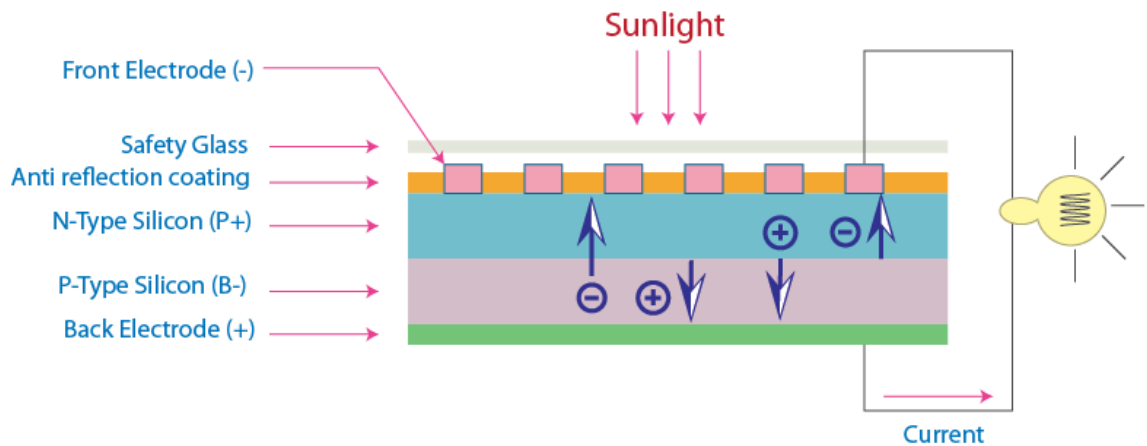


Figure 1.12: Electron-hole separation due to sunlight and the current passing through an external circuit in a solar cell [19].

## 1.6.2 Characteristics of a Solar Panel

Characteristics of a solar panel are described by specific parameters of the PV such as open-circuit voltage, short-circuit current, fill factor, and maximum power point. **Figure 1.13** shows an I-V characteristic together with the power curves. The PV power output varies with irradiation and temperature conditions and uses a Standard Testing Conditions (STC) for the measurement of the panel. The STCs are using a light intensity equivalent to  $1000 \text{ Wm}^{-2}$ , a spectral content corresponding to the standard AM1.5 global spectrum (refer figure 1.7) and an operating temperature of  $25 \text{ }^\circ\text{C}$  [20].

To maximize the power rating, a solar cell must be designed in such a way that the p-n junction should absorb most of the incident solar radiation. According to the diode law, the current generated from a diode upon illumination is [21],

$$I_D = I_0 \left[ \exp\left(\frac{eV}{zkT}\right) - 1 \right] \quad (1.9)$$

where  $I$  is the current,  $I_0$  is the dark saturation current (the diode leakage current density in the absence of light),  $V$  is the voltage,  $e$  is the charge on an electron,  $k$  is the Boltzmann's constant ( $8.61 \times 10^{-15} \text{ eV/K}$ ),  $z$  is the ideality factor; typically between 1 and 2, and  $T$  is the absolute temperature [21].

**Figure 1.14** shows a simplified equivalent circuit model of a real solar cell. The series resistance ( $R_s$ ) and shunt resistance ( $R_{sh}$ ) are associated with a solar cell that reduces the fill factor of the cell. Series resistance is the bulk resistance of the semiconductor material, the metallic contacts, interconnections, carrier transport through the diffused layer, and the contacts between the metallic surfaces and the semiconductor. The shunt resistance is due to p-n junction non-idealities and impurities near the junction [21]. From the circuit shown in figure 1.14, the net current generated by the solar cell (modules or array) is given by

$$I = I_L - I_D - I_{sh} \quad (1.10)$$

The shunt current from the circuit,

$$I_{sh} = \left[ \frac{V + IR_s}{R_{sh}} \right] \quad (1.11)$$



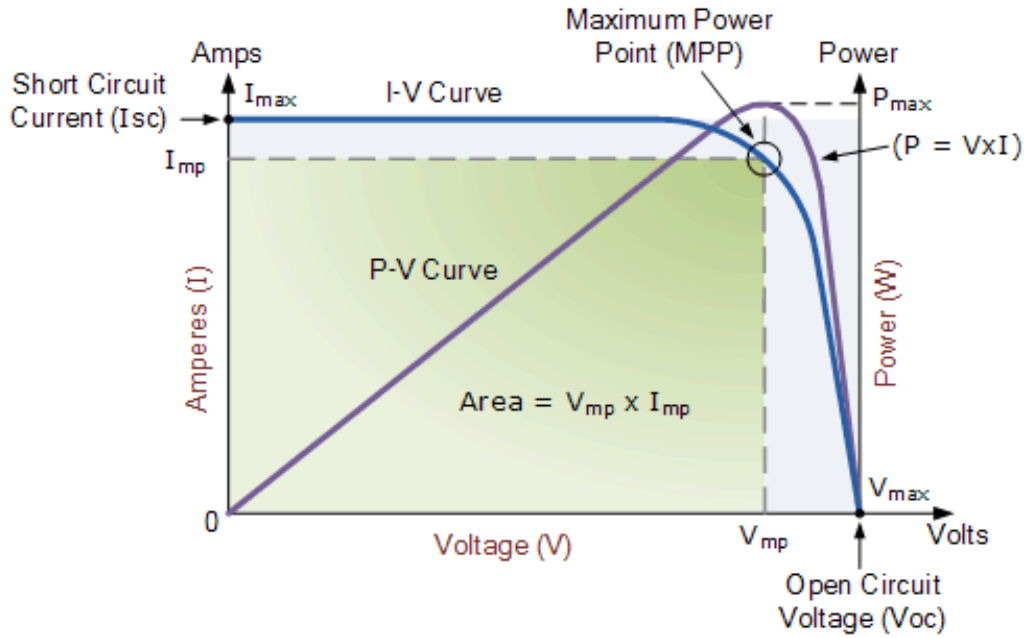


Figure 1.13: Characteristic curves of a PV showing the parameters governing the performance of the PV [7].

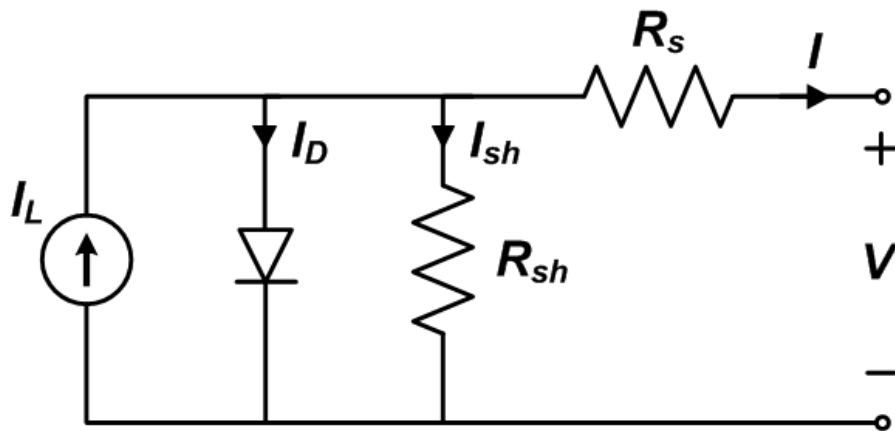


Figure 1.14: The equivalent circuit model of a solar cell showing the current flow through inbuilt resistances of the cell [21].

Substituting equations 1.9 and 1.11 in to equation 1.11, and adding the voltage across the series resistance in the diode current term, the equation for the net current obtained in the circuit is as follows [22],

$$I = I_L - I_0 \left[ \exp\left(\frac{V + IR_s}{z k T / e}\right) - 1 \right] - \left[ \frac{V + IR_s}{R_{sh}} \right] \quad (1.12)$$

where,  $I_L$  is the light generated current.

When the circuit is short-circuited, the external load is minimum (resistance of the wire), and the voltage drop across the solar cell is nearly zero and the current obtained is called **short-circuit current**,  $I_{SC}$ . The short circuit current indicates the maximum current the solar cell can deliver under given conditions of irradiation and cell temperature. Also, short-circuit current is directly proportional to the incident light and is assumed to be approximately equal to the light generated current from the p-n junction of the cell [23],  $I_{SC} = I_L$ .

The point where the I-V curve crosses the voltage axis gives the **open circuit voltage**,  $V_{OC}$  which is when the circuit is connected to no-load. Open circuit voltage indicates the maximum voltage the solar cell can deliver under given conditions of irradiation and cell temperature [24]. Since there is no load connected, the current through the series resistance is zero and the third term in equation 1.12 disappears. Deriving the open circuit voltage from equation 1.12 gives [23],

$$V_{OC} = \frac{z k T}{e} \ln \left[ \frac{I_L}{I_0} + 1 \right] \quad (1.13)$$

The power output is the product of the current and voltage delivered by the solar cell. The **maximum power point** (peak power) is one of the characteristics of a solar cell and is graphically obtained by the largest rectangle that fits under the I-V curve. The voltage and current at peak power are called voltage at maximum power ( $V_{mp}$ ) and current at maximum power ( $I_{mp}$ ) respectively [24].

$$P_{max} = V_{mp} I_{mp} \quad (1.14)$$

At short and open circuit, the power is zero as there is no load connected. The power varies with the load, and the peak power gives information about the best electrical load match for the solar cell under given conditions of irradiation and cell temperature [24].

**Fill Factor, FF** is a factor considered in the design of solar cells which determines the capacity of the solar cells in producing the maximum possible power by compensating between the short-circuit current and open-circuit voltage. The FF can be calculated based on experimental results using the following mathematical expression [25]

$$FF = \frac{V_{mp}I_{mp}}{V_{oc}I_{sc}} \quad (1.15)$$

Many scientists and engineers have come up with empirical relation for the fill factor based on the material properties of a PV module. Among various approximate solutions, the most accurate empirical formula for the fill factor is given by Green Martin as follows [26]

$$FF = \frac{\frac{eV_{oc}}{zkT} - \ln \left[ 0.72 + \frac{eV_{oc}}{zkT} \right]}{\frac{eV_{oc}}{zkT} + 1} \quad (1.16)$$

The leading figure of merit in the characterization of a solar cell is the **maximum power conversion efficiency** which is the ratio of the maximum electrical power supplied by the solar cell to the incoming photon energy [26].

$$\eta = \frac{P_{max}}{P_{in}} = \frac{FFV_{oc}I_{sc}}{P_{in}} \quad (1.17)$$

A high-efficiency solar cell requires a high short-circuit current, a high open-circuit voltage, and a fill factor closer to 1. The overall conversion efficiency of the cell also depends on the p-n junction efficiency, electric contact efficiency, light absorption efficiency, and light reflection efficiency.

The junction efficiency depends on the junction geometry, dimension, and junction materials. A higher junction efficiency reduces recombination losses in the device. A higher contact efficiency reduces the contact losses. Low resistance contacts can yield contact efficiency in the range of 97 to 98%. Proper doping and manufacturing play a key role in obtaining a higher absorption efficiency [23], [27].

## 1.7 Hybrid Photovoltaic-Thermal Systems (HPVT)

A Hybrid PV-T collector is a combination of photovoltaic (PV) and thermal (T) components that enable to produce both electricity as well as heat simultaneously. HPVT systems produce more energy per unit surface area than side-by-side PV modules and thermal collectors working independently [28]. Although PV modules convert sunlight directly into electricity, most of the absorbed solar radiation is unused and dissipated to the PV modules as waste heat. The heat generated can be transferred to a heat exchanger in thermal contact with PV modules to meet some heating demand [29]. Solar radiation that cannot be converted into electricity raises the temperature of the PV modules, causing a decrease in their electrical efficiency. For monocrystalline and polycrystalline Si cells, the efficiency decreases by about 0.45% for every single degree rise in temperature [30]. Thus, employing a thermal system to heat a working fluid like air or water cools the PV while absorbing waste heat. The simultaneous cooling of the PV modules helps maintain electrical efficiency at a satisfactory level, and thus the HPV-T systems offer a better way of utilizing solar energy with higher overall efficiency [31].

HPV-T systems are mainly classified as “Flat plate PV-T collectors” and “Concentrating PV-T collectors.” Flat plate PV-T collectors looks very similar to a flat plate thermal collector where PV panels are attached on top of the metallic absorber plate. The absorber plate is equipped with tubes circulating working fluid such as water or air as shown in **Figure 1.15** [32]. Integrating flat plate PV and thermal collector reduces the production and installation cost and is quite suitable for building rooftop and façade. Since solar cells are not an efficient thermal absorber, flat plate PV-T systems generate low-temperature heat that is considered just as a byproduct of cooling the solar cells [33].

In concentrating PV-T collectors, solar radiation concentration devices such as lenses and mirrors are incorporated to intensify radiations impinging on PV so that inexpensive mirror can replace a (large) part of the expensive PV area. Concentrating photovoltaics present higher efficiency than the typical ones, coupling suitable thermal systems to PV help maintain the module temperature as low as possible while generating usable heat [34]. **Figure 1.16** shows a concentrating photovoltaic-thermal system employing multiple reflectors to focus light on PV panel coupled with the thermal cooling system.

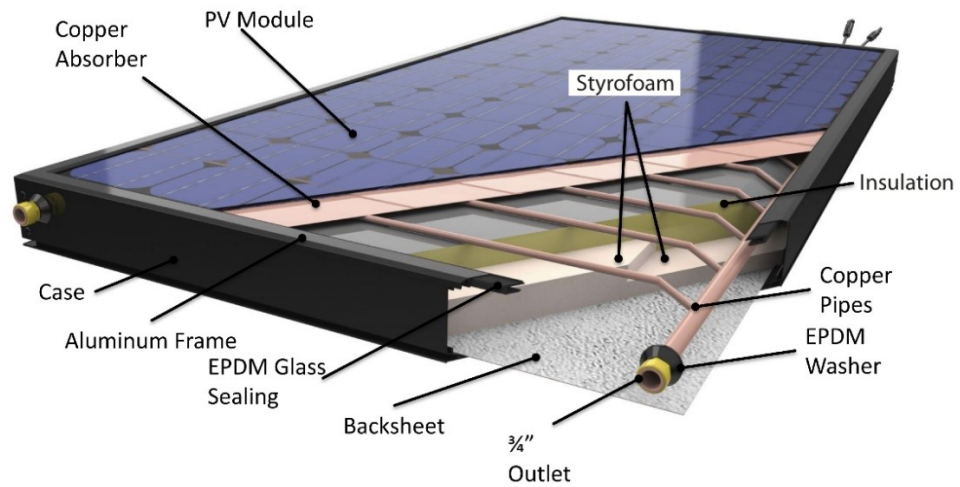


Figure 1.15: A flat plate hybrid photovoltaic-thermal system with Cu pipes circulating working fluid [35].

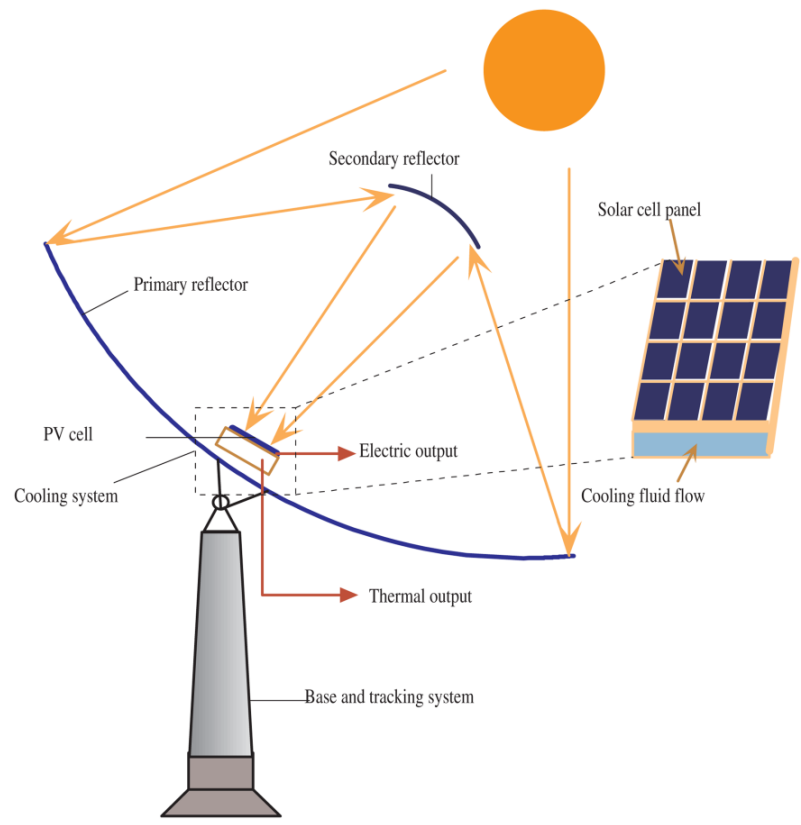


Figure 1.16: A concentrating photovoltaic-thermal system employing multiple reflectors to focus light on PV panel coupled with the thermal cooling system [36].

## 1.8 Optical Losses in a PV Panel

The sources of optical losses in a solar cell are mainly three types (**Figure 1.17**),

- a) Blocking by top contact,
- b) Surface reflection, and
- c) Rear contact reflection.

The optical losses can be minimized by several methods as follows,

- a) Minimizing top contact coverage of the cell surface.
- b) Using a quarter wavelength antireflection coating on the top surface of the cell. A quarter wavelength antireflection coating cancels the reflected light from the top surface and the coating-semiconductor interface by destructive interference effect as shown in **Figure 1.18**. The thickness of a quarter wavelength antireflection coating is related to the incident wavelength  $\lambda_0$  and refractive index  $n_1$  by,

$$d_{AR} = \frac{\lambda_0}{4n_1} \quad (1.11)$$

The surface reflection can be minimized to zero if the refractive index of the antireflection coating is the geometric mean of that of the materials on either side, i.e.,

$$n_1 = \sqrt{n_0 n_2} \quad (1.12)$$

The variation of percent reflection with respect to light wavelength for a Si cell in the air and under glass is shown in **Figure 1.19**. The graph shows the percent reflection from the surface can be up to 20%.

- c) Surface texturing is another method of minimizing reflection. Rough surface reduces reflection by increasing the chances of reflected light bouncing back onto the surface. Electron microscope photograph of a textured silicon surface is shown in **Figure 1.20**.
- d) Rear surface reflection reduces absorption in the rear cell, allowing the light to bounce back into the cell for possible absorption. Randomizing this back reflection can trap the reflected light for absorption. A heavily doped region at the back of the cell reduces back surface recombination velocity and randomize the rear reflected light [21].

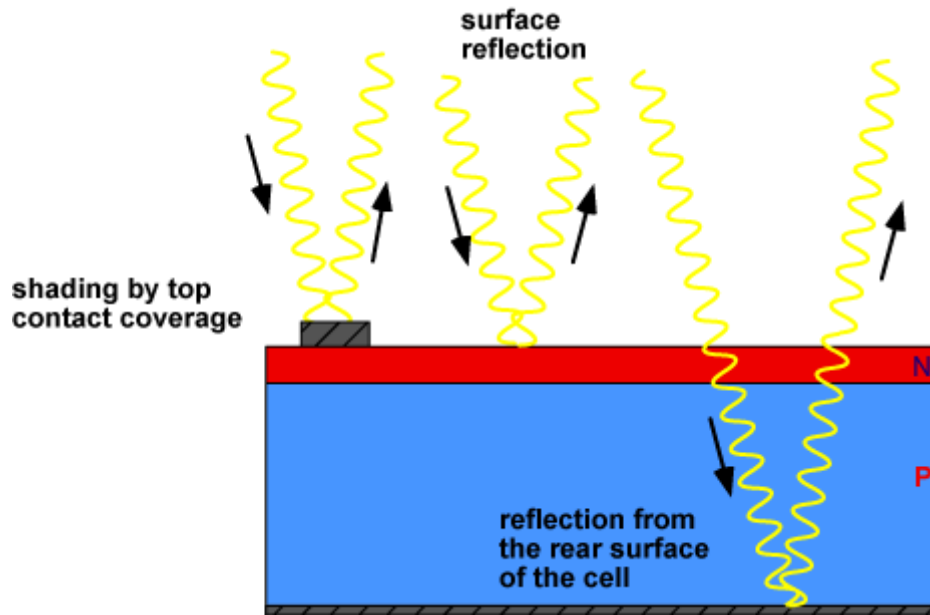


Figure 1.17: Sources of optical losses in a solar cell [37]

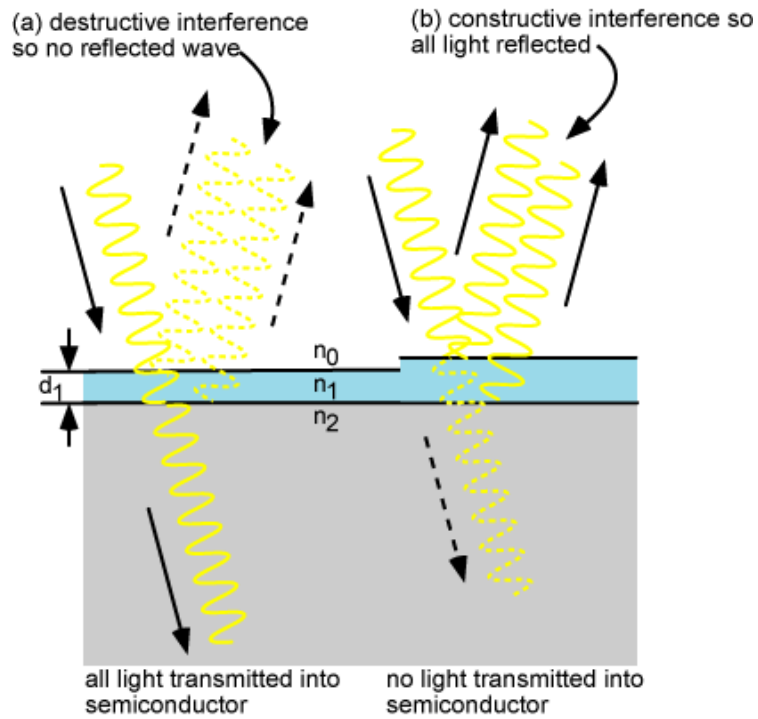


Figure 1.18: Destructive interference effect by antireflection coating on PV surface [38].

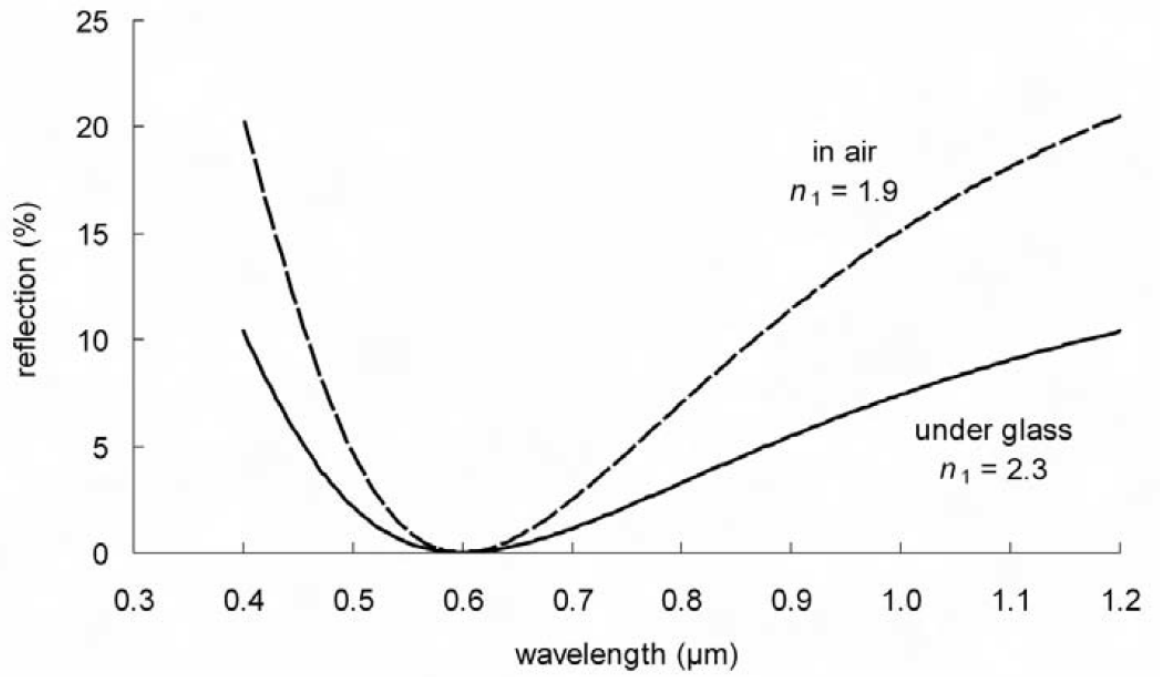


Figure 1.19: The variation of percent reflection with respect to light wavelength for a Si cell ( $n_2 = 3.8$ ) in air ( $n_1 = 1.9$ ) and under glass ( $n_1 = 2.3$ ) [21].

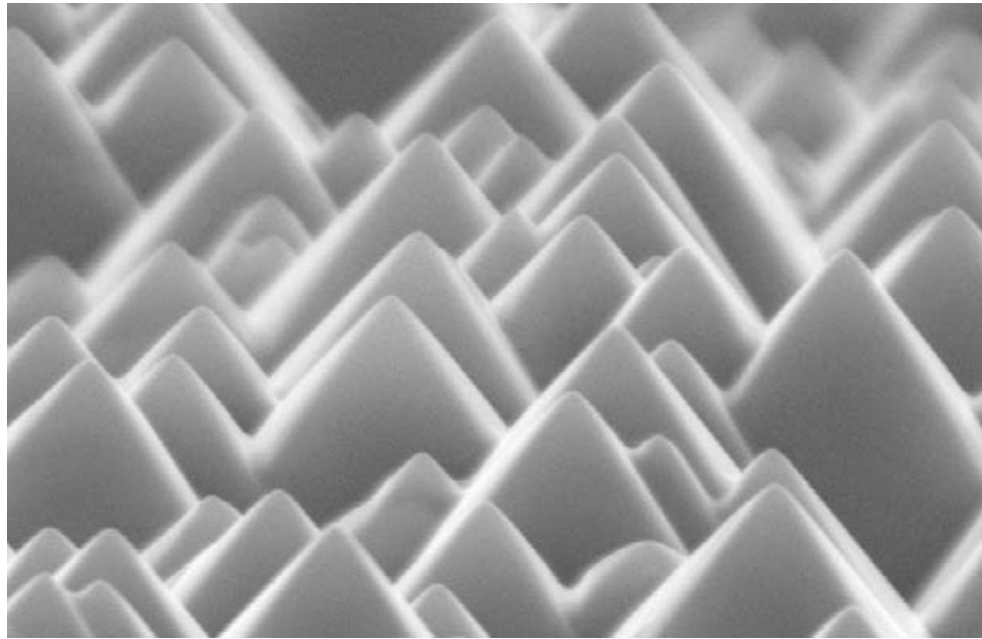


Figure 1.20: Scanning electron microscope image of a textured silicon cell surface for reducing surface reflection [21].



## **1.9 Thesis Outline**

Hybrid Photovoltaic-Thermal (HPVT) systems are an excellent application for buildings which require simultaneous heating and electric power. There are various designs developed to improve the efficiency of HPVT systems. This thesis describes a new design for an HPVT which allows photovoltaic and thermal systems to function independently while regenerating some of the optical losses in the photovoltaic system by hybridization. This research performs detailed experimentation of the new HPVT-Regen system in indoor solar simulation as well as in outdoor solar radiation to study the performance of the photovoltaic subsystem, the thermal subsystem, and the regeneration of photovoltaic optical losses. The thesis is divided into six chapters. Chapter one presents an introduction to global energy demand and need for renewable energy, thermal collectors, photovoltaic technology, hybrid systems, and optical losses in photovoltaics. Chapter 2 presents a detailed review of HPVT systems, experimental and numerical studies done in HPVT systems, and theoretical analysis done in optical losses from PV panels. The research motivation, objectives, phases and the flow chart are described at the end of Chapter 2. Chapter 3 describes the design aspects of the HPVT- Regen system. It includes 3-D modeling and dimensions of the new design done in CATIA. The fabrication of the HPVT-Regen system components, assembling, experimental work done in indoor simulation, test results, and discussion are presented in chapter 4. Outdoor testing, results, and discussions are detailed in chapter 5. Finally, chapter six provides conclusion, future work, and recommendations related to HPVT-Regen research work.

## Chapter 2: Literature Review

### 2.1 History of PV-T Systems

The first work on a flat-plate PVT-liquid system is attributed to Martin Wolf [39]. In 1976 he analyzed a silicon solar array mounted inside a stationary non-concentrating thermal collector, using a lead acid battery as a storage element for residential heating. After the pioneering study of Martin Wolf, the subject of PVT system was quickly taken on by other groups such as MIT. In 1978 the first demonstration project of PVT system was done by professor Böer [40], he applied 13 PVT liquid collectors in his own home, 'Solar Knoll'.

In 1978, MIT Lincoln Laboratory and Sandia [41] jointly acquired three full-size flat plate prototype PVT collectors of two air-type and a water type. The performance of those collectors was below 6.5% electrical and 40% thermal efficiency. The second generation of various designs of air and liquid with the dual flow and multiphase Freon PVTs were proposed. But not all of them was built due to termination of the funds. From 1981 to 1989, Sun Watt manufactured and installed over 100 PVT-liquid collectors.

The 'Solar One' house was the first PVT-air facility built in 1973/1974 at the University of Delaware by professor Boer [42]. In the roof and façade of the house, air collectors were integrated, and four of the 24 roof collectors were equipped with CdS/Cu<sub>2</sub>S cells. In 1998, J.C Hollick [43] with Conserval Engineering Inc. developed the 'PV Solar Wall.' Hollick investigated the method of combining photovoltaic cells with the transpired solar air heater, constructed prototypes, measured the combined electrical and thermal energy produced and compared the results with single function reference panels.

Xing Ju et al. [44] reviews the latest classification of flat plate and concentrating PV-T (CPVT) systems in Science Bulletin 62; 2017. They classify the CPVT systems into three categories: Spectral Beam Splitting (SBS) CPVT, Waste Heat Recovery (WHS) CPVT, and Energy Distribution Fitting (EDF) CPVT. The Waste Heat Recovery CPVT is subcategorized into low concentration, medium concentration and high concentration PVTs.

## 2.2 Experimental Studies in HPV-T Systems

Zondag et al. [44] developed nine design concepts of PVT water collectors classified into four groups as sheet-and-tube, channel, free flow, and two-absorber as shown in **Figure 2.1**. The total efficiency at zero reduced temperature was over 50% and yielded a higher power per unit area. The individual electrical and thermal efficiencies were below the efficiencies of the corresponding standalone systems. The thermal efficiency of glass covered collector was higher than uncovered, but the glass and water layers on top restricted the electrical performance of the PV.

Jin Kim and Jun Kim [45] studied the experimental performance of glazed (glass covered) and unglazed liquid type PV-T collectors in outdoor conditions. The results showed that the thermal efficiency of the glazed PVT collector is 14% higher than that of the unglazed PVT collector, but the unglazed collector had 1.4% higher electrical efficiency than the glazed collector. The overall performance of the glazed collector was 12.6% higher than that of the unglazed collector.

M. Li et al. [46] analyzed a 10 m<sup>2</sup> Trough Concentrating PVT (TCPVT) system with a parabolic trough concentrator, receiver, electrical energy output system, and a thermal energy storage system. Supercell array, GaAs cell array, and Si cell array were pasted on the lighting plate of the receiver with thermally conductive tape (**Figure 2.2**). Forced water circulated through the inner cavity of the receiver cools the solar cells while generating heat. The experimental results obtained average electrical efficiencies of 3.63%, 8.94%, and 3.67% respectively for each cell types. When the mirror reflectivity is improved from 0.69 to 0.92, the electrical efficiency increased by 0.9%, 2.62%, and 5.47% respectively for each cell types. Among the three cell types used, Si cell array showed the best performance.

Kostic et al. [47] studied the influence of reflectance from flat plate solar radiation concentrators made of Al sheet and Al foil on the energy efficiency of PVT collector. The total reflectance from concentrators made of Al sheet and Al foil are the same, but specular reflectance is bigger in concentrators made of Al foil which increases the solar radiation intensity concentration factor. For optimal positions, the factor is obtained to be 1.44% and 1.66% respectively. However, the electrical efficiency of the PVT decreases slightly with an increase in solar radiation intensity concentration factor.

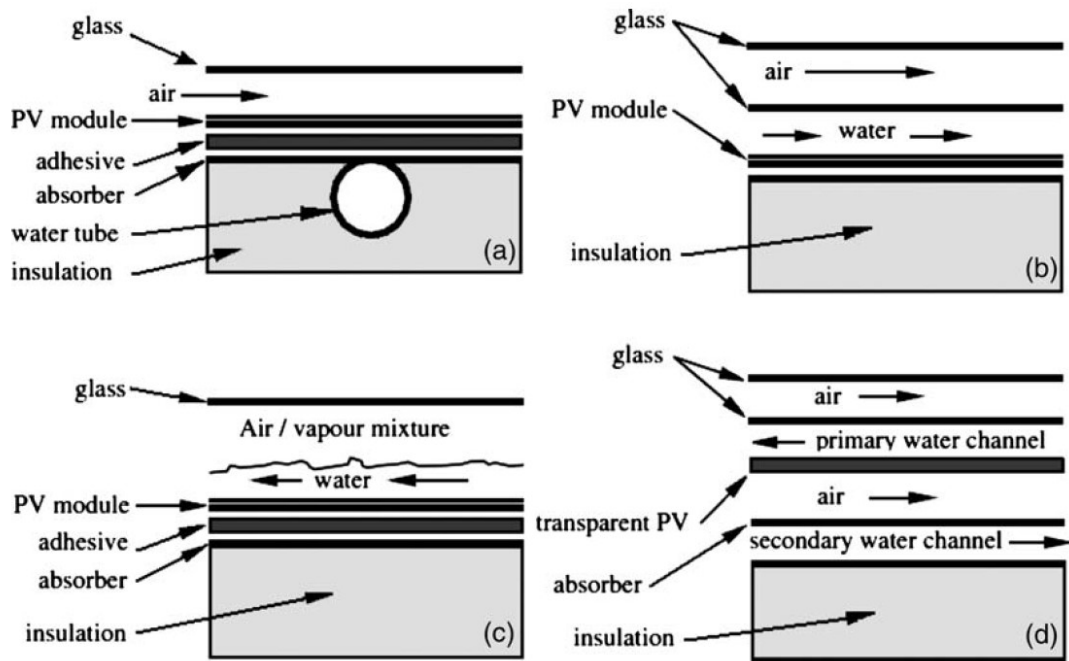


Figure 2.1: Various collector concepts by Zondag et al., (a) sheet-and-tube, (b) channel PVT, (c) free flow PVT, (d) two-absorber PVT [44].



Figure 2.2: The 10 m<sup>2</sup> Trough Concentrating PVT (TCPVT) with Supercell, GaAs and Si cell array at receiver and high reflectivity concentrating mirrors of reflectivity 0.69 and 0.92 analyzed by M. Li et al. [46].

M. Chaabane et al. [48] designed and tested a low concentrating (CR: 1 to 10x) photovoltaic (PV) and photovoltaic/thermal (PVT) systems with an asymmetric compound parabolic photovoltaic concentrator. The CPVT includes a concentrator, a black painted rectangular conduct thermal unit, and a PV panel mounted on the thermal unit as shown in **Figure 2.3**. They performed experimental as well as computational analysis of the system obtaining satisfactory compliance. Compromising the power, efficiency and, governing parameters they obtained optimum electrical, thermal and overall efficiencies to be 10.02%, 9.4%, and 26% respectively.

Since 85% of the incoming solar radiation is either reflected or absorbed as heat by the traditional PV system, A. Muthu Manohar et al. [49] worked on the performance analysis of a Parabolic Trough Concentrating Photovoltaic-Thermal System. They employed a parabolic trough as light concentrator and channel PV/T collector as the receiver. To capture maximum reflection from the trough, they have designed a “V” shaped receiver. The concentrator increased the temperature on PV system by 20 °C which was then transferred to cooling water. They also report adverse impact on the electrical performance due to a significant rise in PV temperature.

### **2.3 Numerical Studies on HPVT systems**

Calise et al. [50] presented a finite volume model of a medium concentration (CR: 10 to 100x) PVT (MCPVT) system with a Parabolic Trough Concentrator (PTC) having a linear triangular receiver as shown in **Figure 2.4**. They obtained an electrical efficiency of 22% and a thermal efficiency of 63%. To enhance electrical efficiency, they suggested triple-junction solar cells such as InGaP/InGaAs/Ge which have good performance at high temperatures.

Renno and Giacomo [51], [52] proposed a high concentration (CR: > 100x) PVT dynamic model using FEM. They used InGaP/InGaAs/Ge triple junction solar cells. The cooling fluid (water and glycol solution) obtained over 85 °C at 1000 suns. The HCPVT systems are excellent from the energy point of view, but they have inefficiencies and maintenance problems such as moving of tracking system, cell wear due to hotspots, optics cleaning that affects system efficiency and energy output.

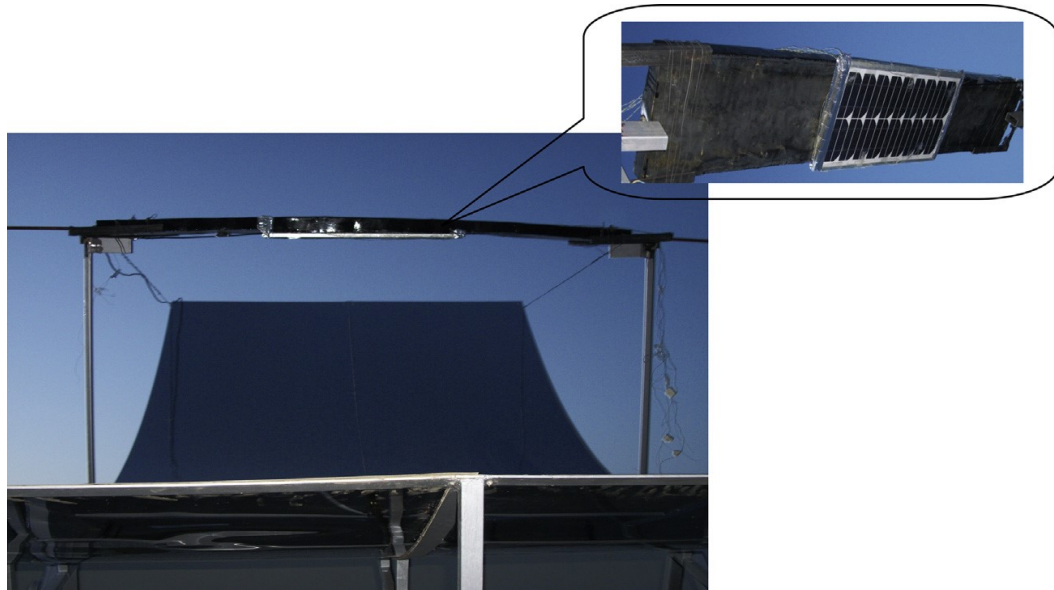


Figure 2.3: CPVT system with PV panel attached to the thermal unit and facing the parabolic concentrator designed by M. Chaabane et al. [48].

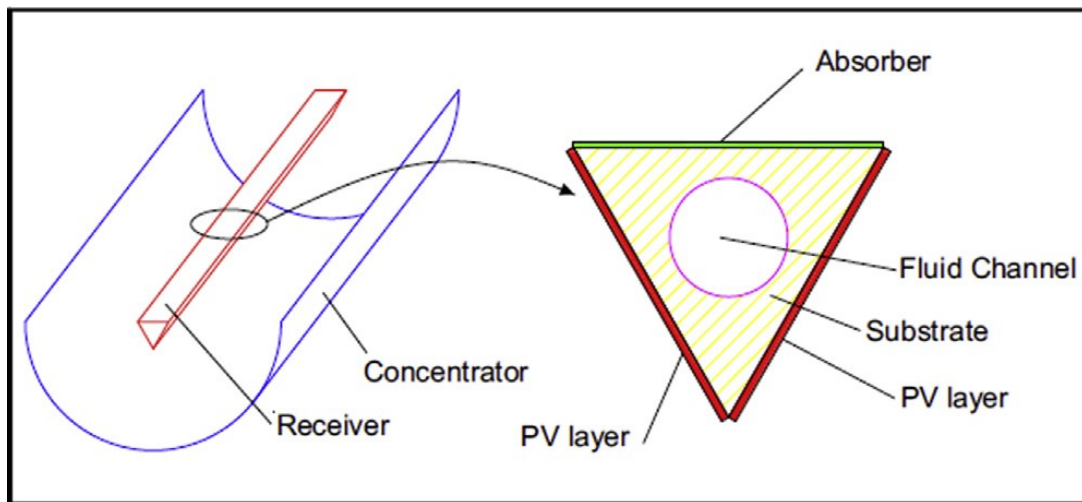


Figure 2.4: Finite volume model of the MCPVT system with a PTC and a linear triangular receiver designed by Calise et al. [50].

## 2.4 Reflection Losses in a PV panel

Sandnes and Rekstad [53] designed, built, and tested a PVT collector and developed an analytical model for the system by modifying Hottel and Willer models for flat plate collectors. They studied the effect of adding glass cover to the PVT collector to reduce heat losses. They found out that, adding a glass cover to the collector reduces heat losses to the surrounding but also reduces the energy absorbed by the collector due to the reflection from the glass by around 10%. The reduced transmittance of the light resulted in a reduction of electrical energy from the PV panel.

Fujisawa and Tani [54] designed, constructed a PVT Collector and analyzed the experimental performance. They found that coverless PV/T collector produced the highest electrical energy. However, the thermal performance of the single covered PVT collector was comparable to a flat plate collector as glass covering reduced the heat losses to the surroundings.

T. Yamada et al. [55] analyzed the influence of reflection on a PV module using optical properties of the module materials. Using the optical performance of a four-layer encapsulation (shown in **Figure 2.5**), a simulation was made on the reflection loss from PV module according to Fresnel's law. They have some results showing the relationship between the total transmittance of the incident radiation through the layers and the incident angle as shown in **Figure 2.6**. The results show that only less than 80% of the light is transmitted to the silicon cell within an incident angle of 50 degrees. The transmittance is steeply declining when the incident angle varies from 50 to 90 degrees.

T. Yamada et al. gives an empirical relation between the transmittance and the reflection of light through the medium [55],

$$\tau = (1 - r)^2 \quad (2.1)$$

Thus, the total reflection can be given by

$$r = 1 - \sqrt{\tau} \quad (2.2)$$

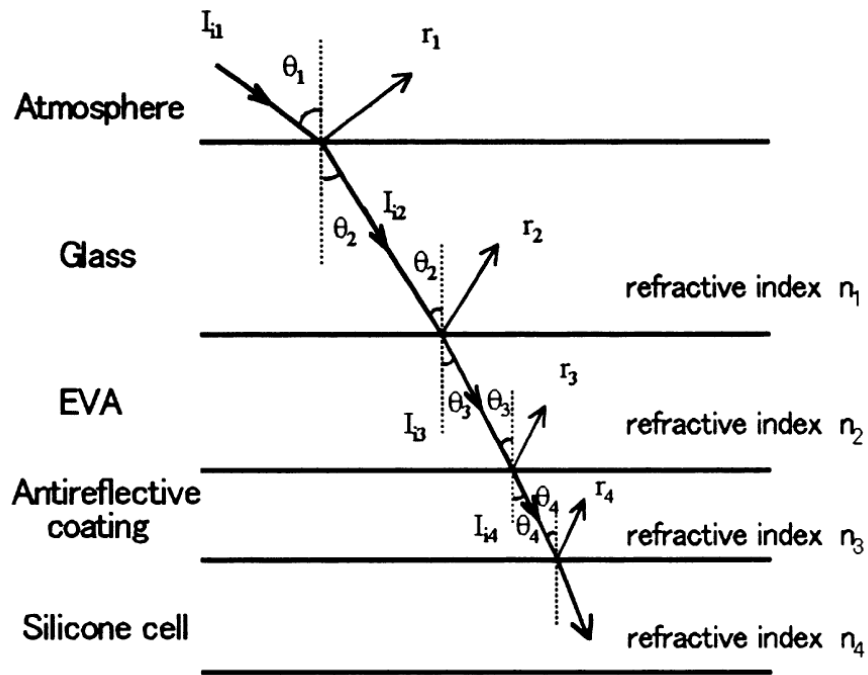


Figure 2.5: The four-layer encapsulation of a PV module used for optical analysis of reflection losses by Takao Yamada et al. [55].

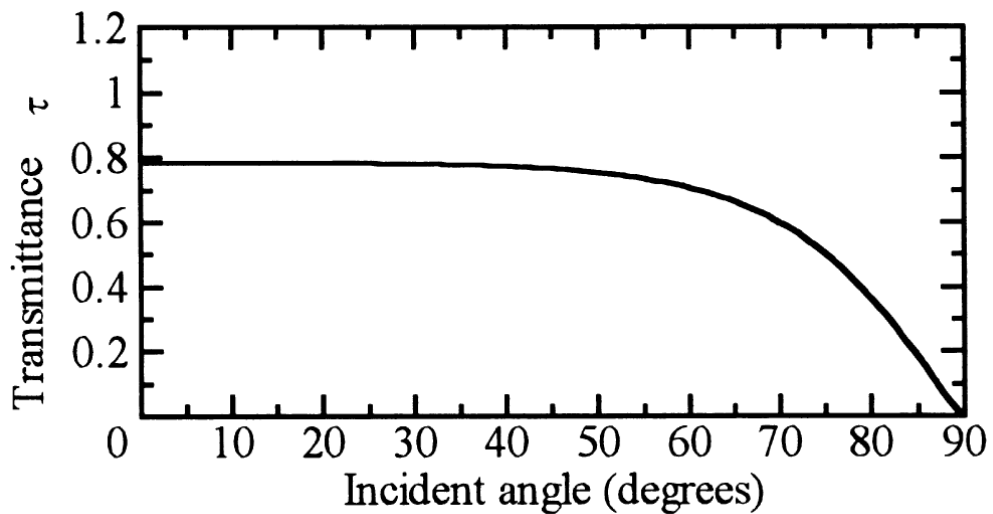


Figure 2.6: The relation between total transmittance through PV module and the angle of incidence [55].



N. Martin and J. M. Ruiz [56] analyzed reflection losses from PV modules and presented an analytical model based on theoretical and experimental results for crystalline and amorphous silicon PV modules with or without antireflection coatings. They proposed the following formula for the reflectance of a PV module [56],

$$\bar{R}(\alpha) = \bar{R}(0) + [1 - \bar{R}(0)] \left[ \frac{\exp(-\cos^2 \alpha / a_r) - \exp(1/a_r)}{1 - \exp(-1/a_r)} \right] \quad (2.3)$$

where,  $\bar{R}(0)$  is the weighted reflectance at STCs,  $\alpha$  is the irradiance angle of incidence, and  $a_r$  is the dimensionless angular loss coefficient.

The annual reflection loss is given by [57],

$$AL(\alpha) = 1 - \left[ \frac{1 - \exp(-\cos^2 \alpha / a_r)}{1 - \exp(-1/a_r)} \right] \quad (2.4)$$

The dimensionless angular loss coefficient,  $a_r$  range from 0.16 to 0.17 for commercial clean silicon modules, 0.20 for module surfaces with moderate dust, and 0.27 for a significant quantity of dust [57].

## 2.5 Thesis Research Objectives and Outline

From the literature review, it is understood that a PV panel reflects up to 20% of the incident light even after employing antireflection layers. There are studies of numerical quantification of this reflected light but lacks effective methods and experimentation in utilizing them. Due to lack of detailed studies in utilizing the reflection losses from the photovoltaic panels, a new design for HPVT system is developed to regenerate the reflection losses at the same time ensuring uninterrupted functioning of photovoltaic and thermal subsystems. This thesis research involves detailed design, construction, and instrumentation of a new HPVT-Regen system for testing under indoor solar simulation as well as under outdoor solar radiation. For the design purpose, to study the effect of horizontal and curved-PV panels, a flexible PV panel was tested in horizontal

as well as in curved positions under an indoor solar simulator. The test results showed that the performance characteristics were identical, and hence the new design fixes PV panel in a curved position in a wooden cylindrical frame. Detailed performance characteristics of the PV panel was done in the indoor solar simulator. PV modules for the regeneration of reflected light was tested and fully characterized for comparing the regeneration efficiency. The thermal subsystem was assembled incorporating the regen-PV modules. Testing of thermal subsystem involved calibration in excluding the effects of the air blower and thermocouple heating. The regeneration subsystem was tested to study the amount of regeneration of electricity as well as heat. In the indoor simulation, each subsystem was studied individually since the radiation is constant. In the outdoor testing, all the subsystem was tested and measured at the same time since the solar radiation is changing continuously. **Figure 2.7** shows the primary component and objectives of this thesis research work.

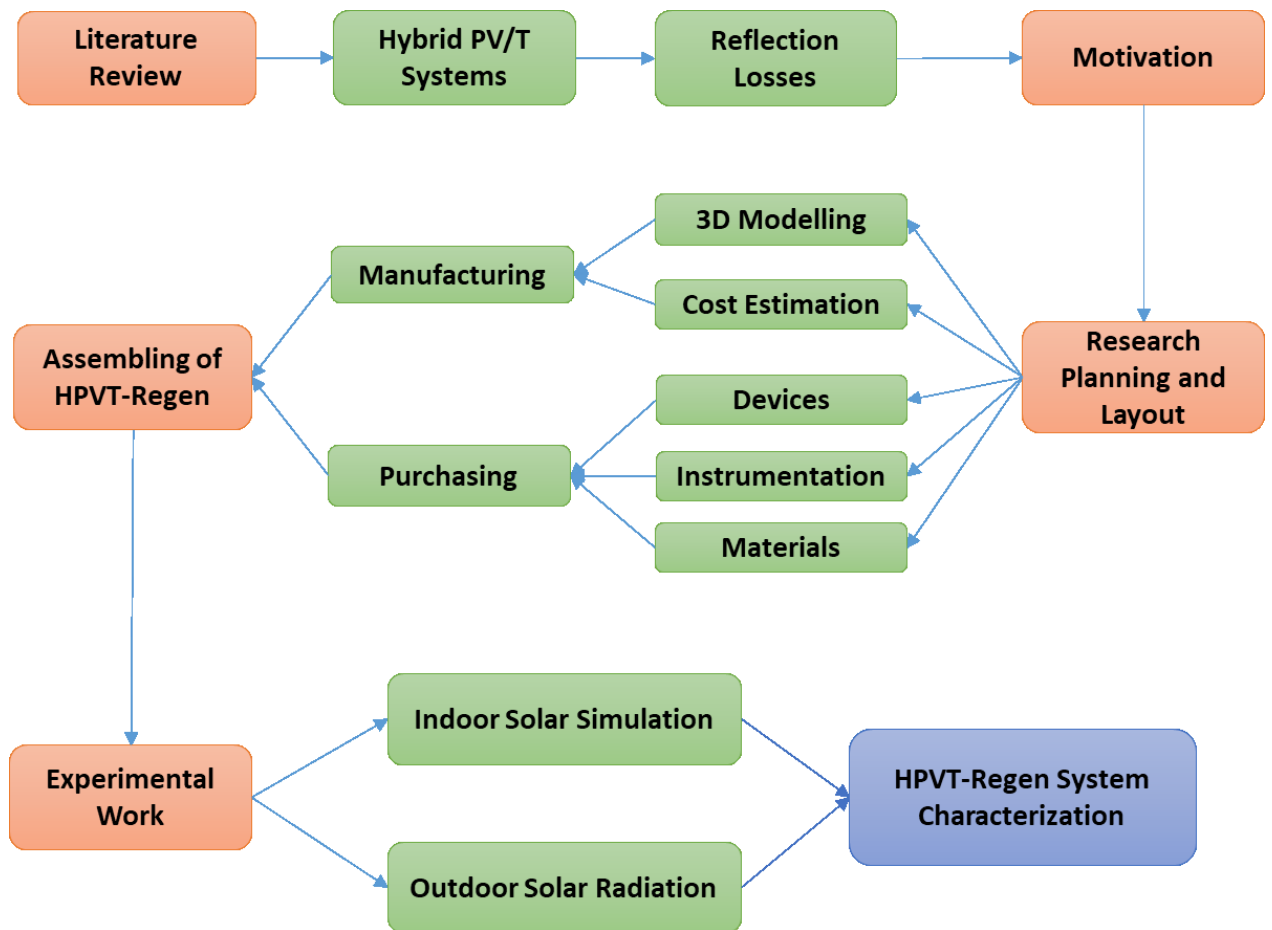


Figure 2.7: Research flow chart showing major phases in this thesis.

# **Chapter 3: Design, Construction and Assembly of the Hybrid Photovoltaic-Thermal system with Regeneration (HPVT-Regen)**

This chapter presents a detailed description of the design of the HPVT-Regen system, construction and assembly of the components, and instrumentation of the experimental test setup. The HPVT-Regen system has a photovoltaic subsystem, a thermal subsystem, and a regenerating subsystem put together to form a hybrid system to produce electrical as well as thermal energy. The design criteria of this HPVT-Regen system are to regenerate the reflected light without affecting the proper functioning of the photovoltaic and thermal subsystems, to concentrate the reflected light by using a flexible panel in a curved position, to regenerate some of the reflected light into electricity and heat and to characterize the experimental performance of the HPVT-Regen system under laboratory simulator lights as well as under Thunder Bay's weather conditions.

## **3.1 Photovoltaic Subsystem of the HPVT-Regen**

A flexible monocrystalline silicon PV panel of 25 W rated power and 18 V open circuit voltage (**Table 3.1 and Figure 3.1**) is proposed for the design. Flexible solar cells are manufactured by depositing photovoltaic material on flexible substrates. Circuits of photovoltaic materials are deposited in five layers of polymer substrates in a vacuum chamber by the process of chemical vapor deposition. The solar cells are protected by UV resistant fluoropolymer or thermoplastic olefin rather than glass in conventional solar panels.

The flexible PV panel can be held in a curved position. The performance of the PV panel in horizontal as well as in curved positions were studied under indoor simulation lights, and the performance is found to be identical. Thus, using PV in a curved position gives room for the PV panel to operate independently from the thermal component at the same time focusing the reflected light on to the focal line. The flexible PV panel is held in a curved position using a wooden frame in cylindrical section. The dimensions and the drawing of the wooden structure will be described later in this chapter.

**Table 3.1: Specification of the flexible monocrystalline PV panel [A-1].**

<b>Description</b>	<b>Details</b>
Material	Mono-crystalline silicon
Size	560mm × 280 mm
Total area of the cells	0.116 m <sup>2</sup>
Maximum power	25 W
$I_{mp}$	1.38 A
$V_{mp}$	18 V
Operating Temperature	-40 to 85°C



Figure 3.1: Flexible monocrystalline silicon PV panel used for the experimentation [A1].

### 3.2 Thermal Subsystem of the HPVT-Regen

The thermal subsystem exchanges the heat of the solar radiation into the working fluid, air. The thermal system is made of a steel channel through which air can be blown at various flow rates. The steel channel is wrapped with a black copper absorber sheet of high thermal absorptivity and lower emissivity. The thermal contact between the absorber sheet and steel channel is made intact with thermally conductive adhesives. The CATIA drawing and the dimensions of the steel channel are shown in **Figure 3.2**. The thermal properties of the steel and the absorber sheet are given in **Table 3.2**. The dimensions of the thermal system and the absorber sheet are given in **Table 3.3**.

**Table 3.2: Thermal properties of the materials of thermal subsystem [A2].**

Thermal conductivity of the black absorber, $k_t$	400 W/mK
Absorptivity of the absorber, $\alpha_t$	0.95
Emissivity of the absorber, $\epsilon$	0.08
Thermal conductivity of the adhesive	2.306 W/mK
Thermal conductivity of the steel	43 W/mK

**Table 3.3: Dimensions of the thermal subsystem.**

Dimensions of steel channel	870 mm $\times$ 60mm $\times$ 27mm
Area of cross section of air flow, $A_{th}$	0.03 m <sup>2</sup>
Thickness of the absorber sheet	0.12 mm

### 3.3 PV Frame: Supporting Structure

The supporting frame for the PV panel and the thermal subsystems are made of plywood. The structure is designed in CATIA V5 to match with the dimensions of the PV panel and the thermal system. The Catia drawing and the dimensions of the wooden frame are shown in **Figure 3.3**. The curvature, the angle of section and radius was determined based on the size and flexibility of the PV panel. The PV subsystem will be fixed in the slot of the cylindrical section, and the thermal subsystem will be fixed at the focal line.

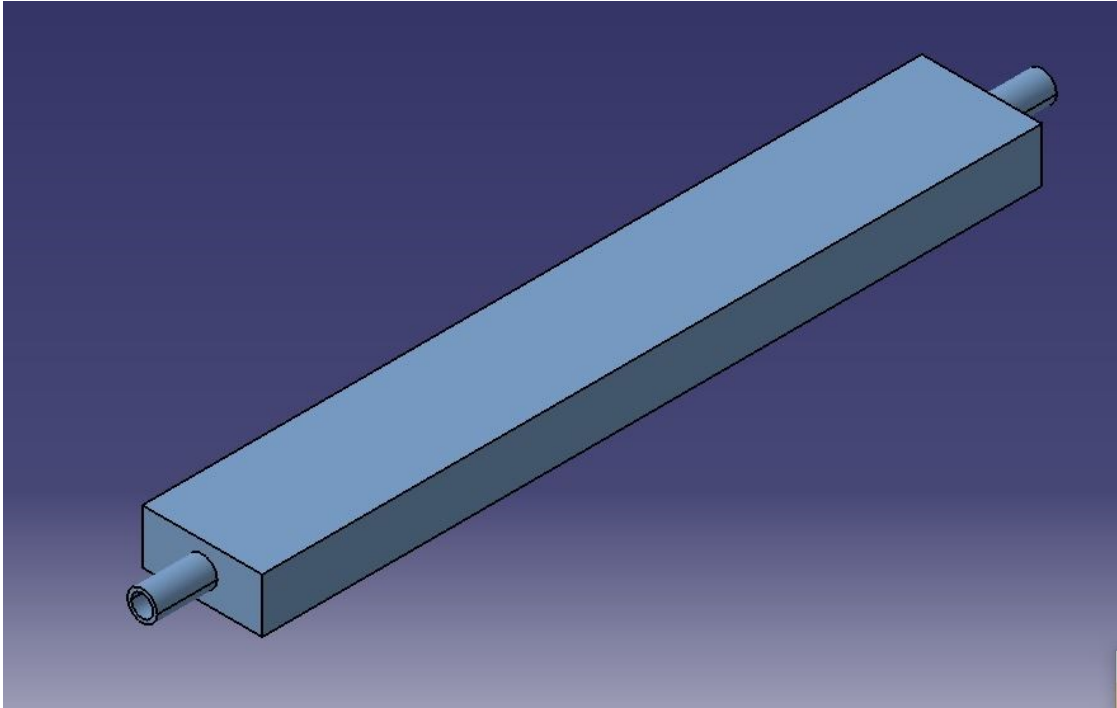


Figure 3.2 a: Isometric view of the steel channel of the thermal system designed in CATIA V5.

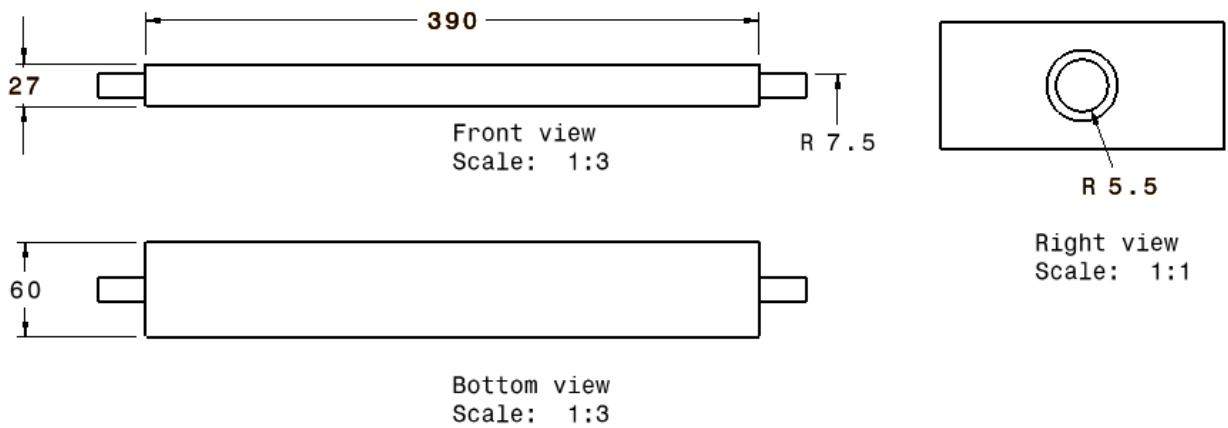


Figure 3.2 b: Orthographic projections of the steel channel drafted in CATIA V5. All dimensions are in mm.

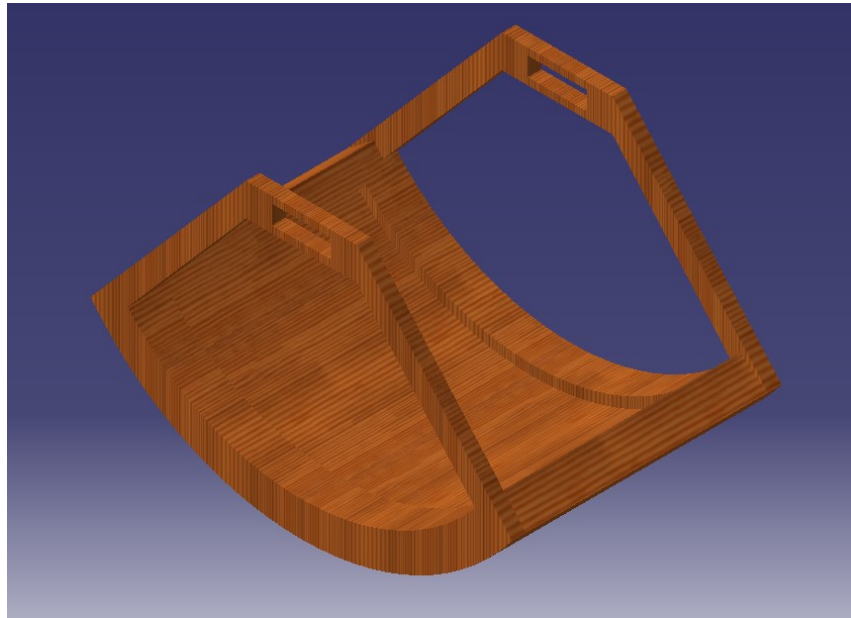


Figure 3.3 a: Isometric view of the wooden structure designed in CATIA V5.

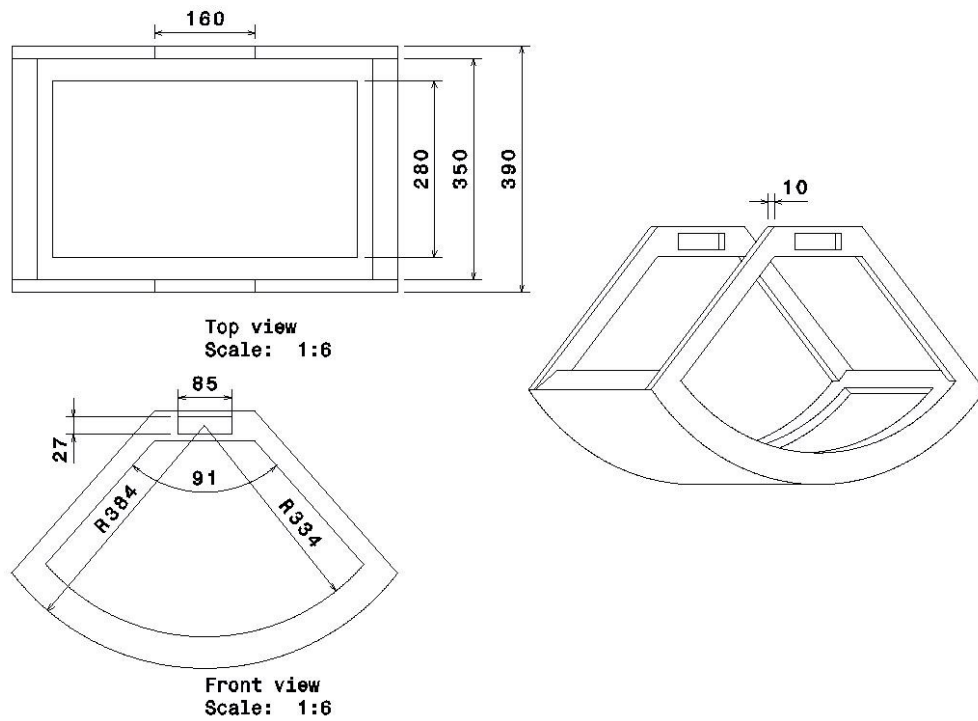


Figure 3.3 b: Orthographic and isometric draft of the wooden structure. All dimensions are in mm.



### 3.4 Regeneration Subsystem of the HPVT-Regen

The objective of the regenerating system is to regenerate the part of the incoming solar radiation that is reflected from the PV surface. Up to 20% of the light is reflected from the PV panel from the top and rear surface of the PV modules. Antireflection coatings are the only solution implemented so far to reduce the reflection losses. In designing this hybrid PVT system, a regenerating system is added to regenerate the reflection losses into electricity as well as heat. The regeneration system consists of four low rating monocrystalline silicon PV modules (**Figure 3.4**) coupled to the thermal system facing the curved-PV panel. The specification of the module is given in **Table 3.4**. The thermal subsystem with regen-PVs is fixed to the focal line of the curved-PV panel receiving a portion of reflected light. Thus, the regen-PVs convert reflected light into electricity as well as dissipate the waste heat into the thermal system.

**Table 3.4: The specifications of the Regen-PV modules [A3]**

Description	Details
Material	Monocrystalline silicon
Size	80mm × 80mm
Area of the cells, $A_{cpv}$	0.0156 m <sup>2</sup>
Rated power	0.5 W
Rated voltage	5 V
Rated current	100 mA

The assembly of the regeneration system to the thermal system in CATIA is shown in **Figure 3.5**, and the orthographic projections with the dimensions of the regeneration system is shown in **Figure 3.6**.

The final assembly of the components without the instrumentation is shown in **Figure 3.7**. This design permits PV as well as thermal subsystems to work independently within same area and irradiation. The radius of the curve can be varied for the experiments with respect to the angle of incidence of radiation to prevent shadow of the thermal subsystem from falling on the PV panel.



Figure 3.4: The low rating monocrystalline silicon mini PV module used for regeneration [A3].

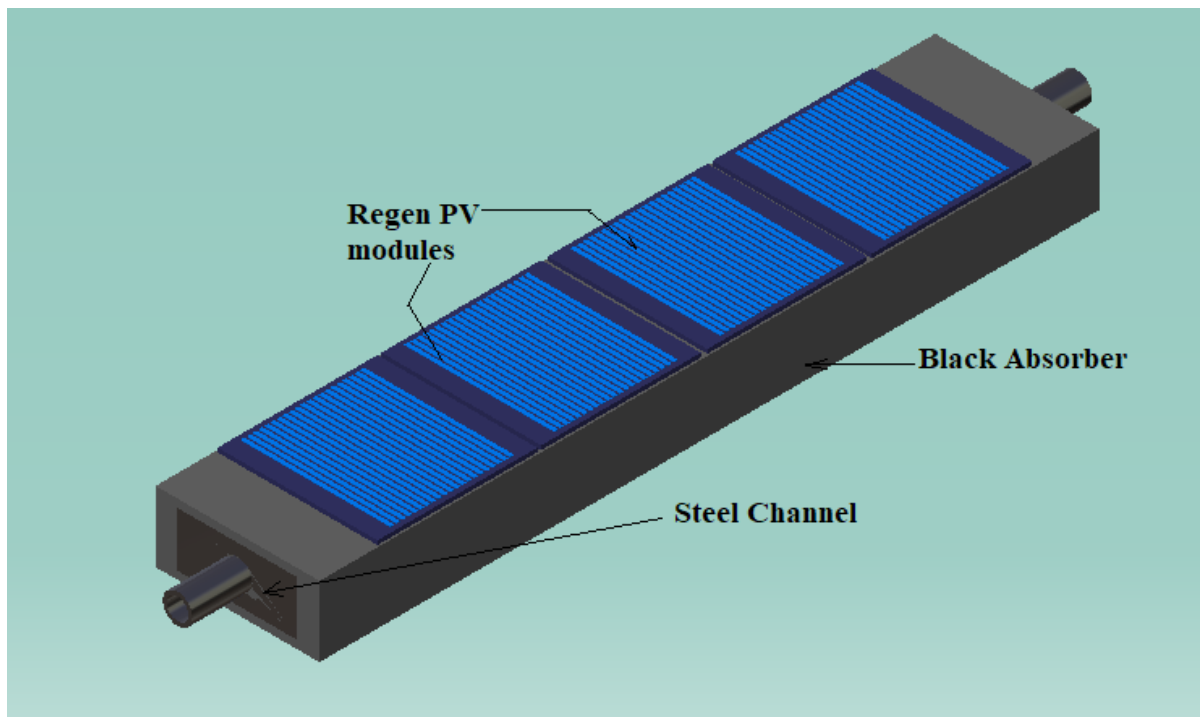


Figure 3.5: The assembly of the regen-PVs with the thermal system done in CATIA V5.

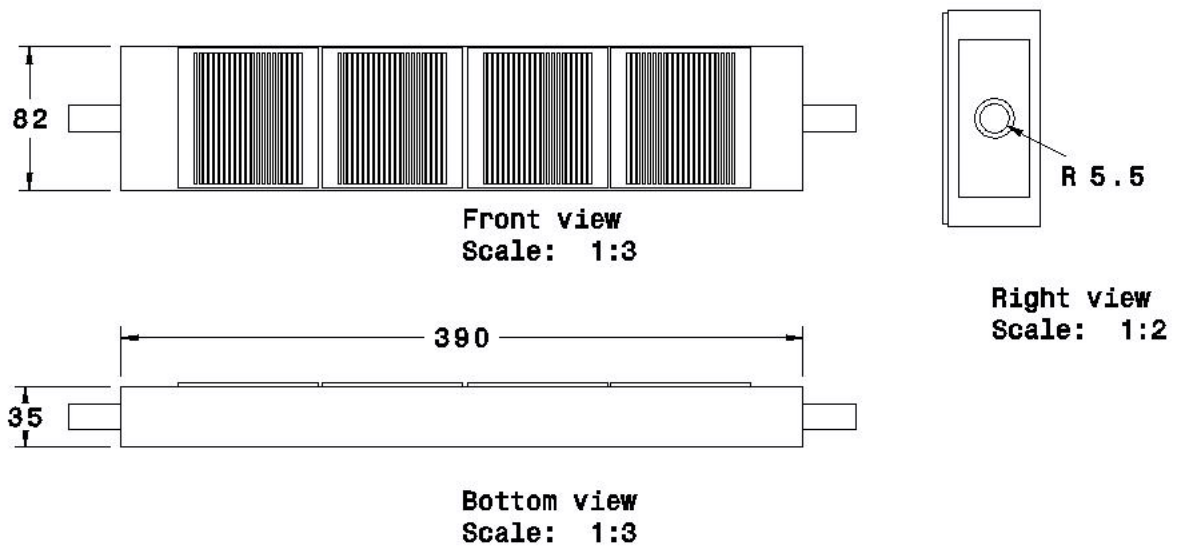


Figure 3.6: Orthographic projections of the regen system. All dimensions are in mm.

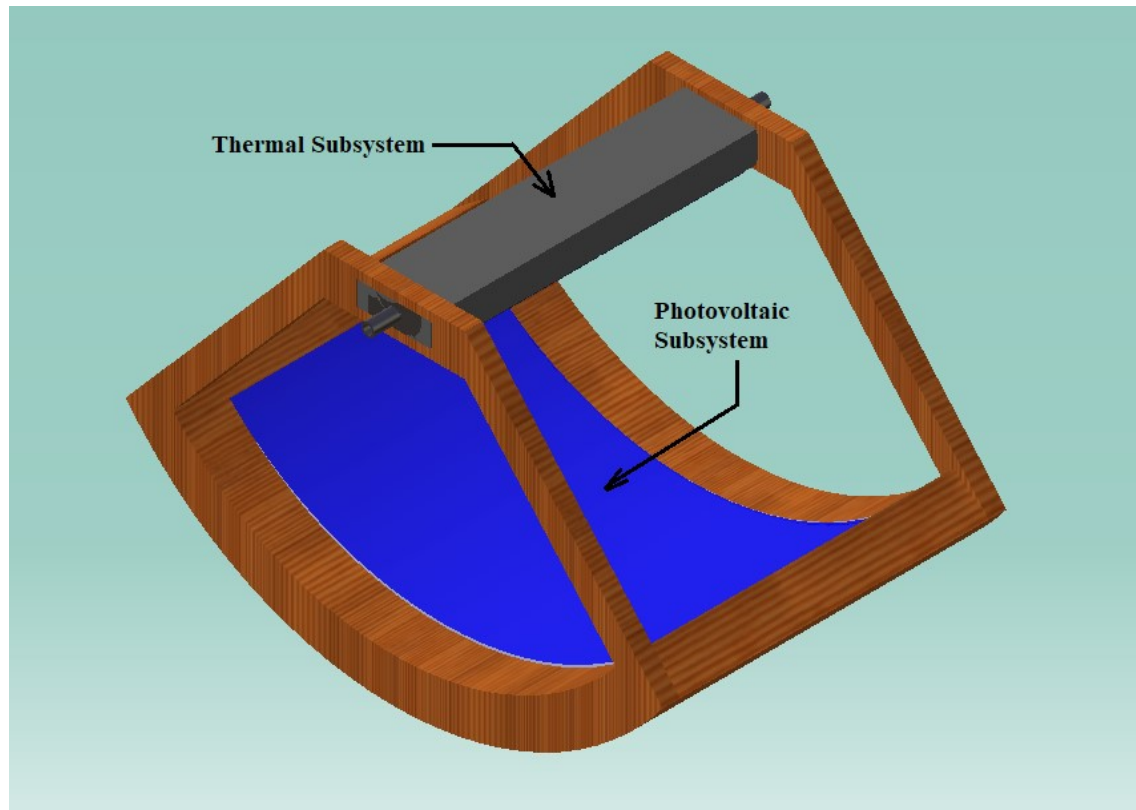


Figure 3.7a: The final assembly of the HPVT-Regen system without the instruments.

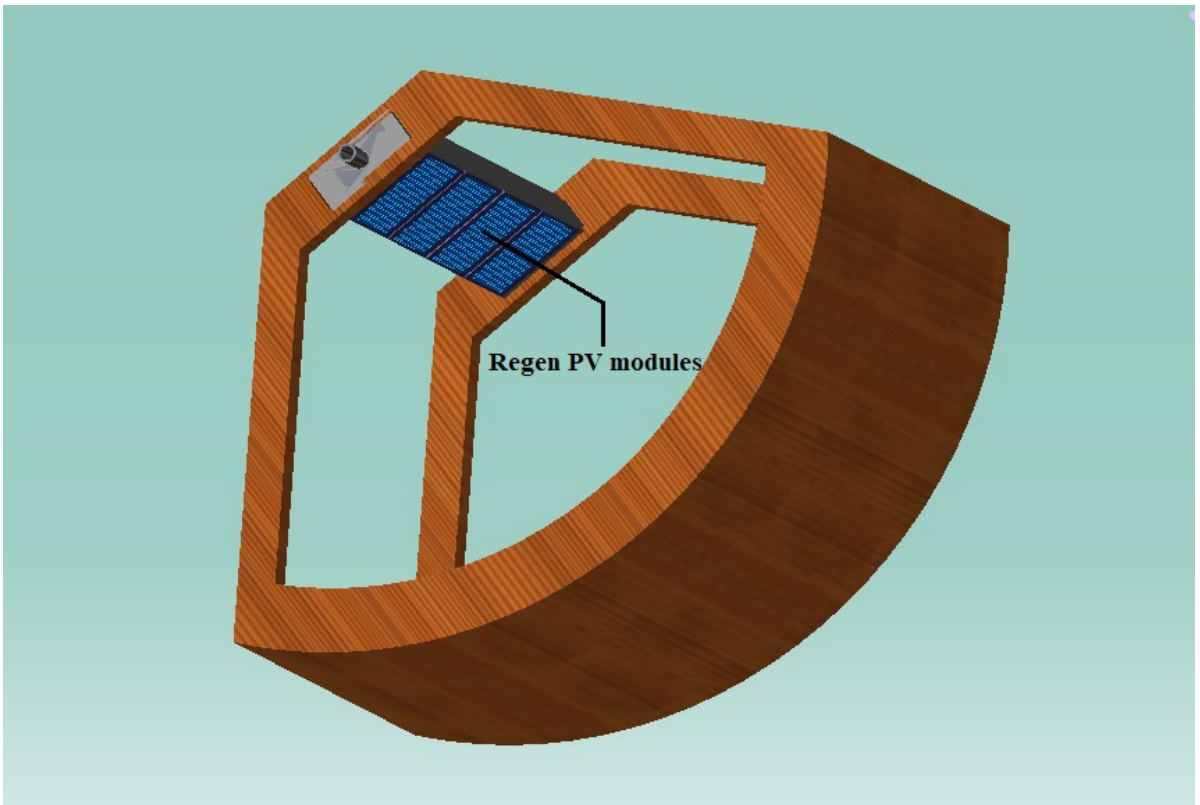


Figure 3.7b: The final assembly of the HPVT-Regen system showing regen-PV modules facing the curved-PV panel.

### 3.5 Construction of the Wooden PV Frame

The wooden frame to support the photovoltaic and thermal subsystems were made of plywood. For the initial test setup, low-cost plywood was sufficient, was readily available, and easy to work on. The carpentry works involved using saw, milling machine, grinding machine, drilling machine, adhesives, and sand papers to make the PV support frame to the design dimensions. **Figure 3.8** depicts various stages of carpentry to build the wooden PV frame. The carpentry stages are as follows

- a) On a 10 mm thick plane plywood, the cross-section of the wooden frame was drawn according to the design dimensions with a tolerance of +2mm.
- b) The ply-wood was cut out using a wood milling machine.
- c) The dimensions were made accurate using a grinding machine.
- d) Similarly, all the different cross sections were cut out of plywood and joined together with carpenter's glue to form the final shape.

### 3.6 Construction of the Thermal Collector

The thermal collector is made of a steel channel for air flow, a black copper absorber sheet, regen-PV modules, and thermally conductive adhesive. The steel channel is wrapped intact by the black copper sheet using thermally conductive adhesive. The black absorber has a high absorptivity of 0.95 and emissivity of 0.08. The inlet and outlet of the steel channel are connected with  $\frac{1}{4}$ " brass pipes allowing the air to flow through them. The air is forced to flow through the pipes and steel channel using an air blower. On the bottom surface of the thermal collector, four low rating PV modules of 0.5 W 5V were connected in parallel. The air temperature measurement at the inlet and outlet of the collector were facilitated with K-type thermocouples. The thermal subsystem is mounted on the focal line of the wooden frame with the black surface facing the sun and the bottom regen-PV surface facing downward to the curved section. **Figure 3.9** shows the assembly of the thermal subsystem with the steel channel, absorber, regen-PV modules, and associated pipes.



Figure 3.8: The carpentry stages in the construction of wooden PV frame.

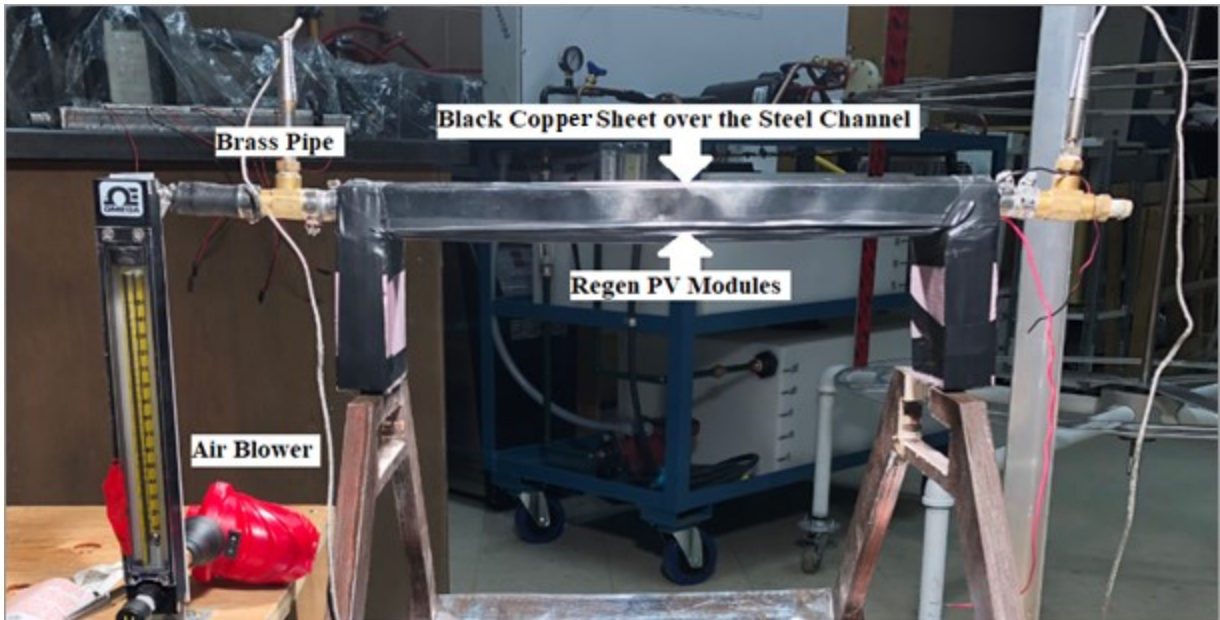


Figure 3.9: The thermal collector with Cu absorber around steel channel, regen-PV modules, and air blower.

### **3.7 Instrumentation for Testing HPVT-Regen System**

Instruments play a crucial role by measuring the performance parameters with which the system is evaluated. The HPVT-Regen system requires various instruments for measuring the current, voltage, electric load, irradiation, reflection, temperature, thermal radiation, and air flow rate. **Figure 3.10** shows the outline of the instrumentation used in testing the system. The details of the various instruments are as follows,

#### **I. Ammeter**

An ammeter measures electric current in a circuit. The SI unit of current is ampere (A).

#### **II. Voltmeter**

A voltmeter measures voltage-drop across a device in an electric circuit. The SI unit of voltage is volt (V).

#### **III. Ohmmeter**

An ohmmeter measures electrical resistance of a device in an electric circuit. The SI unit of electric resistance is ohm ( $\Omega$ ).

#### **IV. Pyranometer**

A pyranometer measures the solar radiation in  $W/m^2$ .

#### **V. Thermometer and Thermocouple**

A thermocouple is a temperature sensor and a thermometer measures the sensed temperature. The SI unit of temperature is degree Celsius ( $^{\circ}C$ ).

#### **VI. IR Camera**

An IR camera measures the thermal radiation emitted from a surface above absolute zero temperature.

#### **VII. Rotameter**

OMEGA-FL-3840ST rotameter is used to measure the flow rate of a fluid, mainly water and air.

### **3.8 Assembly of the HPVT-Regen System**

In the assembly of the HPVT-Regen system, the PV panel is held in the slot of the wooden cylindrical section. The thermal collector with regen-PV modules are fixed at the focal line with regen-PVs facing the curved-PV panel. **Figure 3.11** shows the complete assembly of the HPVT-Regen system with instrumentation for indoor testing.

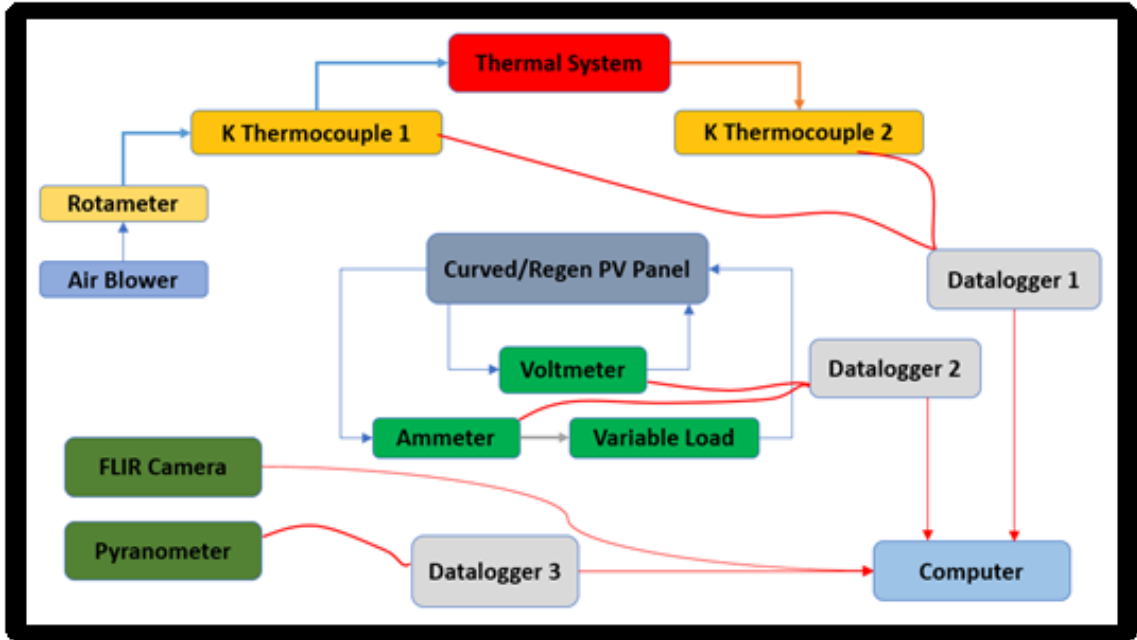


Figure 3.10: The real-time fully instrumented experimental test setup of the HPVT-Regen system used in this research.

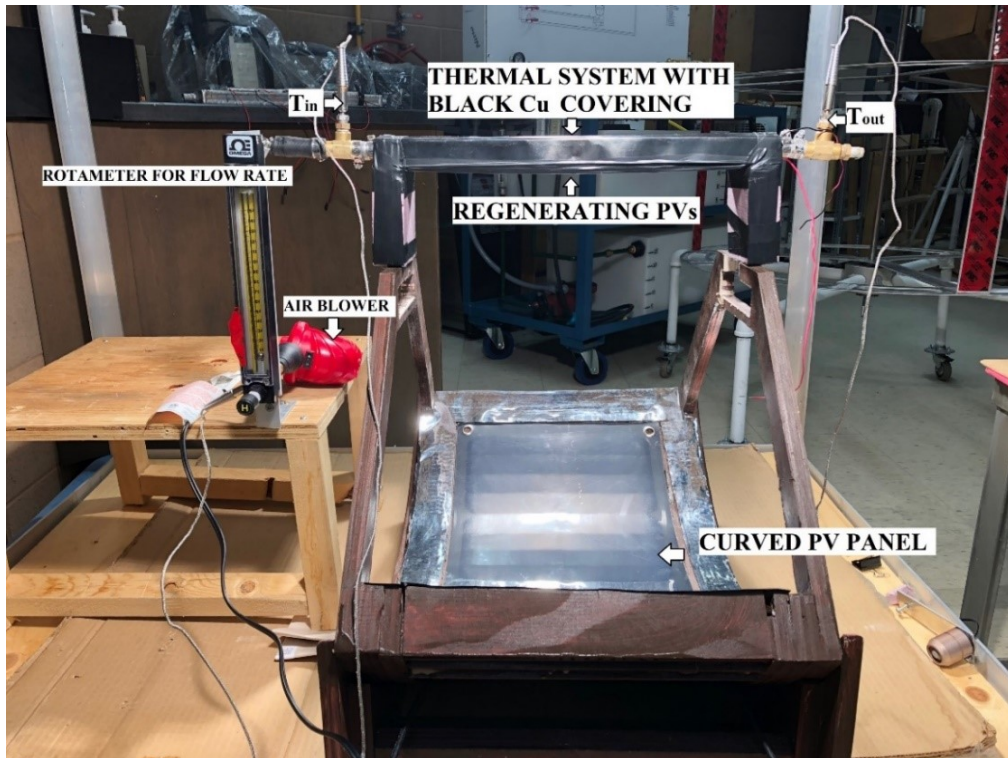


Figure 3.11: The photograph of the complete assembly of the HPVT-Regen system for indoor testing.



### 3.9 Solar Simulator

A solar simulator is a light source like the sun with broad optical output in the range of different solar cell technologies. Various kinds of bulbs can be used to simulate sunlight such as Xenon arc lamps, Quartz-Tungsten halogen lamps, LEDs etc. The solar simulators are designed and evaluated to have some requirements given in the following,

1. Spectral match to the reference spectrum (AM1.5) over a certain wavelength range,
2. Non-uniformity of the irradiance within the measurement test plane,
3. Temporary instability of the irradiance over the course of the measurement.

**Figure 3.12** shows the solar simulator used for the indoor testing of the HPVT-regen system. The assembled HPVT is placed under the solar simulator for performance characterization. The test was done with two halogen lamps illuminated. **Figure 3.13** shows the pyranometer graph of the irradiance measurement. The average irradiance is measured to be  $173.039 \text{ W/m}^2$ .

### 3.10 Energy Balance of the HPVT-Regen System

The energy flow diagram of the proposed HPVT-Regen system explains the conversion of energy from the sun into electricity and heat through photovoltaic and thermal subsystems respectively. The radiation from the sun impinges on the curved-PV panel as well as on the thermal collector in the focal line. The curved-PV panel converts a portion of the solar radiation into electricity. The unabsorbed incident radiation is dissipated into heat. Some of the light incident on the PV panel is reflected (up to 20%) from the PV surface.

Simultaneously, thermal collector also receives the solar radiation. The black absorber on the thermal subsystem has an absorptivity of 0.95, which absorbs the solar radiation and delivers the heat to the steel channel. Through the heat channel, the working fluid, air is flowing at a specific flow rate. This heat is then transferred to the flowing air. The heated air will be then supplied for space heating or to reduce the load on existing HVAC system.

The light reflected from the curved-PV panel is focused to the regen-PV modules arranged on the bottom surface of the thermal collector. The regen-PV modules convert the reflected light into electricity of lower power. These regen-PV modules also dissipate the unabsorbed light as heat into the steel channel and then exchanged to the flowing air. This low power electricity and heat produced from the reflected light are the regenerated power. The flow diagram showing the energy balance of the HPVT-Regen system is depicted in **Figure 3.14**.

### 3.11 Economics of the HPVT-Regen System

Table 3.6 shows the expenditure of the HPVT-Regen system research. This research cost approximately CAD 2910.25.

**Table 3.6: Total expenditure of the HPVT-Regen research**

SI No	Material/Equipment	Quantity	CAD
1	Flexible solar panel	1	77.48
2	Regen PVs	4	36.84
3	Wooden frame	1	100
4	Black solar absorber sheet	0.14 m × 1 m	85.15
5	Steel channel	1	20
6	Brass ¼ pipes	2	18
7	Air blower	1	18
8	K thermocouples	2	56
9	Thermometers	1	150
10	Electrical load box	1	121.78
11	Extech multi-meters	3	1080
12	Pyranometer	1	265
13	Solmetric PV analyzer	1	850
14	Insulation tape	1	12
15	Electrical wires	15	20
<b>Total Cost</b>			<b>CAD 2910.25</b>

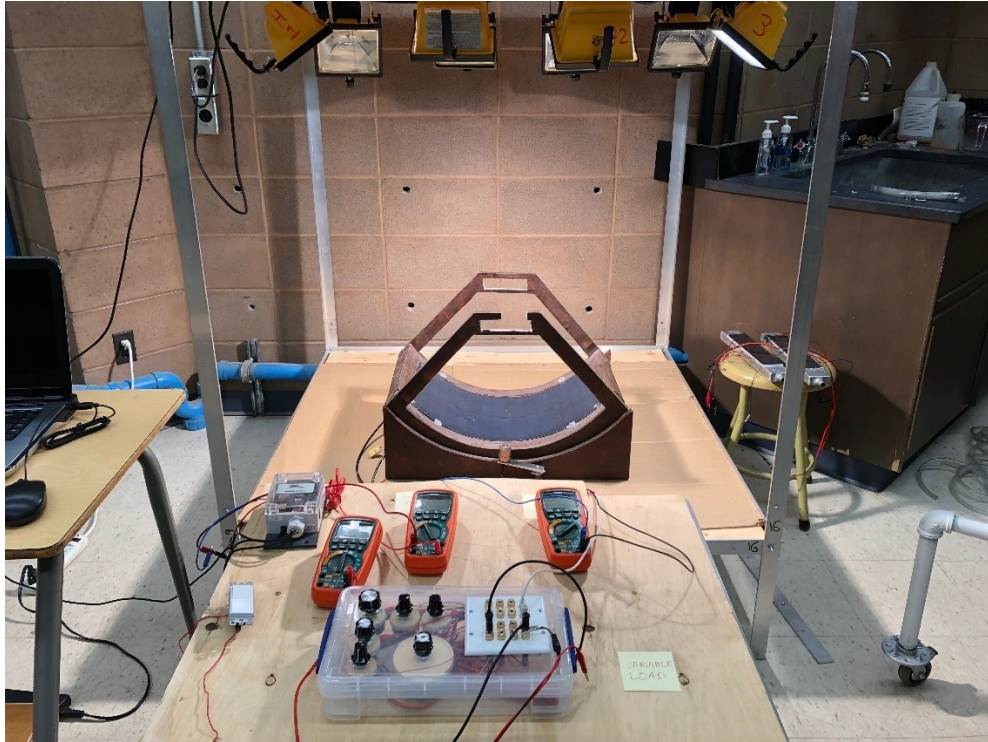


Figure 3.12: A photograph showing the solar simulator with halogen lamps used for the indoor testing.

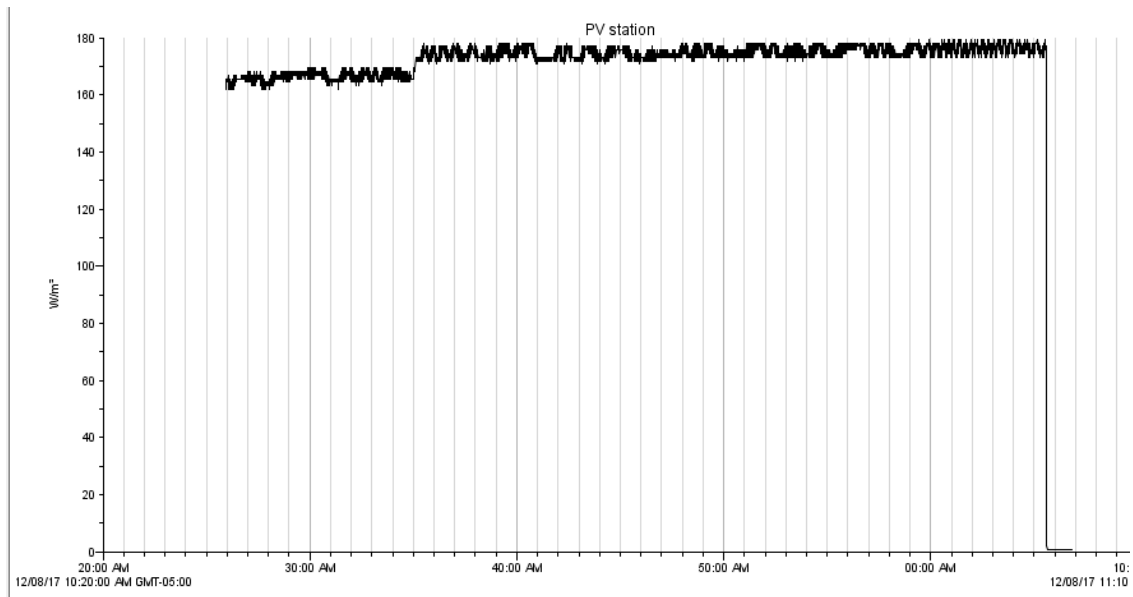


Figure 3.13: Pyranometer reading of the solar irradiation on the horizontal plane of the simulator.

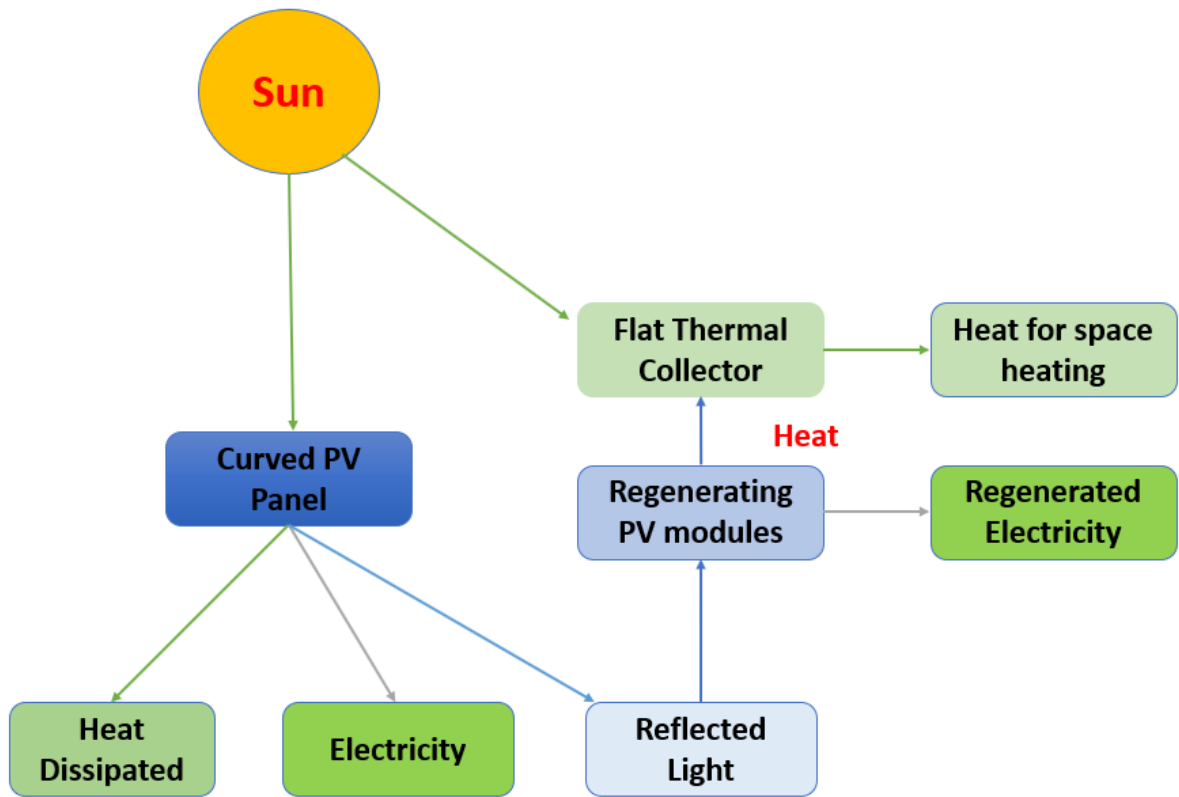


Figure 3.14: Energy flow diagram of the HPVT-Regen system used in this research work.

## Chapter 4: Indoor Laboratory Simulations, Results & Discussion

The previous chapter discussed the design of the HPVT-Regen system, construction of various structures, assembling, instrumentation and the energy balance of the HPVT-Regen system. The design aspects described photovoltaic subsystem, thermal subsystem, and regeneration subsystem assembled on a wooden frame. This chapter gives the details of experimental work done under indoor laboratory solar simulator lights, the experimental test results, and discussions. The curved-PV panel and regen-PV array is characterized for I-V and P-V curves and the thermal system is tested for air temperature rise for a constant airflow rate.

### 4.1 Measuring I-V Curves-Kelvin Circuit

Kelvin configuration or 4-wire circuit is the best configuration for measuring I-V characteristics on solar cells. The circuit is shown in **Figure 4.1**. The circuit that connects ammeter and variable load is called the **source lead** and the current flows through the source lead. The voltage is measured through the circuit parallel across the solar cell and is called the **sense lead**. Since no current flows through the sense lead because of high input impedance, the voltage measured is purely across the solar cell. Instead of a 4-wire circuit, if a 2-wire configuration is used to measure I-V curves, the current flowing through the load will cause a voltage drop in addition to the potential drop across the solar cell.

The flexible PV panel was tested for I-V characteristics in horizontal as well as in curved positions using Kelvin circuit configuration. Both the horizontal as well as the curved positions of the PV panel resulted identical results. Thus, using the flexible PV panel in curved position does not reduce the PV performance but also facilitates the concentration of reflected light to the regeneration subsystem of the HPVT-Regen system. **Figure 4.2** shows the I-V characteristics of the curved-PV panel measured by varying the electric load and recording the changes in current and voltage.

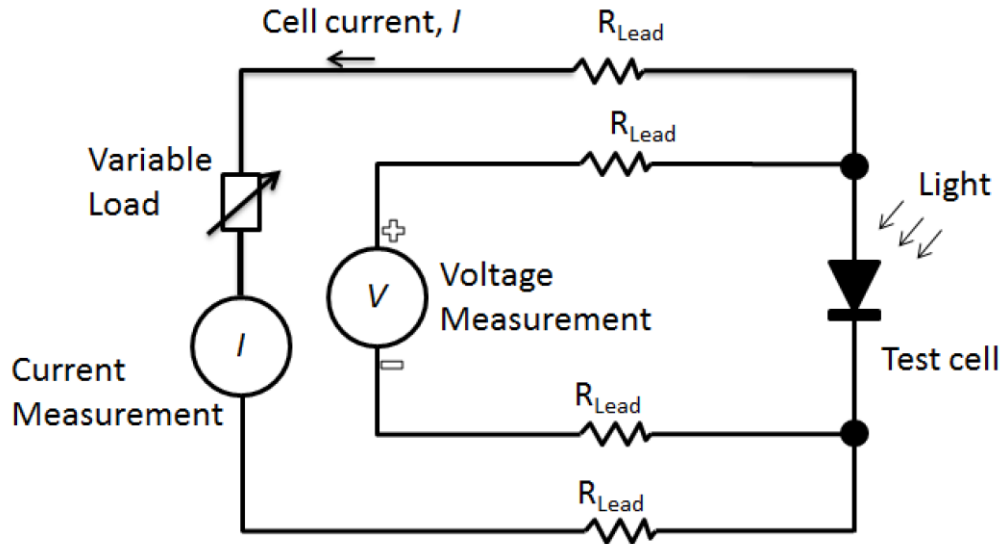


Figure 4.1: Kelvin Configuration or 4 wire circuit for measuring I-V curves of a solar cell [58].

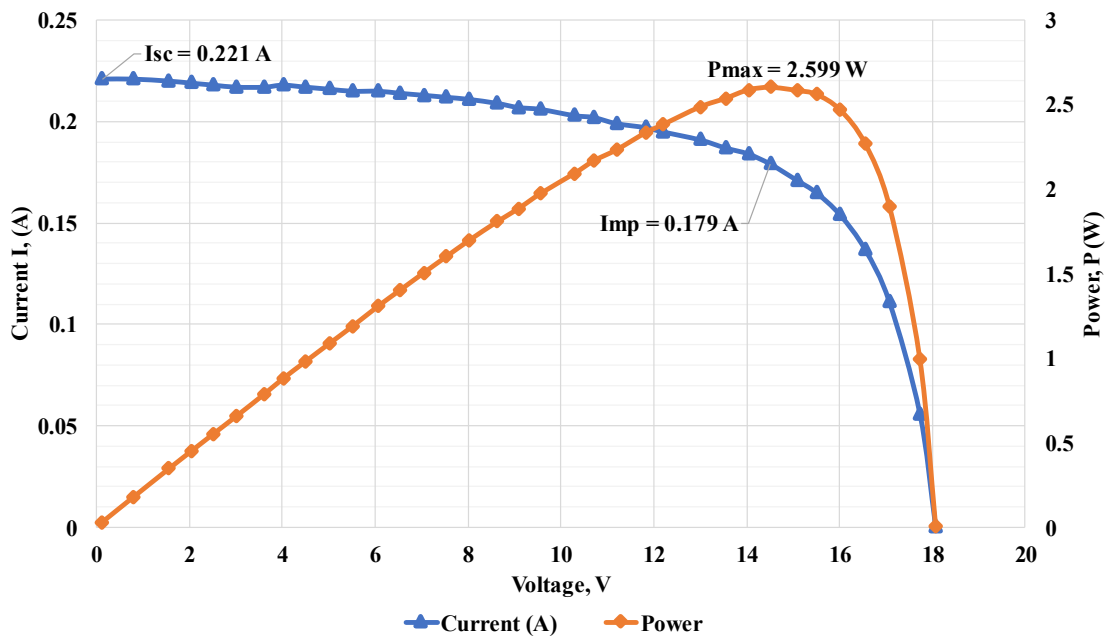


Figure 4.2: I-V characteristics of the curved-PV panel subsystem under indoor solar simulator.

### 4.1.1 Analysis of the Curved-PV Panel

Incident solar radiation = 173.039 W/m<sup>2</sup>

Area of curved-PV panel,  $A_{cpv} = 0.116 \text{ m}^2$

Total incident radiation on PV panel,  $P_{in} = 173.039 \left( \frac{W}{m^2} \right) \times 0.116 \text{ (m}^2) = 20.07 \text{ W}$

Voltage at max power,  $V_{mp} = 15.521 \text{ V}$

Current at max power,  $I_{mp} = 0.179 \text{ A}$

Open circuit voltage,  $V_{OC} = 18.083 \text{ V}$

Short circuit current,  $I_{OC} = 0.221 \text{ A}$

Maximum power obtained using equation 1.14,  $P_{max} = 2.599 \text{ W}$

The fill factor is given by the equation 1.15,

$$FF = \frac{I_{mp} \times V_{mp}}{I_{sc} \times V_{oc}} = \frac{0.179 \times 15.521}{0.221 \times 18.083} = 0.70$$

The efficiency of PV,

$$\eta_{pv} = \frac{P_{max}}{P_{in}} \times 100$$

$$\eta_{c.pv} = \frac{2.599 \text{ W}}{20.07 \text{ W}} \times 100 = 12.95 \%$$

The efficiency is slightly increased from 12.33% to 12.95% when changed the arrangement from horizontal position to curved trough. The reason is attributed to the fact that, the height of the system increased slightly because of the wooden trough which brings the PV panel closer to the light source. Moreover, there is multiple reflections within the panel because of the cylindrical structure.

### 4.1.2 Analysis of the Regen-PV Array

The four regenerating PV modules in parallel combination arranged at the bottom surface of the thermal subsystem is tested for I-V characteristics under reflected light using the 4 wire Kelvin circuit. **Figure 4.3** shows the I-V characteristics obtained when tested under the reflected light. The I-V characteristics has some shape abnormalities due to some instability working under the reflected light.

The intensity of reflected light measured by pyranometer = 25.5 W/m<sup>2</sup>

Percentage reflected from direct irradiance = 14.73%

Area of the regenerating array,  $A_{rpv} = 0.0156 \text{ m}^2$

Therefore, input power,  $P_{in} = 25.5 \left(\frac{\text{W}}{\text{m}^2}\right) \times 0.0156(\text{m}^2) = 0.398 \text{ W}$

Maximum Power obtained,  $P_{max} = 0.01704 \text{ W}$

Voltage at max power,  $V_{mp} = 2.763 \text{ V}$

Current at max power,  $I_{mp} = 0.0617 \text{ A}$

Open circuit voltage,  $V_{oc} = 4.098 \text{ V}$

Short circuit current,  $I_{sc} = 0.0795 \text{ A}$

The fill factor is given by the equation 1.15,

$$FF = \frac{I_{mp} \times V_{mp}}{I_{sc} \times V_{oc}} = \frac{0.0617 \times 2.763}{0.0795 \times 4.098} = 0.52$$

The efficiency of PV,

$$\eta_{regen\_pv} = \frac{P_{max}}{P_{in}} \times 100 = \frac{0.01704}{0.398} \times 100 = 4.28 \%$$

The regen-PV array obtained an electrical efficiency and electric power of 4.28% and 17.04 mW compared to 12.54% and 0.338 W at direct illumination respectively. The Hybrid system regenerated 14.73% of incident radiation and contributed less than 1% more electric power per unit area compared to individual systems working side by side.



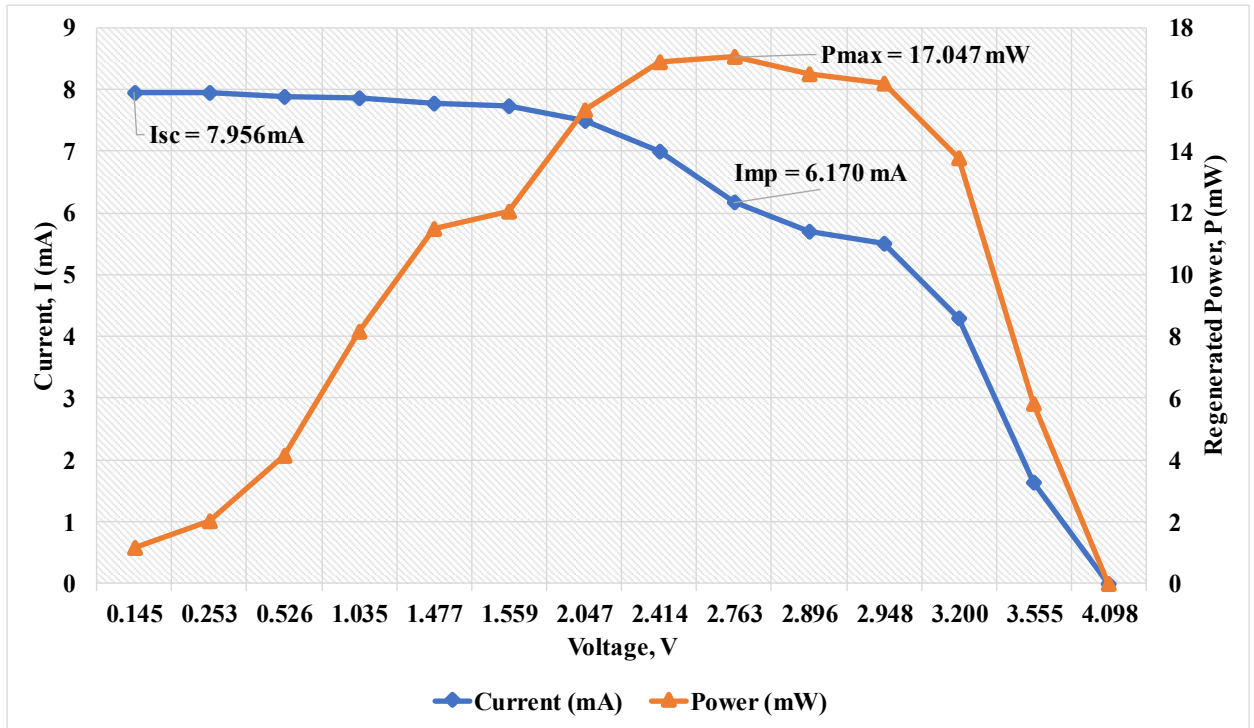


Figure 4.3: I-V characteristics of the regen-PV array tested under the reflected light.

## 4.2 Testing of the Thermal Subsystem

As shown in Figure 4.4, a blower forces air to flow through the thermal collector. The rotameter regulates and measures the air flow rate. K type thermocouples are used to measure temperatures at the blower, inlet and outlet of the thermal collector. **Figure 4.4** shows a thermal image of the thermal collector taken with an IR camera when no lights are irradiated but the blower is circulating the air. The thermal image shows that some heat is being added to the thermal collector by the blower motor. Also, when the thermal collector is being irradiated, the thermocouples intended to measure the air temperature is heated externally by the radiation. This mandates the calibration of the thermal collector subsystem to eliminate

- I. Heat carried by the air from the blower to the inlet up to the exit of the thermal system.
- II. Heat added to the thermocouples by the solar simulator lights.

Thus, the tests were conducted in 4 steps at an air flow rate of  $2.95 \times 10^{-4} \text{ m}^3/\text{s}$ ,

- I. The thermal collector was tested for 20 minutes measuring the temperature values at the inlet and outlet without the radiation but only air blower heating the air. **Figure 4.5a** is a graph of air temperature difference between outlet and inlet. The curve is a negative curve indicating that the outlet temperature is lower than the inlet temperature. The blower adds 7.1 °C to inlet air and dissipates to 2.1 °C to exit air by the end of 20 minutes.
- II. The thermal collector was tested for 20 minutes measuring the temperature values at the inlet and outlet with the simulator radiation but no air blower heating the air. **Figure 4.5b** is a graph of air temperature difference between outlet and inlet. Thermocouples intended to measure air temperature is affected by light exposure. Lights heats up inlet thermocouple by 11.2 °C and exit thermocouple by 7.9 °C. The curve is a negative curve indicating that the outlet temperature is lower than the inlet temperature. This is only because of the non-uniformity in radiation in the simulator test area.



Figure 4.4: Thermal image of the thermal collector when only air blower is circulating the air.

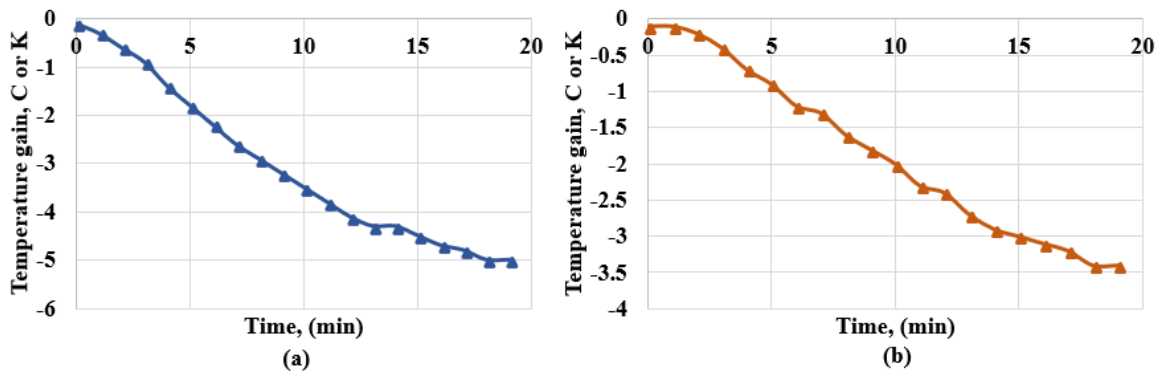


Figure 4.5: Air temperature gain curve between the inlet and outlet of the thermal collector (a) when only air blower is running, (b) when only radiation is heating the thermocouples.

III. The thermal collector was tested for 20 minutes measuring the temperature values at the inlet and outlet with the simulator radiation and the air blower running. This is the actual complete running of the thermal collector. **Figure 4.6** is a graph of air temperature difference between outlet and inlet. The measurement indicates a rise of 2.6 °C on air by the end of 20 minutes. The graph is a positive curve indicating that the outlet air temperature is higher than the inlet air temperature.

For the calibration, all the curves of air temperature difference are combined, and the effects of blower and thermocouple heating were subtracted. **Figure 4.7** shows the compilation of the various air temperature difference curves for the calibration. The figure shows a red thicker curve, which is the actual air temperature difference obtained between the outlet and the inlet of the thermal collector. This graph is separately shown in **Figure 4.8** as well. The calibrated curve indicates that there is a rise of 11 °C in the air by the simulator radiation with an air flow rate of  $2.95 \times 10^{-4} \text{ m}^3/\text{s}$ .

IV. The heat regenerated from the reflected light is measured by the same experiment steps by insulating the top surface of thermal collector. **Figure 4.9** shows the temperature gain by the air solely by the reflected light after calibration. The test results show that, out of the 11 °C rise in air temperature, 3 °C rise is contributed by the reflected light. Thus, the regeneration subsystem regenerated 3 °C of temperature on air at volumetric flow rate of  $2.95 \times 10^{-4} \text{ m}^3/\text{s}$ .

The thermal power output from the solar collector is given by,

$$P_{th} = \dot{m} C_{p,air} [T_{out} - T_{in}] \quad (4.1)$$

The air mass flow rate measured by the rotameter,  $\dot{m} = 3.61 \times 10^{-4} \text{ Kg/s}$

The specific heat of air,  $C_{p,air} = 1005 \text{ J/KgK}$

Temperature gain by the collector,  $T_{out} - T_{in} = 11 \text{ °C or K}$

$$P_{th} = 3.924 \text{ W}$$

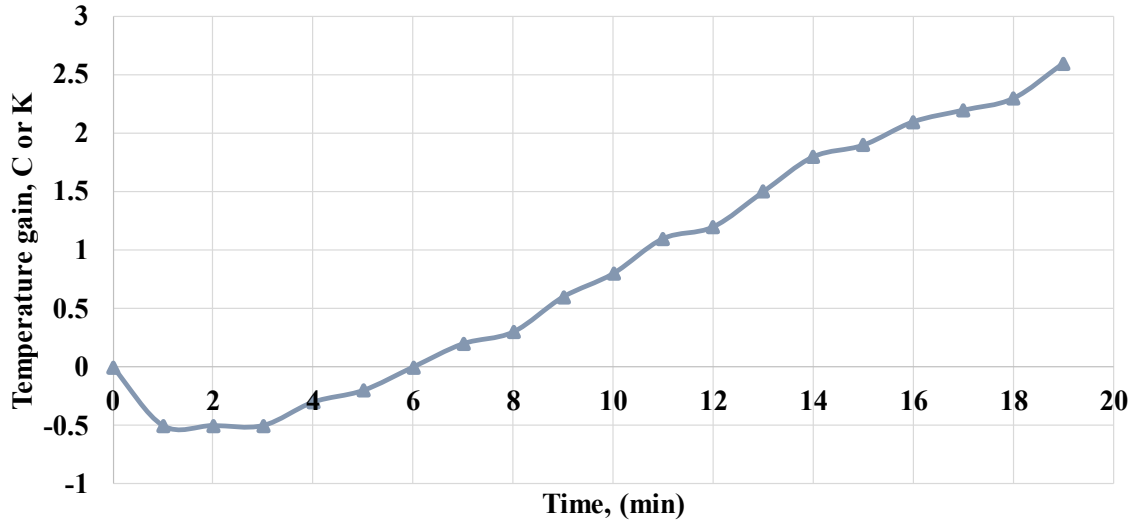


Figure 4.6: Air temperature gain between outlet and inlet of the thermal collector measured on actual running without calibration.

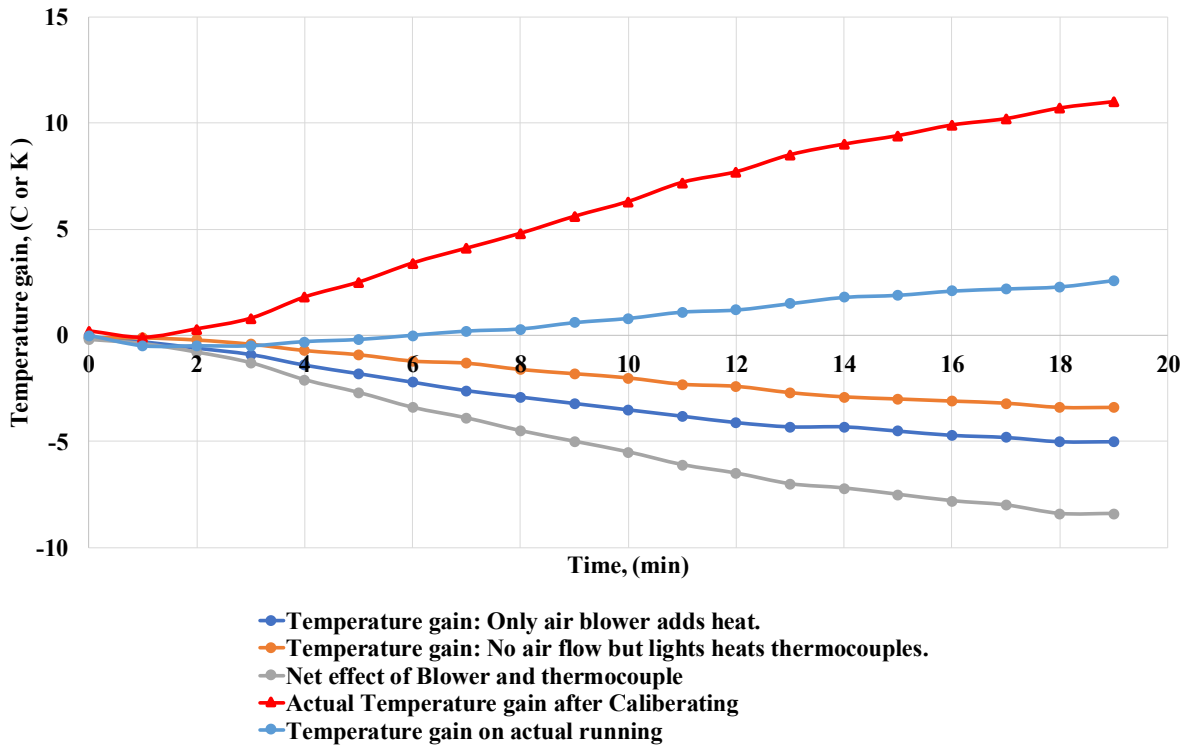


Figure 4.7: Compilation of the air temperature gain curves obtained in indoor testing showing the calibration.

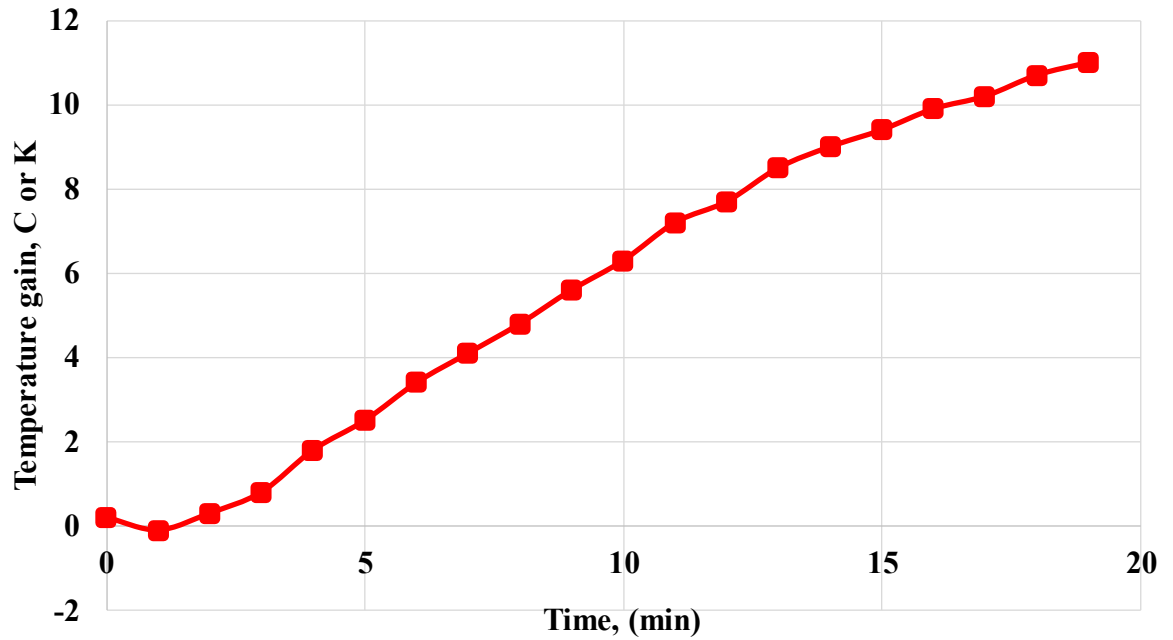


Figure 4.8: Actual air temperature gain under simulator lights after calibration.

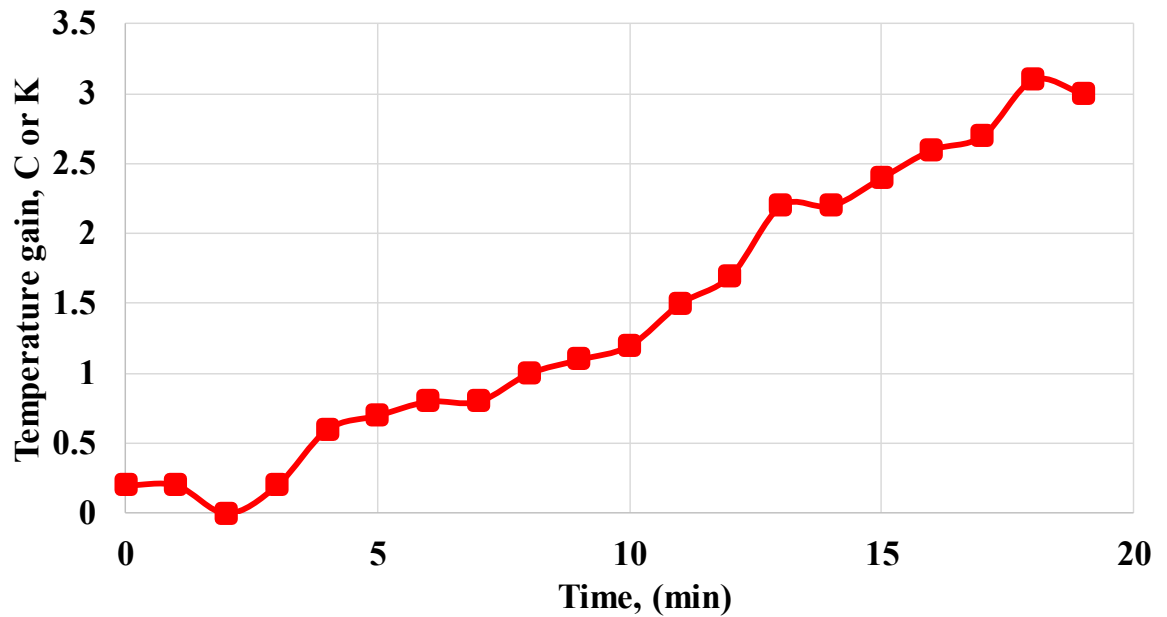


Figure 4.9: Air temperature gain contributed solely by the reflected light in indoor testing.

### 4.3 Infrared Analysis of the Irradiated Surfaces

To study the thermal radiation absorbed and emitted by various surfaces, thermal images of the thermal collector were captured using a FLIR IR camera. The thermal images of the black absorber and the regen-PV array were captured to calculate the input thermal radiation from the simulator and curved-PV panel (reflected radiation) respectively. To capture the thermal images, the IR camera is calibrated for each measuring surfaces. The emissivity values of each surface material are differently set in the camera before capturing. **Figure 4.10** shows the thermal images of black absorber and regen-PV array. The emissivity value is set to 0.08 for the black absorber surface and 0.30 for the regen-PV (silicon) surface.

The temperature of the top and bottom surfaces determined by the thermal camera are 130 °C and 67.1 °C respectively. Using the Stefan-Boltzmann equation, the total thermal radiation received by the thermal collector is

$$P_{in,th} = \sigma A[\varepsilon_1(T_{SA})^4 + \varepsilon_2(T_{SB})^4] \quad (4.2)$$

Where, Boltzmann constant,  $\sigma = 5.67 \times 10^{-8} \text{ W/m}^2\text{K}^4$ .

Area of the radiated surface,  $A_s = 0.03\text{m}^2$ .

Calibration temperature due to air blower,  $T_{cal} = 5.0 \text{ K}$

Temperature of the top black surface,  $T_{SA} = 397.6 \text{ K}$

Temperature of the bottom surface,  $T_{SB} = 334.7 \text{ K}$

Emissivity of the top black surface,  $\varepsilon_1 = 0.08$

Emissivity of the bottom Si surface,  $\varepsilon_2 = 0.30$

$$P_{in,th} = 5.67 \times 10^{-8} \times 0.03 [0.08(397.6)^4 + 0.30(334.7)^4]$$

$$P_{in,th} = 9.804 \text{ W}$$

The thermal collector receives 9.804 W of thermal power from the simulator lights when tested for 20 minutes. Based on calculations from equations 4.1 and 4.2, the thermal system obtained a thermal efficiency of 40.58%.



Figure 4.10 a: Infrared image of the top black surface captured with FLIR IR camera calibrated for the surface emissivity for indoor testing.

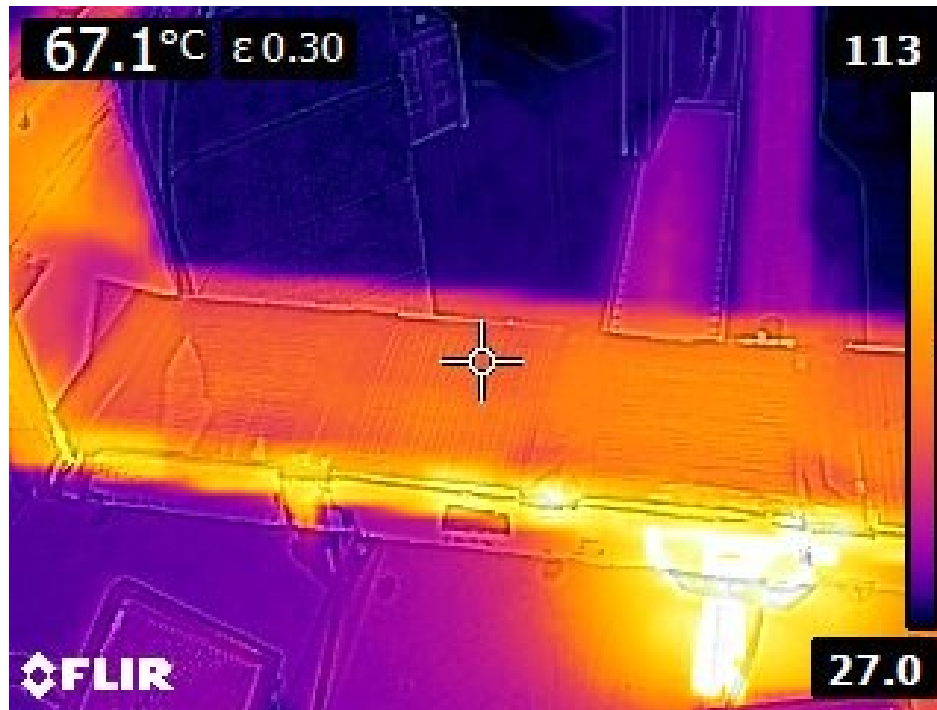


Figure 4.10 b: Infrared image of bottom regen-PV array captured with FLIR IR camera calibrated for silicon surface emissivity for indoor testing.



## 4.4 Overall Efficiency of HPVT-Regen System under Solar Simulator Lights

The total power generated by the HPVT-Regen system is the sum of electric power produced by curved-PV, electric power produced by regen-PV, and thermal power delivered by air.

$$P_{total} = P_{cpv} + P_{regen\ pv} + P_{th} \quad (4.3)$$

The power produced by curved-PV panel,  $P_{cpv} = 2.599$  W.

The power density of the curved-PV panel,  $p_{cpv} = 22.4$  W/m<sup>2</sup>.

The power produced by the regen-PV array,  $P_{regen\ pv} = 17.040$  mW.

The power density of the regen-PV array,  $p_{regen\ pv} = 1.09$  W/m<sup>2</sup>.

The power produced by the thermal collector,  $P_{th} = 3.997$  W.

The power density of the thermal collector,  $p_{th} = 133.23$  W/m<sup>2</sup>.

Irradiation measured by the pyranometer,  $p_{in} = 173.04$  W/m<sup>2</sup>.

Total power density,

$$P_{total} = 22.4 + 1.09 + 133.23 = 156.72 \text{ W/m}^2.$$

Thus, the overall efficiency of the system is,  $\eta_{overall} = 90.6\%$ .

### 4.4.1 Power Regeneration by HPVT-Regen System

The reflection loss of the incident radiation is 14.73%. The HPVT-Regen system regenerated 17.04 mW of electric power with an electrical efficiency of 4.28% and contributed less than 1% more electric power per unit surface area compared to individual side by side systems. The thermal collector raised the temperature of air flowing at  $2.95 \times 10^{-4}$  m<sup>3</sup>/s by 3 °C from the reflected light with a thermal efficiency of 16.94% and contributed 34.49% more thermal power per unit surface area compared to individual side by side systems.

## Chapter 5: Outdoor Actual Experimental Tests, Results & Discussion

Real-time characterization of the fully assembled and instrumented HPVT-Regen system is performed under outdoor solar radiation conditions of Thunder Bay, Ontario. This chapter presents the outdoor tests, results, and discussion of the HPVT-Regen system. The tests were conducted for 20 minutes in two phases on two days of the same week at the same time. The first phase tested the performance of curved-PV panel, regen-PV array, and thermal collector for full running of the system (**Figure 5.1**). The second phase temperature measurements with insulated top surface of the thermal collector studied the contribution of reflected light on the temperature of the air.

### 5.1 Performance of the Curved-PV Panel

The curved-PV panel was tested under solar radiation of Thunder Bay's weather conditions on July 2<sup>nd</sup>, 2018 from 14:00 to 14:20 oriented towards the North-South direction of the earth. The measurements were taken using Solmetric PVA-600V PV-Analyzer for maximum power points obtained from the PV panel. **Figure 5.2** shows the variation of maximum power with the solar radiation. In the figure, the sudden drops in irradiation and power are due to intermittent sky clouds. **Table 5.1** shows the irradiation and other performance parameters. **Figure 5.3** shows the I-V characteristics of the curved panel for the instant of highest power obtained during the 20 minutes test.

Highest incident solar radiation =  $1030 \text{ W/m}^2$

Area of curved-PV panel,  $A_{cpv} = 0.116 \text{ m}^2$

Total incident radiation on PV panel,  $P_{in} = 1030 \left( \frac{\text{W}}{\text{m}^2} \right) \times 0.116 (\text{m}^2) = 119.48 \text{ W}$

Maximum power measured with PV analyzer,  $P_{max} = 4.345 \text{ W}$

The efficiency of PV using equation 1.17,

$$\eta_{c-pv} = \frac{4.345 \text{ W}}{119.48 \text{ W}} \times 100 = 3.63 \%$$

The curved-PV panel produced an average electric power of 2.93 W with an average electrical efficiency of 3.40 % under an average irradiation of  $814.4 \text{ W/m}^2$ .



Figure 5.1: A photograph of the fully instrumented test set up under solar radiation in Thunder Bay, Ontario.

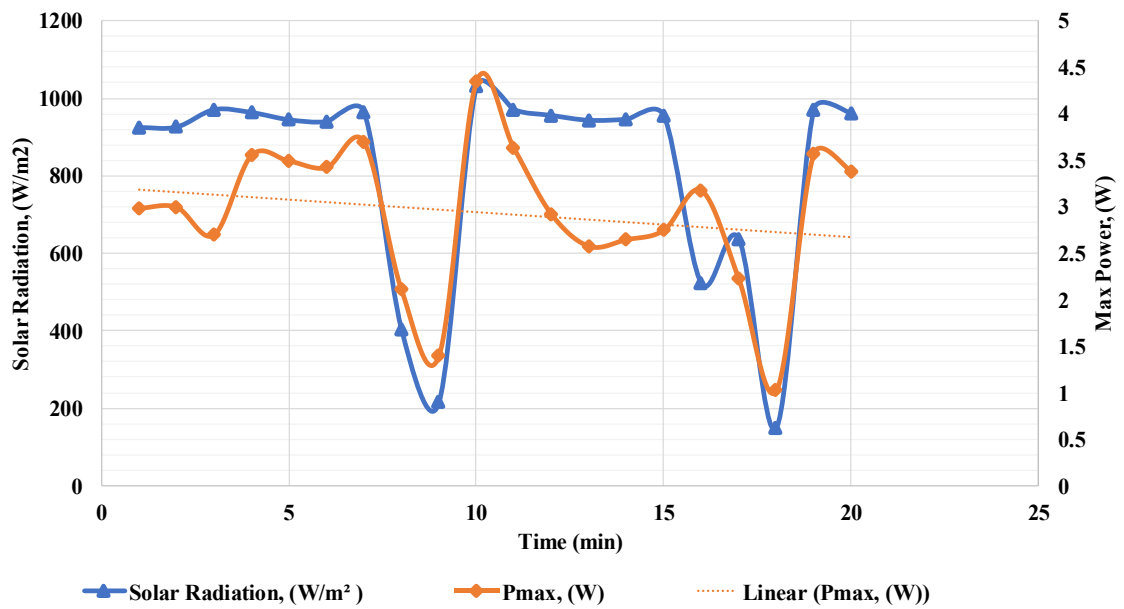


Figure 5.2: Variation in maximum power of the curved-PV panel with respect to solar radiation for 20 minutes.

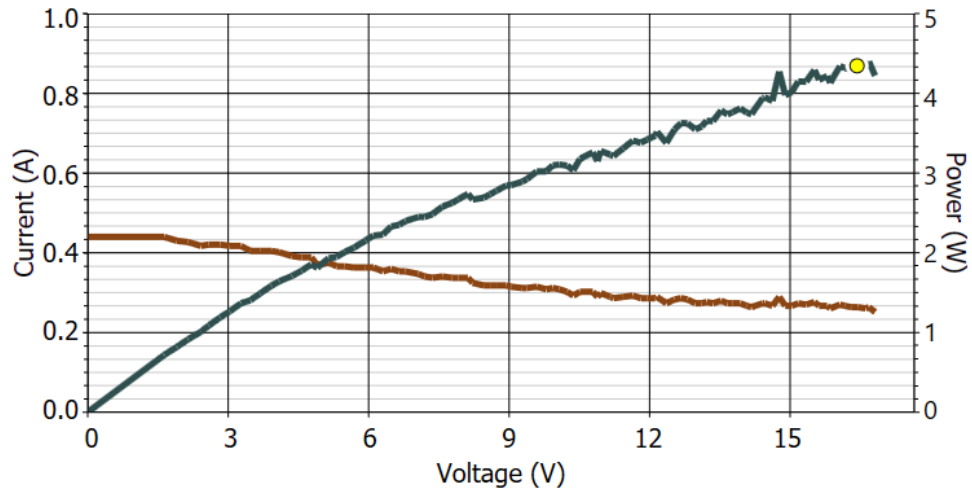


Figure 5.3: I-V characteristics of the curved-PV panel for the instant of highest maximum power obtained, measured by Solmetric PVA-600V PV-Analyzer.

**Table 5.1: Irradiation and performance parameters of the curved-PV panel measured by Solmetric PVA-600V PV Analyzer.**

Solar Radiation, (W/m <sup>2</sup> )	$P_{max}$ (W)	$V_{mp}$ (V)	$I_{mp}$ (A)	$V_{oc}$ (V)	$I_{sc}$ (A)	Efficiency (%)
924.4	2.98	13.63	0.21	19.06	0.38	2.78
925.6	3.00	14.67	0.20	19.08	0.37	2.79
970.6	2.70	13.09	0.20	18.8	0.30	2.40
963.1	3.55	15.13	0.23	19.34	0.39	3.18
944.4	3.49	14.71	0.23	19.29	0.38	3.19
939.4	3.42	14.16	0.24	19.24	0.37	3.14
964.4	3.70	14.71	0.25	19.31	0.40	3.31
403.1	2.11	10.61	0.19	18.26	0.26	4.51
214.4	1.40	7.837	0.17	17.69	0.18	5.62
1030.6	4.35	16.43	0.26	19.49	0.44	3.63
970.6	3.63	18.34	0.19	19.41	0.42	3.22
955.6	2.92	14.73	0.19	19.33	0.40	2.63
943.1	2.58	10.53	0.24	19.27	0.40	2.35
945.6	2.65	10.04	0.26	19.25	0.40	2.41
954.4	2.75	10.12	0.27	19.26	0.41	2.48
521.9	3.18	15.59	0.20	19.32	0.44	5.24
636.9	2.22	11.12	0.20	18.32	0.26	3.01
148.1	1.02	6.571	0.15	17.67	0.16	5.94
970.6	3.57	16.63	0.21	19.64	0.47	3.17

## 5.2 Performance of the Regen-PV Array

From measurements of pyranometers, 14.31% of the incident light is reflected to the regeneration subsystem. The regen-PV array irradiated by the reflected light was characterized using the four-wire Kelvin circuit by varying the electrical load. The characterization test of the Regen-PVs under solar radiation was relatively more stable than the indoor testing. The I-V characteristics of the regen-PV array is shown in **Figure 5.4**. The I-V characteristics have a standard shape with measurements being stable.

The intensity of reflected light measured by pyranometer = 127.75 W/m<sup>2</sup>

Percentage reflected from direct irradiance = 14.73%

Area of the regenerating array,  $A_{rpv} = 0.0156 \text{ m}^2$

Therefore, input power,  $P_{in} = 127.75 \left(\frac{\text{W}}{\text{m}^2}\right) \times 0.0156(\text{m}^2) = 1.99 \text{ W}$

Maximum Power obtained,  $P_{max} = 137.64 \text{ mW}$

Voltage at max power,  $V_{mp} = 3.720 \text{ V}$

Current at max power,  $I_{mp} = 0.037 \text{ A}$

Open circuit voltage,  $V_{oc} = 4.542 \text{ V}$

Short circuit current,  $I_{sc} = 0.043 \text{ A}$

The efficiency of PV,

$$\eta_{regen\_pv} = \frac{P_{max}}{P_{in}} \times 100 = \frac{0.13764}{1.99} \times 100 = 6.91 \%$$

The Regen-PV array produced an electric power of 0.137 W with an electrical efficiency of 6.91% contributing to approximately 3.167% more electric power per unit PV surface area. A comparison of performance parameters of curved-PV panel and regen-PV array in indoor simulation and outdoor real-time characterization is shown in **Table 5.2**. From the table, the outdoor performance is better than indoor simulation. Identical values of percent reflection is in agreement with the optical properties of curved-PV panel.

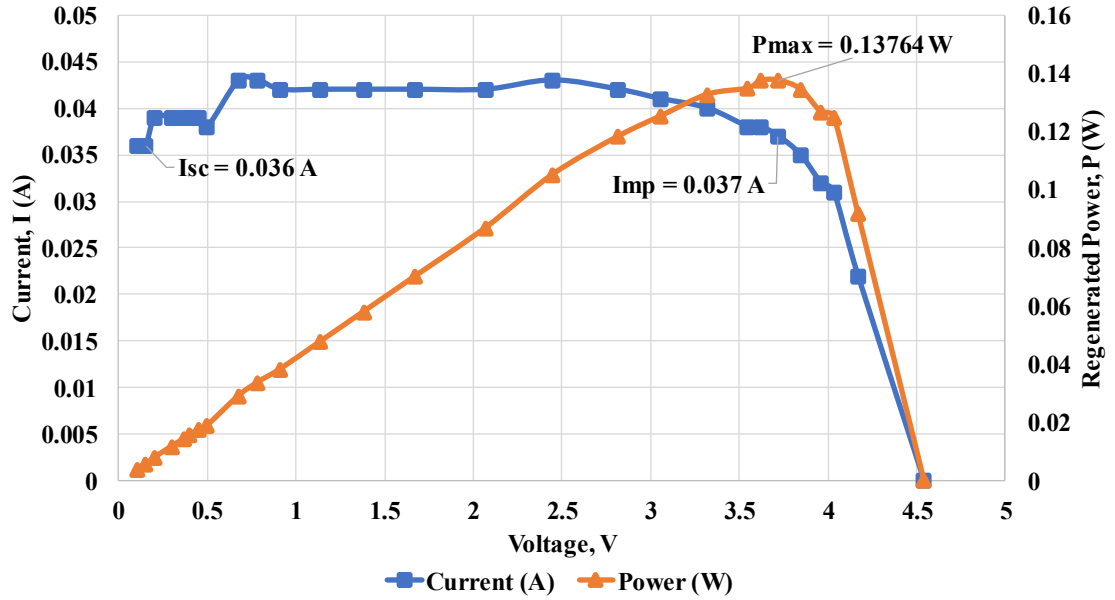


Figure 5.4: I-V characteristics of the regen-PV array obtained while testing under outdoor solar radiation.

**Table 5.2: Comparison of performance parameters of the electrical subsystem of the HPVT-Regen system for indoor and outdoor testing.**

Parameters	Indoor testing	Outdoor testing
Irradiation, $P_{in,pv}$	173.039 W/m <sup>2</sup>	892.54 W/m <sup>2</sup>
Reflected solar radiation, $P_{in,regn}$	25.5 W/m <sup>2</sup>	127.75 W/m <sup>2</sup>
Percentage reflection	14.73 %	14.31 %
Max power: curved-PV, $P_{max,pv}$	2.599 W	4.345 W
Electrical efficiency: curved-PV	12.95%	3.63 %
Max power: Regen-PV, $P_{max,regen}$	17.04 mW	137.64 mW
Electrical efficiency: Regen-PV	4.28 %	6.90 %
Regeneration of electric power	< 1%	3.16 %

### 5.3 Performance of the Thermal Subsystem

The air type thermal collector was tested for temperature gain at a volumetric flow rate of  $2.95 \times 10^{-4} \text{ m}^3/\text{s}$  for 20 minutes at the same time curved-PV panel and regen-PV array were tested. As in indoor testing, the actual air temperature gain was determined after calibration eliminating blower heat and thermocouple heat. Since the thermocouples were uniformly exposed to solar radiation, the thermocouple heating does not have any effect on calibration. **Figure 5.5** shows the compilation of temperature gain curves used to calibrate and **Figure 5.6** shows the actual temperature gain in air for the duration of test. From the experiment, it is measured that, the thermal collector was able to raise the temperature of the air by 9.3 °C by the end of 20 minutes. To study the performance of the thermal collector under reflected light, the top surface of the collector was insulated and tested on July 7<sup>th</sup>, 2018 from 14:00 to 14:20 at the same location and orientation. Since the days are on the same week, the solar radiation intensity can be approximated same. The test results are depicting the temperature gain graph is shown in **Figure 5.7**. The results show that the thermal collector was able to raise the temperature of the air by 2.4 °C by the end of 20 minutes.

The thermal power output from the solar collector is given by equation 4.1,

$$P_{th} = \dot{m} C_{p,air} [T_{out} - T_{in}]$$

The air mass flow rate measured by the rotameter,  $\dot{m} = 361.61 \times 10^{-6} \text{ Kg/s}$

The specific heat of air,  $C_{p,air} = 1005 \text{ J/KgK}$

Temperature gain by the collector,  $T_{out} - T_{in} = 9.3 \text{ °C or K}$

$$P_{th} = 3.379 \text{ W}$$

The IR images of the collector surfaces under solar radiation used to measure input thermal radiation are shown in **Figure 5.8**. The camera was calibrated for emissivity values of the black absorber and silicon respectively for the top and bottom surfaces. The temperature of the top and bottom surfaces determined by the thermal camera are 233.06 K and 333.56 °C respectively.

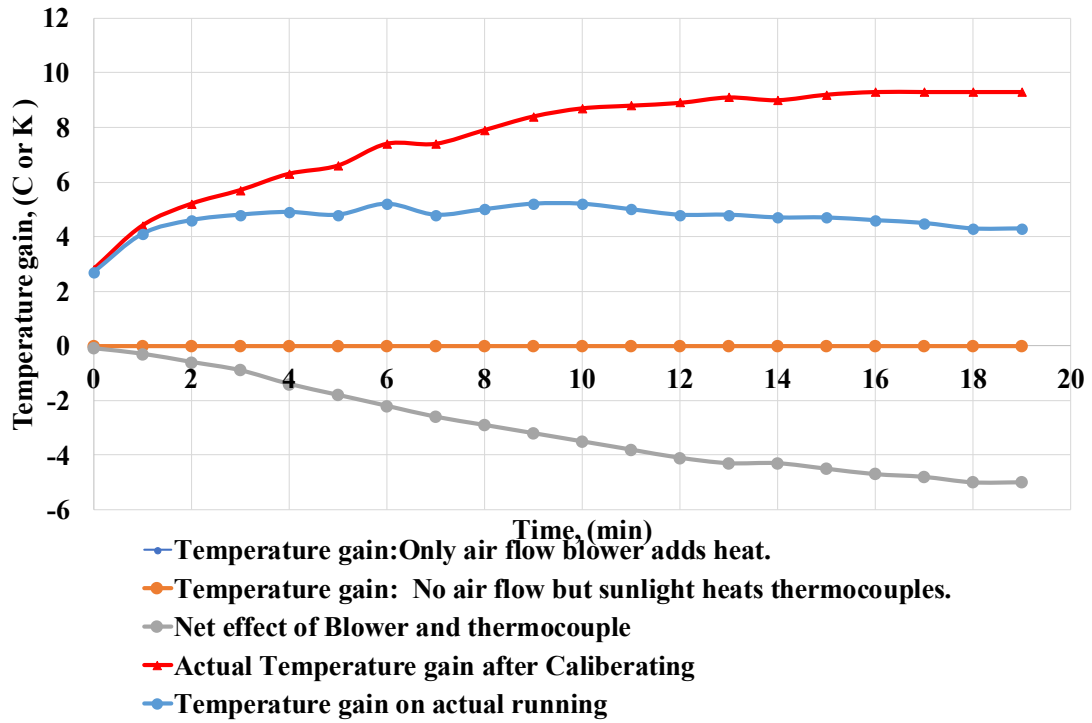


Figure 5.5: Compilation of the air temperature gain curves obtained in outdoor testing showing the calibration.

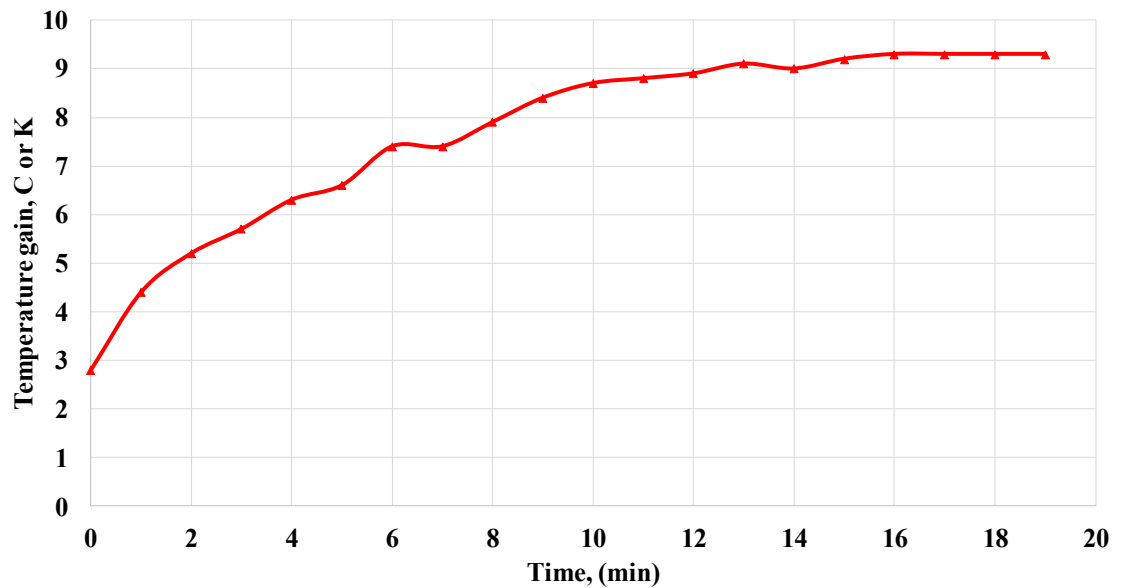


Figure 5.6: Actual air temperature gain after calibration obtained in outdoor testing.



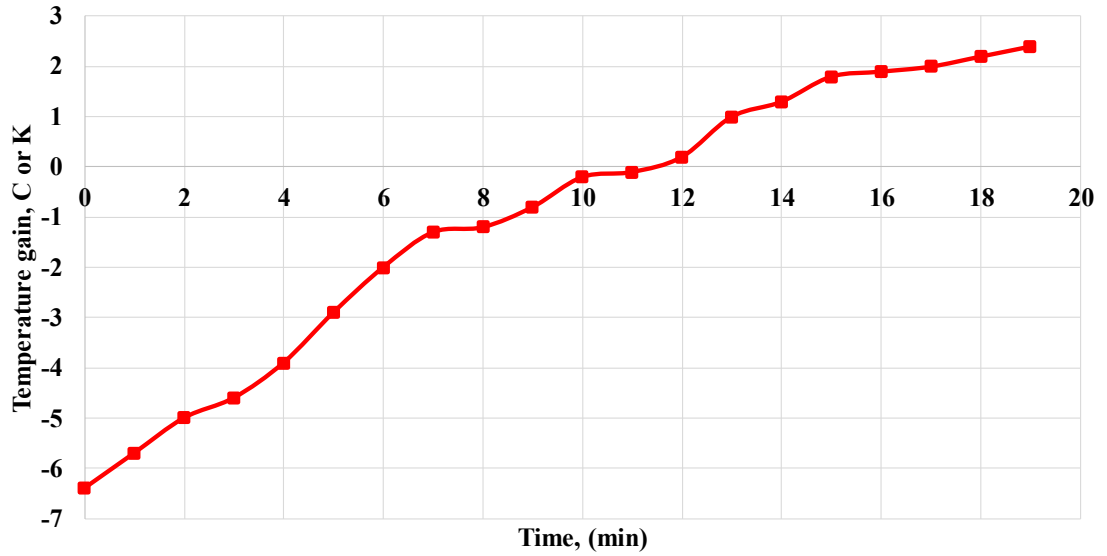


Figure 5.7: Air temperature gain solely due to reflected light obtained in outdoor testing.

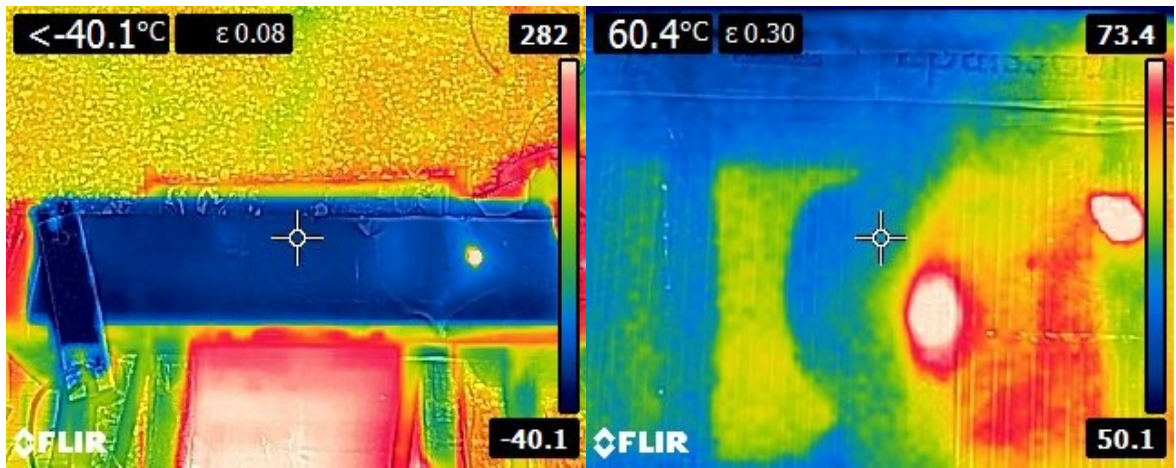


Figure 5.8: Thermal images of the top (left) and bottom (right) surfaces of the thermal collector taken with FLIR camera for outdoor simulation.

Using the Stefan-Boltzmann equation given by equation 4.2, the total thermal radiation received by the thermal collector is,

$$P_{in,th} = \sigma A[\varepsilon_1(T_{SA})^4 + \varepsilon_2(T_{SB})^4]$$

where, Boltzmann constant,  $\sigma = 5.67 \times 10^{-8} \text{ W/m}^2\text{K}^4$ .

Area of the radiated surface,  $A = 0.03\text{m}^2$ .

Calibration temperature due to air blower,  $T_{cal} = 5.0 \text{ K}$

Temperature of the top black surface,  $T_{SA} = 228.06 \text{ K}$

Temperature of the bottom surface,  $T_{SB} = 328.56 \text{ K}$

Emissivity of the top black surface,  $\varepsilon_1 = 0.08$

Emissivity of the bottom Si surface,  $\varepsilon_2 = 0.30$

$$P_{in,th} = 5.67 \times 10^{-8} \times 0.03 [0.08(228.06)^4 + 0.30(328.56)^4]$$

$$P_{in,th} = 6.315 \text{ W}$$

The thermal collector receives 6.315 W of thermal power from the simulator lights when tested for 20 minutes. Based on calculations from equations 4.1 and 4.2, the thermal collector obtained a thermal efficiency of 53.50%. A comparison of performance parameters of the HPVT-Regen thermal subsystem is shown in **Table 5.3**.

**Table 5.3: Comparison of performance parameters of the thermal subsystem of the HPVT-Regen system for indoor and outdoor testing.**

Parameters	Indoor testing	Outdoor testing
Total air temperature gain	11 °C	9.3 °C
Temperature gain due to reflected light	3 °C	2.4 °C
Thermal power	3.924 W	3.379 W
Thermal radiation	9.804 W	6.315 W
Thermal efficiency	40.58 %	53.50 %

## 5.4 Overall Efficiency of HPVT-Regen System under Solar Radiation

The total power generated by the HPVT-Regen system given by equation 4.3 is the sum of electric power produced by curved-PV, electric power produced by regen-PV, and thermal power delivered by air.

$$P_{total} = P_{cpv} + P_{regen\ pv} + P_{th}$$

The power produced by curved-PV panel,  $P_{cpv} = 4.345$  W.

The power density of the curved-PV panel,  $p_{cpv} = 37.456$  W/m<sup>2</sup>.

The power produced by the regen-PV array,  $P_{regen\ pv} = 137.640$  mW.

The power density of the regen-PV array,  $p_{regen\ pv} = 8.823$  W/m<sup>2</sup>.

The power produced by the thermal collector,  $P_{th} = 3.379$  W.

The power density of the thermal collector,  $p_{th} = 112.633$  W/m<sup>2</sup>.

Irradiation measured by the pyranometer,  $p_{in} = 892.540$  W/m<sup>2</sup>.

Total power density,

$$P_{total} = 37.456 + 8.823 + 112.633 = 158.909 \text{ W/m}^2.$$

Thus, the overall efficiency of the system is,  $\eta_{overall} = 17.80\%$ .

### 5.4.1 Power Regeneration by HPVT-Regen System

The reflection loss of the incident radiation is 14.31%. The HPVT-Regen system regenerated 137.64 mW of electric power with an electrical efficiency of 6.90% and contributed 3.16% more electric power per unit surface area compared to individual side by side systems. The thermal collector raised the temperature of air flowing at  $2.95 \times 10^{-4}$  m<sup>3</sup>/s by 2.4 °C from the reflected light with a thermal efficiency of 14.66% and contributed 34.77% more thermal power per unit surface area compared to individual side by side systems. Comparing to indoor testing, thermal regeneration in outdoor testing is identical as well and is 34%.

## 5.5 Uncertainty Analysis of the Experimental Results

The uncertainty in the experimentally measured and calculated results are given in **Table 5.4**. Uncertainty analysis of the measured variables is determined as follows. Let an instrument measures an independent parameter for  $N$  number of times as  $x_1, x_2, \dots, x_n$  for a given set of experimental conditions, then the uncertainty,  $\mu$  is given by

$$\mu_x = \pm \sqrt{\frac{\sum_{i=1}^n (x_i - \bar{x})^2}{N - 1}} \quad (5.1)$$

where,  $\bar{x}$  is the mean value of the parameter from  $N$  number of measurements. The uncertainty of a function is calculated by the method of Holman as follows.

Consider a function,  $F$  of multiple independent variables  $x, y,$  and  $z$ :

$$F = f(x, y, z, \dots) \quad (5.2)$$

then the uncertainty of the function  $F$  is given by

$$\mu_F = \pm \sqrt{\left(\frac{\partial F}{\partial x} \sigma_x\right)^2 + \left(\frac{\partial F}{\partial y} \sigma_y\right)^2 + \left(\frac{\partial F}{\partial z} \sigma_z\right)^2 + \dots} \quad (5.3)$$

The uncertainty in the measured values was analyzed using ‘‘Uncertainty Sidekick’’ software. An Extech wireless multimeter was used to measure the DC voltage and current from the curved-PV and regen-PVs, as well as the resistance of the electrical loads. The Extech multimeter has an uncertainty of 0.05%, 0.12%, and 1.5% in the measurements of DC voltage, current and resistance respectively. Solmetric PVA-600V PV-Analyzer was used to measure the real-time maximum power values of the curved-PV. The analyzer has an uncertainty of  $\pm 0.78$  W when tested for real-time maximum PV power measurement. The pyranometer used to measure solar irradiance has an uncertainty of 1.5%. K-type thermocouples with an operating temperature range of 0 to 500 °C are used to measure the air temperature at the blower, inlet, and outlet of the thermal collector. The uncertainty of the K-type thermocouples is  $\pm 0.71$  °C or 2.9% of the measured temperature. A rotameter used to measure the air flow rate to the thermal collector has an uncertainty of 0.34% of the measured flow rates. A FLIR infrared camera is used to record the thermal profile of the top and bottom surfaces of the thermal collector. The camera has a least count of 0.1 °C and uncertainty of 1.7%.

**Table 5.4: Uncertainty of experimentally measured and calculated parameters of the HPVT-Regen simulation.**

<b>Parameter</b>	<b>Instrumentation</b>	<b>Uncertainty</b>
DC voltage (V)	Extech wireless multimeter	0.05%
Current (A)	Extech wireless multimeter	0.12%
Load resistance ( $\Omega$ )	Extech wireless multimeter	1.5%
Electric power (W)	Solmetric PVA-600V PV-analyzer	$\pm 0.78$ W
Solar radiation ( $\text{W}/\text{m}^2$ )	Pyranometer	1.5%
Air temperature ( $^{\circ}\text{C}$ )	K-type thermocouple	$\pm 0.71$ $^{\circ}\text{C}$ or 2.9%
Air flow rate ( $\text{m}^3/\text{s}$ )	Rotameter	0.34%
Temperature profile ( $^{\circ}\text{C}$ )	FLIR-E4 IR camera	1.7%

# Chapter 6: Conclusion, Future Work and Recommendations

## 6.1 Conclusion

In this work, an experimental test setup of the hybrid photovoltaic-thermal system with regeneration (HPVT-Regen) was designed, built and fully instrumented to experimentally investigate the regeneration of optical losses from the photovoltaic subsystem. Detailed real-time tests were performed using the HPVT-Regen system under indoor solar simulations as well as under outdoor solar radiation of Thunder Bay climate conditions in order to characterize the electrical and thermal performance of the HPVT-Regen system.

The experimental results showed that the Regen-PV subsystem reflected approximately 14% of the incident radiation of the indoor as well as of the outdoor tests. The HPVT-Regen system regenerated this reflected light and converted into electrical and thermal power. The indoor setting regenerated 17.04 mW of electricity with an electrical conversion efficiency of approximately 4.3% and contributed with less than 1% more electric power per unit area. However, the outdoor setting regenerated 137.64 mW of electricity with an electrical conversion efficiency of 6.9% and contributed with 3.16 % more electric power per unit area. The thermal collector regenerated 3°C and 2.4°C of air temperature solely from the reflected radiation in the indoor and outdoor settings, respectively. Thermal collector contributed approximately 34% more thermal power per unit surface area compared to individual side by side systems in both indoor and outdoor test settings.

The indoor simulations achieved a total output power density of 156.72 W/m<sup>2</sup> with an overall conversion efficiency of approximately 91%, whereas the outdoor experimentation achieved a total output power density of 158.90 W/m<sup>2</sup> with an overall efficiency of 17.80%. Although, the power density obtained was higher in the outdoor testing, the HPVT-Regen system did not perform well under real solar radiation outdoor conditions. The reason is attributed to the lower power rating of the curved-PV panel.

Using a high rated PV panel of the same size would bring up the overall efficiency of the HPVT-Regen system making it applicable in practical situations. Therefore, it is suggested that more detailed outdoor testing is required in the future for further understanding this interesting performance phenomena.

## **6.2 Future Work and Recommendations**

From the experimental characterization, it is now evident that, regeneration of photovoltaic optical losses is practical and can be applied in various real-life engineering situations. The HPVT-Regen system can be improved by employing high rating flexible PV panels which has a high potential of generating electricity from high intensity solar radiations. The design can be improved to accommodate a variable focal length from the curved-PV panel to adjust the position of thermal collector to avoid shadows of the collector falling on PV panel with changing solar time and seasons. A solar tracking system with at least one degree of freedom for the whole hybrid system with various modifications in fixed parts can be implemented to maximize the power generation throughout a year. The HPVT-Regen system can be enhanced to a large scale in both size as well as in number to meet higher energy demands.

The HPVT-Regen system can be further tested with different working fluids other than air. Possibility of combining the HPVT-Regen with a Rankine cycle of low temperature working fluids like pentane and toluene is considered. The schematic diagram of a concept showing the incorporation of HPVT-Regen system for preheating the working fluid of a Rankine cycle is shown in Figure 6.1.

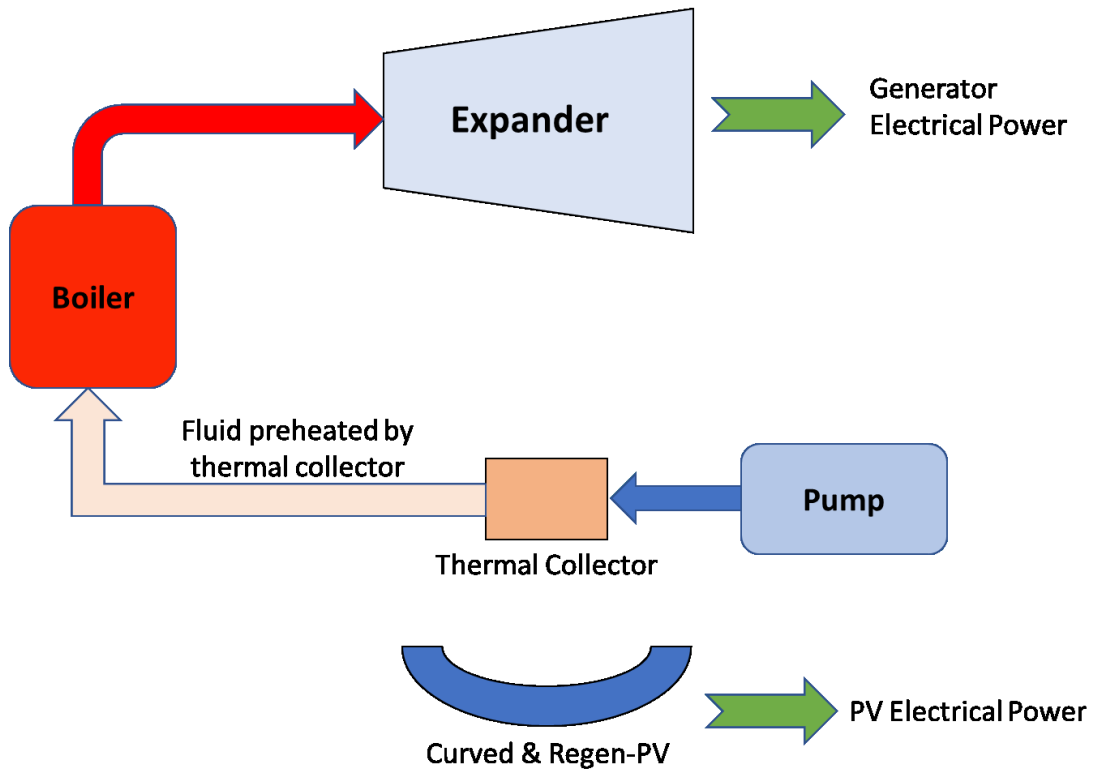


Figure 6.1 Schematic of a concept of combining HPVT-Regen system with a Rankine cycle for preheating the working fluid.



## References

- [1] J. Duffie and W. Beckman, *Solar Engineering of Thermal Processes. 2nd ed. John Wiley and Sons. New York: USA. 1991.*
- [2] Natural Resources Canada, “Renewable Energy | Natural Resources Canada,” 2014. [Online]. Available: <http://www.nrcan.gc.ca/statistics-facts/energy/895>. [Accessed: 28-May-2018].
- [3] Natural Resources Canada, “Canada – A Global Leader in Renewable Energy: Enhancing Collaboration on Renewable Energy Technologies,” in *Energy and Mines Ministers Conference*, no. August 2013, p. 14.
- [4] Green Rhino Energy, “Extraterrestrial Radiation | Solar Radiation,” 2016. [Online]. Available: <http://www.greenrhinoenergy.com/solar/radiation/extraterrestrial.php>. [Accessed: 15-May-2018].
- [5] U.S. Energy Information Administration, *International Energy Outlook*, vol. 0484, no. July. 2010.
- [6] I. R. E. Agency, “International Renewable Energy Agency,” no. December, pp. 25–30, 2013.
- [7] C. Honsberg and S. Bowden, “Solar Energy | PVEducation.” [Online]. Available: <http://www.pveducation.org/pvcdrom/introduction/solar-energy>. [Accessed: 10-May-2018].
- [8] C. Gueymard and D. Myers, *Modeling Solar Radiation at the Earth’s Surface*. Springer, 2008.
- [9] M. Iqbal, “Solar Radiation Measuring Instruments,” in *An Introduction to Solar Radiation*, Academic Press Canada, 1983, pp. 335–373.
- [10] K. Mertens, “Solar Radiation,” in *Photovoltaics: Fundamentals, Technology, and Practice*, John Wiley & Sons Ltd, 2014, p. 22.
- [11] A. A. Hosseini and S. H. Hosseini, “Utilizing Solar Energy Instead of Fossil Fuels

- as Domestic Energy (Case Study: Dehloran City, Ilam Province, Iran),” *Energy Exploration and Exploitation*, vol. 30, no. 3, pp. 389–401, 2012.
- [12] S. A. Kalogiru, “Solar Energy Collectors,” in *Solar Energy Engineering*, 2nd Edition, Academic Press, London, UK, 2009, pp. 132–133.
- [13] R.H.B.Exell, “Principles of Solar Thermal Conversion,” in *Proceedings of the International Workshop on Physics of Solar Energy*, 1986, vol. 1, pp. 27–38.
- [14] M. Archer, “The Past and Present,” in *Clean Electricity from Photovoltaics*, 1st Edition, Imperial College Press, 2001.
- [15] L. El Chaar, et al., “PV technology - Industry update,” *IEEE PES General Meeting PES 2010*, pp. 1–6, 2010.
- [16] B. Ismail, “Alternative Energy Engineering,” *Lakehead University*. p. 199–200, ENGI 5271 FA, 2016.
- [17] University of Central Florida, “Types of PV Systems,” *Florida Solar Energy Center*, 2014. [Online] Available: [http://www.fsec.ucf.edu/en/consumer/solar\\_electricity/basics/types\\_of\\_pv.htm](http://www.fsec.ucf.edu/en/consumer/solar_electricity/basics/types_of_pv.htm). [Accessed: 18-May-2018].
- [18] “What types of PV modules are available,” *Gehrlicher Solar*. [Online]. Available: <http://www.gehrlicher.com/en/service/faq/what-types-of-pv-modules-are-available/>. [Accessed: 04-Jun-2018].
- [19] “Photovoltaic Cell Working Principle – How to Convert Sunlight into Electricity,” *January 29, 2016*, 2016. [Online]. Available: <http://bestsale2u.com/photovoltaic-cell-working-principle-how-to-convert-sunlight-into-electricity/>. [Accessed: 12-Jun-2018].
- [20] N. M. Pearsall and R. Hill, “Photovoltaic Modules Systems and Applications,” in *Clean Electricity from Photovoltaics*, 1st Edition, vol. 1, M. D. Archer and R. Hill, Editors. Imperial College Press, 2001, p. 677.
- [21] S. R. Wenham, et al., “Semiconductors and P-N Junctions,” in *Applied Photovoltaics*, 2nd edition, Earthscan, 2007, p. 39.

- [22] A. J. Bühler, et al., “Post-processing data of measured I-V curves of photovoltaic devices,” *Renewable Energy*, vol. 68, pp. 602–610, 2014.
- [23] J. L. Gray, “The Physics of the Solar Cell,” in *Handbook of Photovoltaic Science and Engineering*, A. Luque and S. Hegedus, Ed. John Wiley & Sons Ltd, England, 2003.
- [24] L. Castañer and S. Silvestre, “Electrical Characteristics of the Solar Cell,” in *Modelling Photovoltaic Systems Using PSpice®*, John Wiley & Sons Ltd, England, 2002, p. 45.
- [25] J. Bisquert, “Basic Operation of Solar Cells,” in *The physics of solar cells: Perovskites, Organics, and Photovoltaic Fundamentals*, CRS Press, New York, 2018, p. 144.
- [26] G. A. Martin, “Accuracy of analytical expressions for solar cell fill factors.,” *Solar Cells*, vol. 7, pp. 337–340, 1982.
- [27] A. R. Jha, “Design Expressions and Critical Performance Parameters for Solar Cells,” in *Solar Cells Technology and Applications*, Auerbach Publications, 2010, pp. 64–66.
- [28] S. B. Riffat and E. Cuce, “A review on hybrid photovoltaic/thermal collectors and systems,” *International Journal of Low-Carbon Technology*, vol. 6, no. 3, pp. 212–241, 2011.
- [29] T. J. Tripanagnostopoulos, “Improved PV/T solar collectors with heat extraction by forced or natural air circulation,” *Renewable Energy*, vol. 32, pp. 623–637, 2007.
- [30] S. A. Kalogirou, “Hybrid PV/T systems,” in *Solar Energy Engineering Processes and Systems*, 2nd Edition, Academic Press, London, UK, 2014, p. 532.
- [31] M. A. Hasan and K. Sumathy, “Photovoltaic thermal module concepts and their performance analysis: A review,” *Renewable and Sustainable Energy Reviews*, vol. 14, no. 7, pp. 1845–1859, 2010.
- [32] P. G. Charalambous, et al., “Photovoltaic thermal (PV/T) collectors: A review,”

*Applied Thermal Engineering*, vol. 27, no. 2–3, pp. 275–286, 2007.

- [33] X. Ju et al., “A review of concentrated photovoltaic-thermal (CPVT) hybrid solar systems with waste heat recovery (WHR),” *Science Bulletin*, vol. 62, no. 20, pp. 1388–1426, 2017.
- [34] M. Y. H. Othman, et al., “Performance analysis of a double-pass photovoltaic/thermal (PV/T) solar collector with CPC and fins,” *Renewable Energy*, vol. 30, no. 13, pp. 5–17, 2005.
- [35] J. J. Michael and R. Goic, “Flat plate solar photovoltaic-thermal (PV/T) systems: A reference guide,” *Renewable and Sustainable Energy Reviews*, vol. 51, pp. 62–88, 2015.
- [36] Z. Xu and C. Kleinstreuer, “Computational Analysis of Nanofluid Cooling of High Concentration Photovoltaic Cells,” *Journal of Thermal Science and Engineering Applications*, vol. 6, no. 3, p. 31009, Mar. 2014.
- [37] “Optical Losses – PVEducation.” [Online]. Available: <https://www.pveducation.org/pvcdrom/optical-losses>. [Accessed: 25-Jun-2018].
- [38] PVEducation, “Anti-Reflection Coatings | PVEducation,” *Anti-Reflection Coatings*. [Online]. Available: <http://pveducation.org/pvcdrom/design/anti-reflection-coatings>. [Accessed: 25-Jun-2018].
- [39] M. Wolf, “Performance Analyses Of Combined Heating And Photovoltaic Power Systems For Residences,” *Energy Conversion*, no. IEEE Conference, pp. 79–90, 1976.
- [40] S. D. Hendrie, “Photovoltaic/thermal collector development program—final report,” 1982.
- [41] H. A. Zondag, “Flat-plate PV-Thermal collectors and systems: A review,” *Renewable and Sustainable Energy Reviews*, vol. 12, no. 4, pp. 891–959, 2008.
- [42] M. Malik, “Solar One,” in *Solar Energy Applications in Buildings*, A. Sayigh, Ed. Academic Press, New York, 1979.

- [43] J. C. Hollick, "Solar Cogeneration Panels," *Renewable Energy*, vol. 15, pp. 195–200, 1998.
- [44] X. Ju *et al.*, "A review of concentrated photovoltaic-thermal (CPVT) hybrid solar systems with waste heat recovery (WHR)," *Science Bulletin*, vol. 62, no. 20, pp. 1388–1426, 2017.
- [45] J. H. Kim and J. T. Kim, "Comparison of electrical and thermal performances of glazed and unglazed PVT collectors," *International Journal of Photoenergy*, vol. 2012, 2012.
- [46] M. Li, et al., "Performance investigation and optimization of the Trough Concentrating Photovoltaic/Thermal system," *Solar Energy*, vol. 85, no. 5, pp. 1028–1034, 2011.
- [47] L. T. Kostic, et al., "Influence of reflectance from flat aluminum concentrators on energy efficiency of PV/Thermal collector," *Applied Energy*, vol. 87, no. 2, pp. 410–416, 2010.
- [48] M. Chaabane, et al., "Performance evaluation of concentrating solar photovoltaic and photovoltaic/thermal systems," *Solar Energy*, vol. 98, no. PC, pp. 315–321, 2013.
- [49] A. M. Manokar, et al., "Performance Analysis of Parabolic trough Concentrating Photovoltaic Thermal System," *Procedia Technology*, vol. 24, pp. 485–491, 2016.
- [50] F. Calise, et al., "A finite-volume model of a parabolic trough photovoltaic/thermal collector: Energetic and exergetic analyses," *Energy*, vol. 46, no. 1, pp. 283–294, 2012.
- [51] C. Renno and F. Petito, "Choice model for a modular configuration of a point-focus CPV/T system," *Energy and Buildings*, vol. 92, pp. 55–66, 2015.
- [52] C. Renno and M. De Giacomo, "Dynamic Simulation of a CPV/T System Using the Finite Element Method," *Energies*, vol. 7, no. 11, pp. 7395–7414, 2014.
- [53] B. Sandnes and J. Rekstad, "A photovoltaic/thermal (PV/T) collector with a

- polymer absorber plate. Experimental study and analytical model,” *Solar Energy*, vol. 72, no. 1, pp. 63–73, 2002.
- [54] T. Fujisawa and T. Tani, “Annual exergy evaluation on photovoltaic thermal hybrid collector,” *Solar Energy Materials and Solar Cells*, vol. 47, pp. 135–148, 1997.
- [55] T. Yamada, et al., “Reflection loss analysis by optical modeling of PV module,” *Solar Energy Materials and Solar Cells*, vol. 67, pp. 405–413, 2001.
- [56] N. Martín and J. M. Ruiz, “Calculation of the PV modules angular losses under field conditions by means of an analytical model,” *Solar Energy Materials and Solar Cells*, vol. 70, no. 1, pp. 25–38, 2001.
- [57] N. Martín and J. M. Ruiz, “Annual angular reflection losses in PV modules,” *Progress in Photovoltaics: Research and Applications*, vol. 13, no. 1, pp. 75–84, 2005.
- [58] B. H. Hamadani and B. Dougherty, “Solar cell characterization,” *Semiconductor Materials for Solar Photovoltaic Cells*, pp. 229–245, 2015.

## APPENDIX A-1:

### SPECIFICATIONS OF THE FLEXIBLE PV PANEL

#### Feature:

- 25W 18V Sunpower Semi-flexible Solar Panel
- Light weight, easy to carry.
- High conversion rate, high output.
- Resistance to resistance, can resist different environment, waterproof performance is good.
- High stability, good durability
- With Sunpower chip, can be used for car ,home, boat, motorcycle, etc.
- Suitable for car batteries, car, RV, boat, ship, aircraft, satellites, space stations, outdoor breeding, planting, tourism, solar street lamp.
- Resistance to resistance, can resist different environment, waterproof performance is good.
- Components can withstand snow pressure up to 5400Pa, to withstand wind pressure up to 2400Pa.
- Semi-flexible, and can be properly bent to use a wider range of applications.

#### Specifications:

Product name: Solar panels  
Color: Black  
Size: Approx. 560x280x2mm/22"x11"x0.078"  
Power: 25W  
Working voltage: 18V  
IPmax: 1.39A  
Isc: 1.59A  
Voc: 21V  
Operating Temperature: -40°C-85 °C  
Weight: 751g

#### Package Include:

1x Elfeland 25W 18V Sunpower Semi-flexible Solar Panel



Figure A-1: Specifications of the flexible PV panel used in this research.

## APPENDIX A-2:

### SPECIFICATIONS OF THE REGEN-PV PANEL

**Parameters:**

Model Number: GP80\*80-10A100

Material: Monocrystalline Silicon

Number of Cells: 10

Max. power: 0.5W

Max. current: 100mA

Max. voltage: 5V

Size: 80mm\*80mm/3.15in\*3.15in

Weight: 50g/1.76oz

**Features:**

1. 4 holes at for extreme corner for holding screw, at 2mm diameter.

2. Red/black 3 feet long wire, connected as one wire. 3. Colored alligator clips soldered in the backside

4. Blocking diode installed already in the back to protect the solar panel from over-charging and current backflow.

5. Put a plastic cover in the panel, a label stick there said "please remove protective cover"

6. Special silicone to protect the blocking diode well to prevent the humid climates.

**Package Content:**

1\* Solar Panel (alligator clips soldered in the backside)

Figure A-2: Specifications of regen-PV module used in this research.



## APPENDIX A-3

# SPECIFICATIONS OF BLACK COPPER ABSORBER



湖南国开国际发展有限公司  
GK INTERNATIONAL ENTERPRISES CO.,LTD.

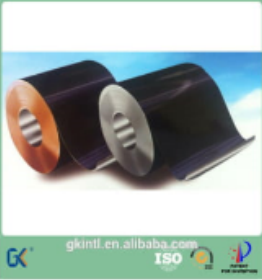
Product name	black chrome copper selective solar coating
Picture	
Width	140mm
Length	customized
Thickness	0.12mm
Hardness	Halfhard
Specific weight(g/cm <sup>3</sup> )	8.95
Certification	ISO9001:2008;Patent for invention
Substrate Material	Copper
Light Performance Indicator	Absorptivity:95±2%
	Emissivity:8±2%
Corrosion Resistance	Salt-fog test≥72h
Anti-fatigability And Heat&Humidity	Heat and moisture test≥72h
Cohesive Force	Conforming to GB5270-85
Temperature stability	Vacuum ≈ 400℃
	Air ≈ 350℃
Coils or sheet with	Paper interleave

Figure A-3: Specifications of the black Cu absorber used in this research.

## **APPENDIX B:**

### **7<sup>TH</sup> – INTERNATIONAL CONFERENCE & EXHIBITION ON CLEAN ENERGY (ICCE-2018), QUEBEC, CANADA**

ICCE-2018 is an international conference focused on clean and renewable energy and was held from August 6<sup>th</sup> to 8<sup>th</sup>, 2018 at Laval University, Quebec City. This research work was presented at the conference and the conference committee has approved our referred paper and was published by International Academy of Energy, Minerals & Materials, Ottawa, Ontario. The published conference paper is presented in this appendix.



# EXPERIMENTAL CHARACTERIZATION OF A HYBRID PHOTOVOLTAIC-THERMAL SYSTEM WITH REGENERATION

B.I. Ismail\* and A. Jose

*Department of Mechanical Engineering, Lakehead University  
955 Oliver Road, Thunder Bay, Ontario P7B5E1, Canada  
(\*Corresponding author: bismail@lakeheadu.ca)*

## ABSTRACT

Currently, enormous quantities of waste energy are continuously discharged into the earth's atmosphere from various sources. For example, in a photovoltaic panel, about 85% of the incident light is either dissipated as heat or reflected from the PV surface accounting huge losses. Reflection losses in a PV panel can be up to 20% even with antireflection layers inbuilt in them. In order to regenerate some of the optical losses in a photovoltaic system, a new hybrid photovoltaic-thermal regeneration system (HPVT-Regen) is designed and built. The new HPVT-Regen system design allows the photovoltaic and thermal subsystems to function independently while regenerating some of the optical losses by hybridization. Detailed experimentation of the HPVT-Regen system was conducted under indoor lab-scale solar simulator as well as under outdoor solar radiation conditions of Thunder Bay, Ontario. The results showed that the HPVT-Regen system regenerated 14 % of the light, which was reflected from the PV panel, and converted into electrical as well as heat energy. This paper presents and discusses the design and real-time performance characteristics of the HPVT-Regen system under various operating conditions.

**KEYWORDS:** Clean renewable energy, Hybrid power generation, Waste heat recovery, Curved PV surface, Solar PV simulations, Thunder Bay's climate conditions

## 1 INTRODUCTION

In recent years, increasing concern of environmental issues of greenhouse gas (GHG) emissions, causing global warming and climate change, and the limitations of energy resources have resulted in extensive research into novel technologies of generating electrical power. The International Energy Outlook (IEO) 2010 reported and projected an increase of 43% in carbon dioxide emissions from 2007 to 2035. The estimated emission would increase from 29.7 billion metric tons in 2007 to 33.8 billion metric tons in 2020 and 42.4 billion metric tons in 2035. The world marketed energy consumption was also estimated to increase by 49% from 2007 to 2035. IEO2010 predicted that the world renewable energy use for electricity generation would grow by an average of 3.0% per year reaching 4.5 trillion kWh from 2007 to 2035 (U.S. Energy Information Administration, IEO-2010). Canada is the fifth largest energy producer and eighth largest energy consumer. Renewable energy represents 17% of Canada's total primary energy supply. Hydroelectricity is the most abundant renewable energy supply with 60% of Canada's electricity generation. Resources such as biomass, wind, tidal, and solar contribute 3% of electricity generation (Natural Resources Canada).

Currently, enormous quantities of waste-heat energy are continuously discharged into the Earth's atmosphere from various sources. For example, in a gasoline spark-ignition (SI) powered engine, approximately 30-40% of the primary gasoline fuel energy is dissipated as waste heat energy in the exhaust gases; waste heat energy discharged in the exhaust gases from a typical passenger car travelling at a regular speed is 20-30 kW (Ismail and Ahmed, 2009; Ismail, 2012, Ismail and Bujold 2014). The utilization and

direct conversion of this waste-heat energy into green electrical power were accomplished by Ismail and Hazrat (2016) using innovative Stirling engine (SE). A unique experimental test setup was made incorporating a prototype gamma-configuration SE system to investigate the SE ability in converting the exhaust waste heat produced from an actual four-stroke SI engine into electrical power.

A Hybrid PV-T collector is a combination of photovoltaic (PV) and thermal (T) components that enable to produce both electricity as well as heat simultaneously. HPVT systems produce more energy per unit surface area than side-by-side PV modules and thermal collectors working independently (Riffat and Cuce, 2011). Although PV modules convert sunlight directly into electricity, most of the absorbed solar radiation is unused and dissipated to the PV modules as waste heat. Solar radiation that cannot be converted into electricity raises the temperature of the PV modules, causing a decrease in their electrical efficiency. The heat generated can be transferred to a heat exchanger in thermal contact with PV modules to meet some heating demand (Tripanagnostopoulos et al., 2007). There are various designs developed to improve the overall efficiency of HPVT systems. For example, Ismail and Bujold (2015) experimentally investigated the performance characteristics of a Hybrid PV solar and Thermoelectric (HPV-TEG) system for direct power generation from solar and waste heat energy. They reported an increase in both power generation and overall efficiency of the system. In their design, they used a flat PV panel.

Among various losses in a PV panel, one of the significant loss is reflection loss. Up to 20% of the incident light is reflected even after employing antireflection layers (Yamada, T. et al., 2001). There are studies of numerical quantification of this reflected light but lacks effective methods and experimentation in utilizing them. HPVT systems are an excellent application for buildings which require simultaneous electric power and heat. Usually, an HPVT system constitutes photovoltaic and thermal subsystems working together to maximize the utilization of incident solar radiation. A silicon-based PV panel has some restriction in responding to the solar spectrum, converting the light in the range of visible light and near IR into electricity with an electrical efficiency up to 20% and dissipating high-intensity IR radiations into heat. The dissipated heat negatively affects the performance of the PV cells that for every single degree rise in temperature, the efficiency decreased by approximately 1% as reported by (Kalogirou S. A., 2014). Thus, to cool the PV panel as well as to regenerate the wasted heat, a thermal collector can be hybridized with PV panel.

Integrating flat plate PV and thermal collector reduces the production and installation cost and is quite suitable for building rooftop and façade. Since solar cells are not an efficient thermal absorber, flat plate PV-T systems generate low-temperature heat that is considered just as a byproduct of cooling the solar cells (X. Ju *et al.*, 2017). Jin Kim and Jun Kim (2012) studied the experimental performance of glazed (glass covered) and unglazed liquid type PV-T collectors in outdoor conditions. Their results showed that the thermal efficiency of the glazed PVT collector is 14% higher than that of the unglazed PVT collector, but the unglazed collector had approximately 1.4% higher electrical efficiency than the glazed collector. The overall performance of the glazed collector was approximately 12.6% higher than that of the unglazed collector. Li, M. et al. (2011) analyzed a 10 m<sup>2</sup> Trough Concentrating PVT (TCPVT) system with a parabolic trough concentrator, receiver, electrical energy output system, and a thermal energy storage system. Supercell array, GaAs cell array, and Si cell array were pasted on the lighting plate of the receiver with thermally conductive tape. In their work, forced water was circulated through the inner cavity of the receiver which cools the solar cells while generating heat. Their experimental results showed average electrical efficiencies of approximately 3.6%, 8.9%, and 3.7%, respectively for each cell types. When the mirror reflectivity is improved from 0.69 to 0.92, the electrical efficiency increased by 0.9%, 2.62%, and 5.47%, respectively for each cell types. Since 85% of the incoming solar radiation is either reflected or absorbed as heat by the traditional PV system, A. M. Manokar et al. (2016) worked on the performance analysis of a Parabolic Trough Concentrating Photovoltaic-Thermal System. They employed a parabolic trough as light concentrator and channel PV/T collector as the receiver. To capture maximum reflection from the trough, they have designed a “V” shaped receiver. The concentrator increased the temperature on the PV system by 20°C which was then transferred to cooling water. They also report an adverse impact on the electrical performance due to a significant rise in PV temperature. Yamada et al. (2001) analyzed the influence of reflection on a PV module using the optical properties of the module materials. Using the

optical performance of a four-layer encapsulation, a simulation was made on the reflection loss from a PV module according to Fresnel's law. They reported that only less than 80% of the light is transmitted to the silicon cell within an incident angle of 50 degrees. The transmittance is steeply declining when the incident angle varies from 50 to 90 degrees.

This research paper describes a new design for an HPVT which permits photovoltaic and thermal systems to function independently while regenerating some of the optical losses in the photovoltaic system by hybridization. This research was accomplished by performing detailed experimentation of the new design using indoor solar simulations and outdoor solar radiation to study the performance of the photovoltaic subsystem, the thermal subsystem, and the regeneration of photovoltaic optical losses. This research uses a lab scale design of HPVT with a flexible curved PV panel of 25W, four 0.5 W PV modules for regeneration of reflected light, and an air type thermal collector. The major advantage of the proposed design is that the design permits PV panel and thermal collector to function independently while regenerating some of the reflected light by hybridization.

## 2 THE DESIGN AND ENERGY BALANCE OF THE HPVT-REGEN SYSTEM

In this research, an HPVT system was designed, fabricated, and fully instrumented in order to test the regeneration of electrical as well as thermal power. To assist in building the HPVT-Regen prototype, a 3D model of the system was produced using Catia V5 (CAD) software as shown in Figure 1. A flexible PV panel of 25W, 18 V is fixed in a curved position in a wooden frame. The characteristics of the PV panel in horizontal and curved positions were identical in the indoor testing. The thermal collector fixed at the focal line is made of a steel channel to allow air flow. The steel channel is wrapped tightly with a black copper sheet of high absorptivity of 0.95 with the help of thermally conductive adhesives. There are four low rating PV modules connected in parallel arranged at the bottom surface of the thermal collector facing the curved PV panel.

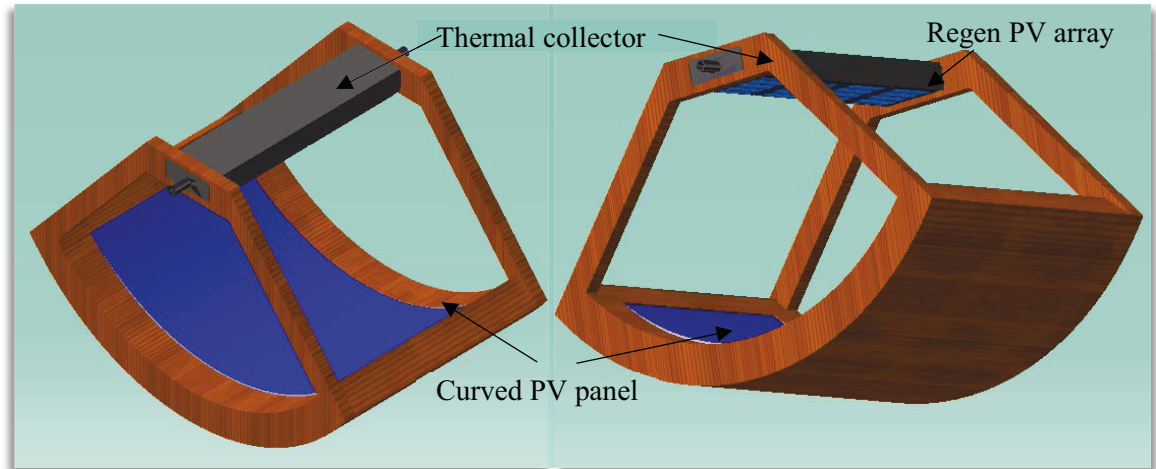


Figure 1: The 3D model of the HPVT-Regen used in this research in order to regenerate power from reflection loss of the curved PV panel.

The energy flow diagram of the proposed HPVT-Regen system shown in Figure 2 illustrates the conversion of energy from the sun into electricity and heat through photovoltaic and thermal subsystems respectively. The radiation from the sun impinges on the curved PV panel as well as on the thermal collector in the focal line. The curved PV panel converts a portion of the solar radiation into electricity. The unabsorbed transmitted radiation is dissipated into heat, and some of the light incident on the PV panel is reflected (estimated at up to 20%) from the PV surface. Simultaneously, thermal collector also receives the solar radiation. The black absorber on the thermal subsystem has an absorptivity of 0.95 which absorbs the

solar radiation and delivers the heat to the working fluid, air, flowing at a specific flow rate. The heated air can be then supplied for space heating or to reduce the load on an existing HVAC system. The light reflected from the curved PV panel is then focused on the regen PV modules arranged on the bottom surface of the thermal collector. The Regen-PV modules convert the reflected light into electricity of lower power. These Regen-PV modules also dissipate the unabsorbed light into heat and then exchanged to the flowing air. This low power electricity and heat produced from the reflected light are considered the regenerated power from the HPVT-Regen system.

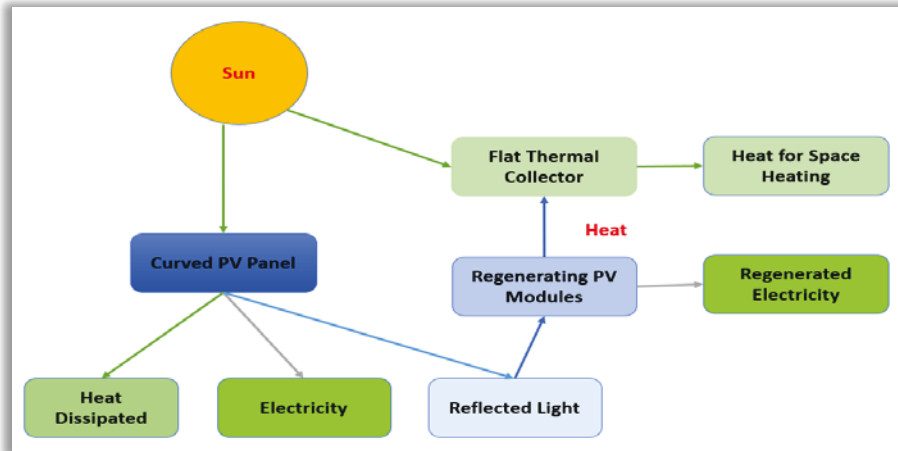


Figure 2: The energy flow diagram of the HPVT-Regen system used in this research work.

### 3 EXPERIMENTAL TEST SETUP OF THE HPVT-REGEN SYSTEM

The experimental test set up was designed and constructed in order to study in detail the performance characteristics of the curved PV panel, thermal collector, and Regen-PV array. This requires careful and real-time measurements of irradiation, voltage, current, temperature, air flow rate, and emittance as shown in Figure 3.

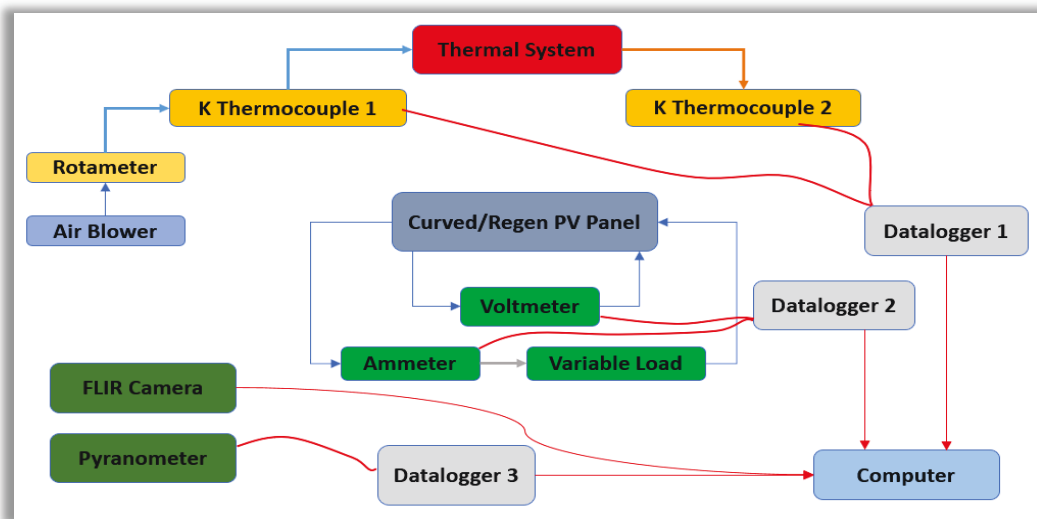


Figure 3: The real-time fully instrumented experimental test setup of the HPVT-Regen system used in this research.

As shown in Figure 3, the HPVT-Regen test setup was fully instrumented with real-time data acquisition sensors for temperature measurements at various locations across the thermal collector. In addition, the system is equipped with voltage and electric current measurement sensors for the DC power output from the curved and regen PVs, irradiance, and emittance sensors to measure input global solar radiation impinging on the photovoltaic and thermal subsystems, respectively. A photograph showing the experimental test setup of the HPVT-Regen used in this research is shown in Figure 4.

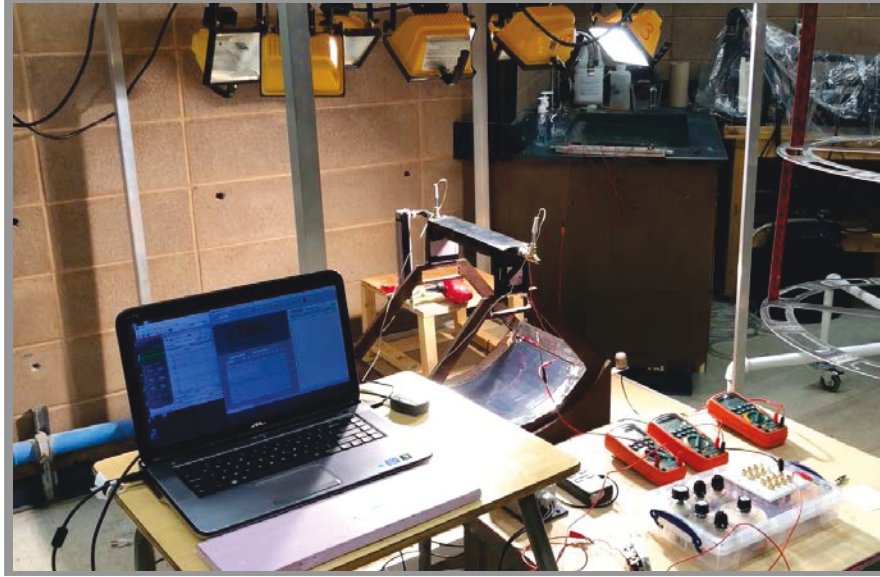


Figure 4: A photograph showing the experimental test setup of the HPVT-Regen system used in this research.

The curved PV panel and regen PV array were tested under indoor solar simulator and outdoor solar radiation of Thunder Bay city, using a 4-wire Kelvin circuit consisting of a voltmeter, ammeter, and variable load. Since the indoor simulated radiation is almost constant throughout, a variable load is used to characterize the PVs. The real-time characterization under the outdoor solar radiation was performed using Solmetric PVA-600V PV Analyser. A pyranometer was used to measure the input solar radiation impinging on the HPVT-Regen system. The maximum power output from the photovoltaic subsystem is calculated using,

$$P_{max} = V_{mp}I_{mp} \quad (1)$$

Where,  $V_{mp}$ , and  $I_{mp}$  are the output DC voltage and current, respectively, at the maximum power point. The electrical conversion efficiency of the PV subsystem is given by,

$$\eta_{pv} = \frac{P_{max}}{P_{in,pv}} \quad (2)$$

Where,  $P_{in,pv}$  is the incident solar radiation measured by the pyranometer.

Forced air circulation in the thermal collector was provided using an air-blower. The air flow rate is measured and regulated by OMEGA-FL-3840ST rotameter. The inlet and outlet air temperature are measured by K-type thermocouples. The temperature measurements are acquired every 20 minutes at an



interval of one minute. The thermal collector was calibrated in order to eliminate the effect of heat added by the air blower as well as heating of thermocouples by irradiation. A calibrated FLIR-IR camera is used to measure incident thermal radiation received by the thermal collector. The thermal power output from the solar collector is given by,

$$P_{th} = \dot{m} C_{p,air}[T_{out} - T_{in}] \quad (3)$$

Where,  $\dot{m}$  is the air mass flow rate measured by the rotameter,  $C_{p,air}$  is the specific heat of air,  $T_{out}$  and  $T_{in}$  are the outlet and inlet air temperatures, respectively. The collector receives thermal radiation from the top surface by direct irradiation and from the bottom surface by reflected radiation from the curved PV panel. Total thermal radiation received by the top and bottom surfaces are given by,

$$P_{in,th} = \sigma A[\varepsilon_1(T_{SA})^4 + \varepsilon_2(T_{SB})^4] \quad (4)$$

Where,  $\sigma$  is the Boltzmann constant,  $A$  is the area of the radiated surface,  $\varepsilon_1$  and  $\varepsilon_2$  are the emissivity of top black Cu absorber and bottom Regen PV silicon respectively,  $T_{SA}$  and  $T_{SB}$  are the temperature (in K) of the top and bottom surfaces, respectively, after being calibrated.

#### 4 EXPERIMENTAL RESULTS AND DISCUSSION

As mentioned previously, detailed experimental tests and measurements were performed in order to fully characterize the performance of the HPVT-Regen system. Figure 5 shows the I-V characteristics of the curved PV panel tested under indoor simulator. The curved PV panel produced an electric power of 2.6 W with an electrical efficiency of approximately 13% under irradiation of 173.04 W/m<sup>2</sup> from the solar simulator.

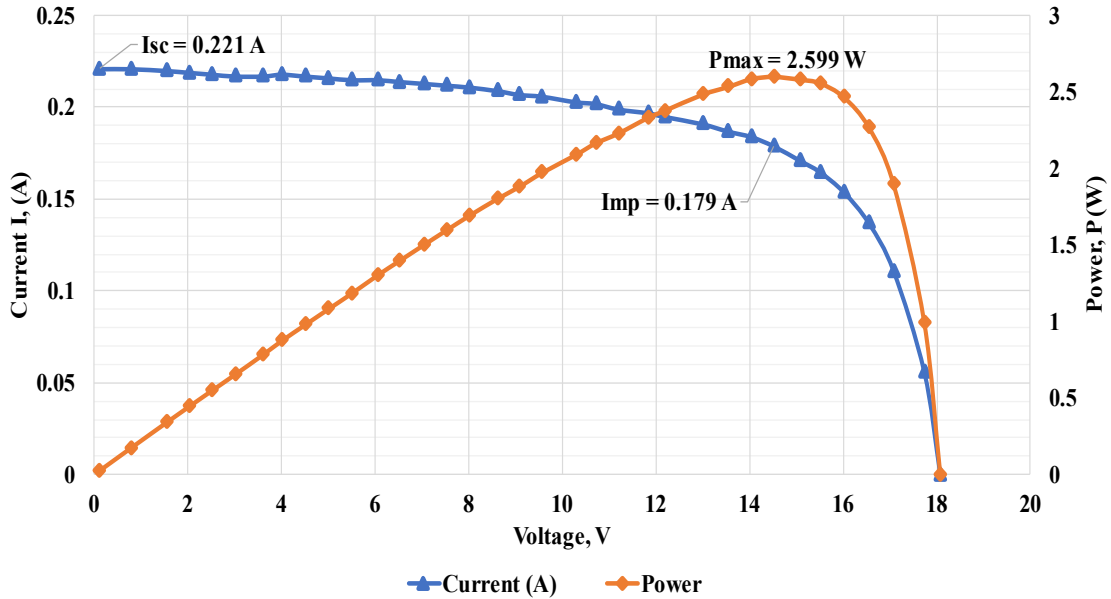


Figure 5: I-V characteristics of the curved PV panel subsystem under indoor solar simulations.

From the pyranometer measurements, approximately 14.73% of the incident simulator light was received as reflected light on to the Regen-PV array. The Regen-PV array regenerated 17.047 mW of electric power from this reflected light with an electrical efficiency of 4.28% contributing with less than

1% more electric power per unit area. Figure 6 shows the I-V characteristics of the Regen-PV array performing under the reflected radiation. It was found that the test was relatively unstable as the Regen-PVs were performing under variably reduced illumination. The electrical load was carefully varied to take into account the variations in DC voltage (V) and current (mA).

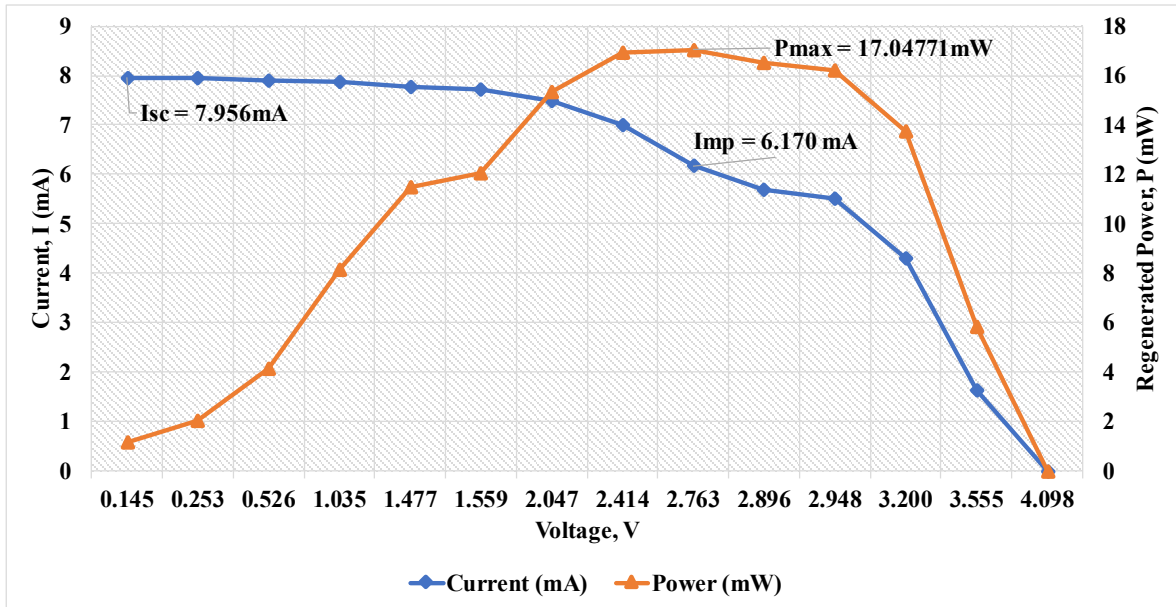


Figure 6: I-V characteristics of the Regen-PV array under indoor solar simulations.

The results show that the curved PV panel produced more electrical power, nearly doubled, under outdoor solar radiation compared to indoor simulations. However, the electrical efficiency of the curved PV panel dropped drastically as the available capacity of the PV panel was much lower to absorb the high-intensity of solar radiation. For this case, the PV panel produced an electric power of 4.35 W with an electrical efficiency of 3.63%. The outdoor performance characteristics of the curved PV panel were obtained and the variation in maximum power with respect to solar radiation is shown in Figure 7. The decrease in the irradiation and power in Figure 7 was found due to the intermittent sky clouds during the day of testing. The outdoor performance of the Regen-PV array was found to be very promising. The results, in outdoor testing, showed that the reflected light from the curved PV panel measured by the pyranometer is 14.31% of the incident radiation, which is similar to 14.73% obtained in the indoor testing. This was found to be in agreement with results of optical properties of the PV panel analyzed by Yamada et al., 2001.

Figure 8 shows the I-V characteristics of the Regen-PV array performing under the reflected radiation. The Regen-PV array produced an electric power of 0.137 W under solar radiation with an electrical efficiency of 6.90% contributing to approximately 3.167% more electric power per unit PV surface area. The characterization test of the Regen-PVs under solar radiation was relatively more stable than the indoor testing. Table 1 gives a comparison of the critical performance parameters and values of the electrical subsystem of the HPVT for indoor and outdoor testing.

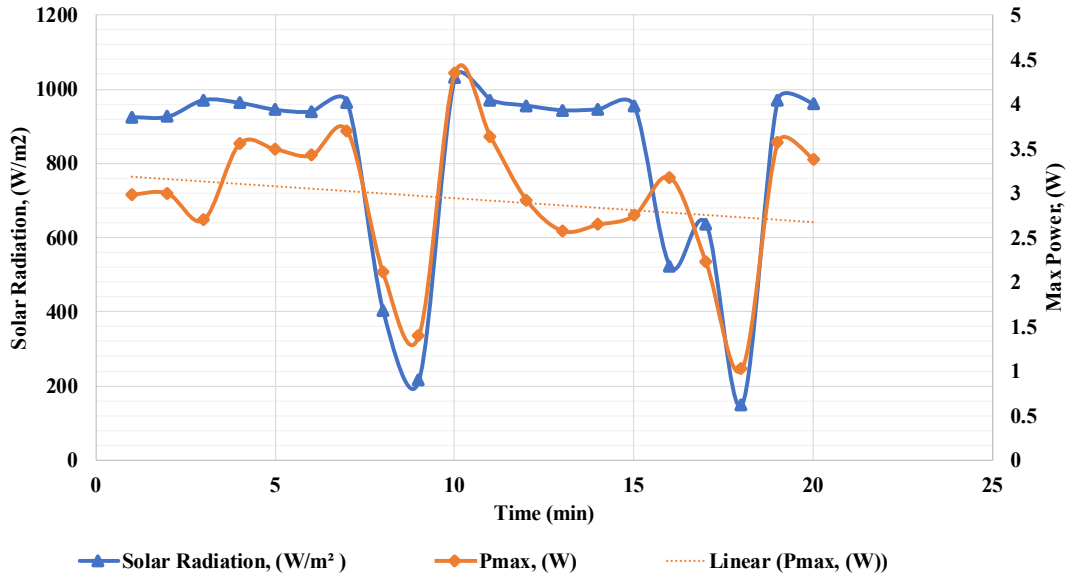


Figure 7: Variation in maximum power of the curved PV panel with respect to solar radiation for a duration of 20 minutes.

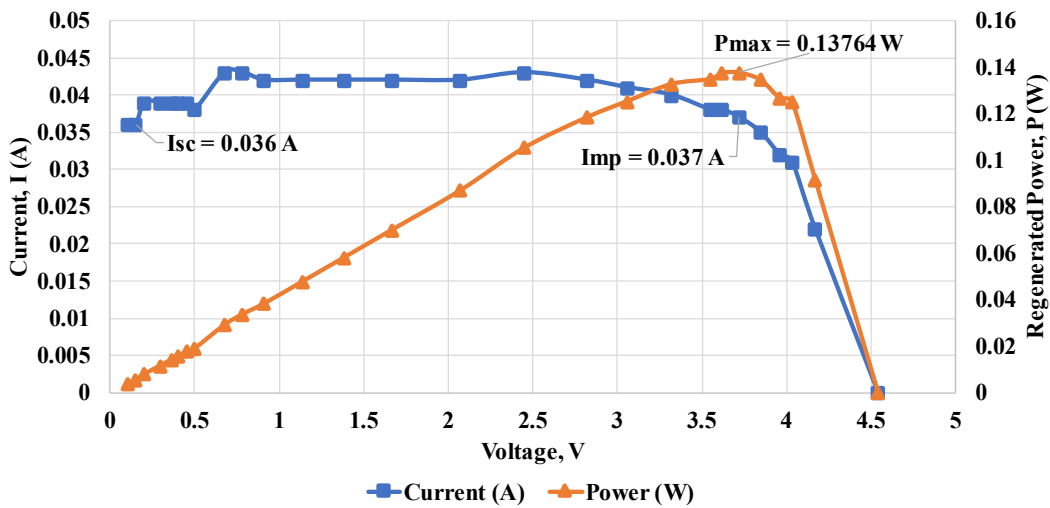


Figure 8: I-V characteristics of the regen PV array obtained while testing under outdoor solar radiation.

The performance of the thermal collector was analyzed for an air volumetric flow rate of  $0.000295 \text{ m}^3/\text{s}$  under simulator lights and solar radiation. The gain in temperature by the air cannot be measured directly since there are unaccounted heating from air blower and thermocouple heating due to exposure to radiation. Thus, the actual rise in air temperature was determined by calibrating the temperature data. For calibration, the heat addition by the air blower and thermocouple heating were separately measured on different days and subtracted from the temperature data of the actual running of the thermal subsystem. The experiment also included separate measurement of temperature rise due to reflected light by insulating the top surface for both indoor and outdoor testing. Figure 9 shows temperature gain by the circulated air for a test duration of 20 minutes under indoor simulations, whereas, Figure 9(a) shows the total temperature gain, and Figure 9(b) shows temperature gain solely due to reflected light.

Table 1: Comparison of performance parameters of the electrical subsystem of the HPVT-Regen system for indoor and outdoor testing.

Parameters	Indoor testing	Outdoor testing
Irradiation, $P_{in,pv}$	173.039 W/m <sup>2</sup>	892.54 W/m <sup>2</sup>
Reflected solar radiation, $P_{in,regn}$	25.5 W/m <sup>2</sup>	127.75 W/m <sup>2</sup>
Percentage reflection	14.73 %	14.31 %
Max power-curved PV, $P_{max,pv}$	2.599 W	4.345 W
Electrical efficiency- curved PV	12.95%	3.63 %
Max power-Regen PV, $P_{max,regen}$	17.04 mW	137.64 mW
Electrical efficiency- Regen PV	4.28 %	6.90 %
Regeneration of electric power	< 1%	3.16 %

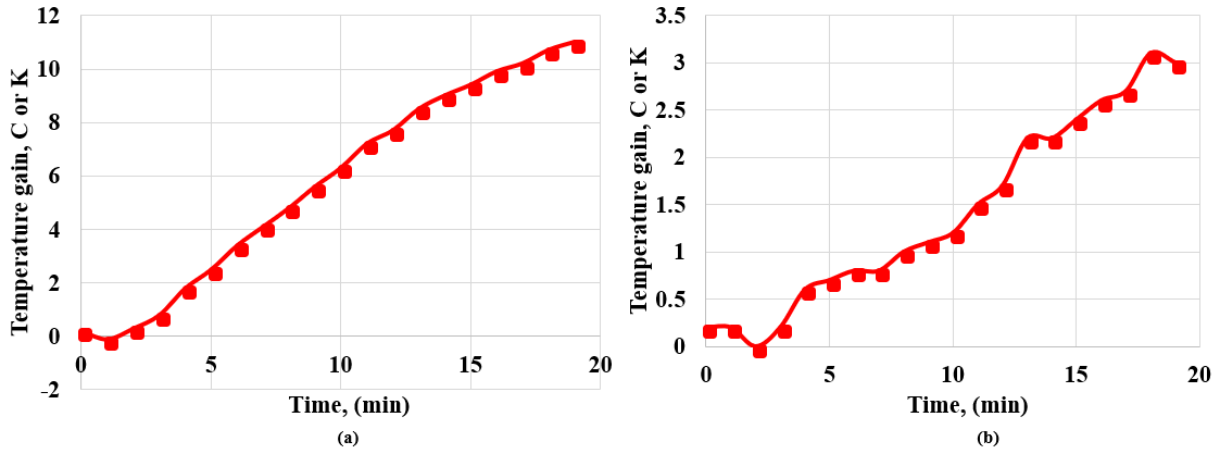


Figure 9: Temperature gain by the air in thermal collector when tested for 20 minutes under indoor simulator, (a) total gain in temperature, (b) temperature gain solely due to reflected light.

In Figure 9, the results show that, under indoor simulations, air flowing at a rate of 0.000295 m<sup>3</sup>/s through the thermal collector gained a total temperature rise of 11°C of which 3°C rise was solely due to the reflected light. The thermal collector obtained a thermal conversion efficiency of approximately 41% for indoor testing. The input thermal radiation was calculated using Equations 3 and 4 with the aid of thermal images taken by FLIR-IR camera calibrated for the top and bottom surfaces of the thermal collector respectively as shown in Figure 10. Figure 11 shows temperature gain by the air flowing at a flow rate of 0.000295 m<sup>3</sup>/s through the thermal collector for a test duration of 20 minutes under outdoor solar radiation. Figure 11(a) shows the total temperature gain, and Figure 11(b) shows temperature gain solely due to reflected light. The results also show that, under outdoor solar radiation, the thermal collector gained a total temperature rise of 9.3 °C of which 2.4 °C rise is solely due to reflected light. The thermal collector obtained a thermal conversion efficiency of approximately 50%, based on the outdoor testing. The comparison of the considered thermal parameters for indoor and outdoor tests are given in Table 2.

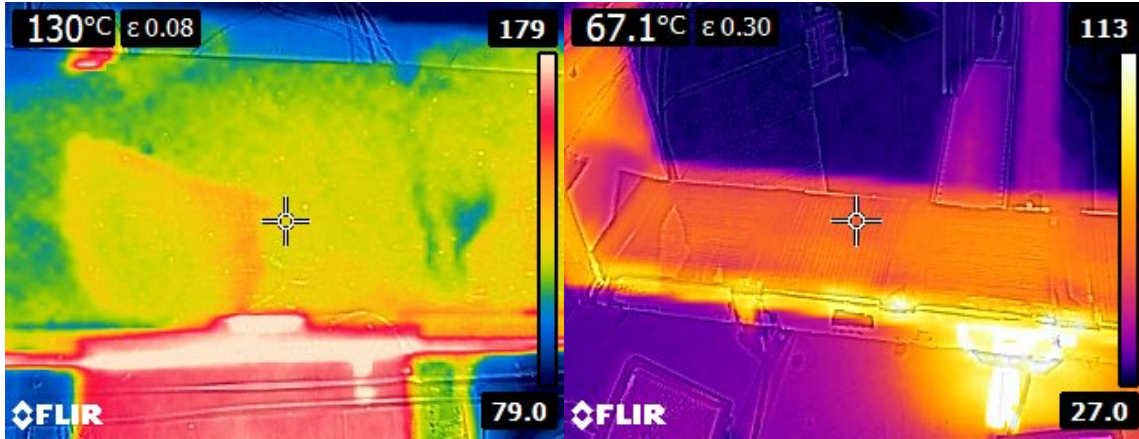


Figure 10: Thermal images of the top (left) and bottom (right) surfaces of the thermal collector taken with FLIR camera for indoor simulation.

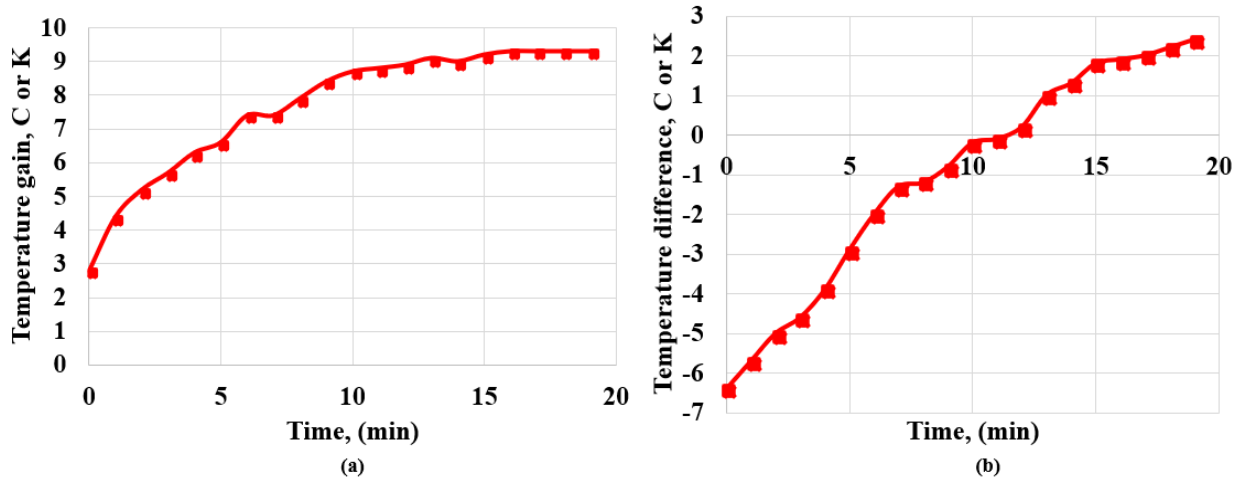


Figure 11: Temperature gain by the air in thermal collector when tested for 20 minutes under outdoor solar radiation, (a) total gain in temperature, (b) temperature gain solely due to reflected

Table 2: Comparison of performance parameters of the thermal subsystem of the HPVT-Regen system for indoor and outdoor testing.

Parameters	Indoor testing	Outdoor testing
Total air temperature gain	11 °C	9.3 °C
Temperature gain due to reflected light	3 °C	2.4 °C
Thermal Power	3.924 W	3.379 W
Thermal efficiency	40.58 %	50.23 %

## 5 CONCLUSIONS

In this work, an experimental test setup of the hybrid photovoltaic-thermal system with regeneration (HPVT-Regen) was designed, built and fully instrumented to experimentally investigate the regeneration of optical losses from the photovoltaic subsystem. Detailed real-time tests were performed using the HPVT-Regen system under indoor solar simulations as well as under outdoor solar radiation of Thunder Bay

climate conditions in order to characterize the electrical and thermal performance of the HPVT-Regen system. The experimental results showed that the Regen-PV subsystem reflected approximately 14% of the incident radiation of the indoor as well as of the outdoor tests. The HPVT-Regen system regenerated this reflected light and converted into electrical and heat power. The indoor setting regenerated 17.04 mW of electricity with an electrical conversion efficiency of approximately 4.3% and contributed with less than 1% more electric power per unit area. However, the outdoor setting regenerated 137.64 mW of electricity with an electrical efficiency of 6.9% and contributed 3.16 % more electric power per unit area. The thermal collector regenerated 3°C and 2.4 °C of air temperature solely from the reflected radiation in the two indoor and outdoor settings, respectively. The indoor simulations achieved a total output power density of 156.72 W/m<sup>2</sup> with an overall conversion efficiency of approximately 91%, whereas the outdoor experimentation achieved a total output power density of 158.90 W/m<sup>2</sup> with an overall efficiency of 17.80%. Although, the power density obtained was higher in the outdoor testing, the HPVT-Regen system did not perform well under real solar radiation outdoor conditions. The reason is attributed to the lower power rating of the curved PV panel. Using a high rated PV panel of the same size would bring up the overall efficiency of the HPVT-Regen system making it applicable in practical situations. Therefore, it is suggested that more detailed outdoor testing is required in the future for further understanding this interesting performance phenomena.

## 6 ACKNOWLEDGMENTS

The primary author wishes to acknowledge the funding contributions provided partly by Science Without Border (SWB) engineering research placement projects funds under the primary author's supervision at Lakehead University (2013 & 2014), as well as remaining small fund from Dr. Ismail's previous Goldcorp research (2007-2010). Acknowledgments also go to Mr. Jawad Hazrat, Mr. Joe Ripku, and Ms. Pragati Gupta, for their help in this research work at Lakehead University.

## REFERENCES

- Ismail, B. I., Ahmed, W. (2009). Thermoelectric Power Generation using Waste-Heat Energy as an Alternative Green Technology. *Recent Patents on Electrical Engineering*, 2(1), 27-39.
- Ismail, B. I. (2012). Automotive Exhaust Gas Waste-Heat Recovery for Green Electrical Power Generation Using Thermoelectric Technology. *Recent Patents on Electrical & Electronic Engineering*, 5(3), 185-197.
- Ismail, B. I., Bujold, J. P. (2014). Experimental Investigation of Direct and Clean Power Generation from Exhaust Waste Heat Energy Produced from SI Engine Using Thermoelectric Green Technology, *3<sup>rd</sup> International Conference & Exhibition on Clean Energy (ICCE2014), October 20-22, 2014, Quebec City, Canada.*
- Ismail, B. I., Bujold, J. P. (2015). Performance Characteristics of a Simulated Hybrid Solar-Photovoltaic-Thermoelectric System for Renewable and Direct Power Generation Applications. *Journal of Solar Energy Research Updates*, 2(2), 31-39.
- Ismail, B. I., Hazrat, A. J. (2016). Experimental Characteristics of Green Power Generation Using a Stirling Engine Powered by Waste Heat Energy in Exhaust Gases Produced from a Four-Stroke SI Engine. *5<sup>th</sup> International Conference & Exhibition on Clean Energy (ICCE2016), August 22-24, 2016, Montreal, Quebec, Canada.*
- Ju, X. *et al.* (2017). A Review of Concentrated Photovoltaic-Thermal (CPVT) Hybrid Solar Systems with Waste Heat Recovery (WHR). *Science Bulletin*, vol. 62, no. 20, 1388–1426.
- Kalogirou, S. A., Hybrid PV/T Systems, *Solar Energy Engineering Processes and Systems, 2nd Edition, Academic Press, London, UK, 532.*
- Kim, J. H., and Kim, J. T. (2012). Comparison of Electrical and Thermal Performances of Glazed and Unglazed PVT Collectors, *International Journal in Photoenergy*, vol. 2012.
- Li, M. *et al.* (2011). Performance Investigation and Optimization of the Trough Concentrating Photovoltaic/Thermal system, *Solar Energy*, vol. 85, no. 5, 1028–1034.

- Manokar, A. M. (2016). Performance Analysis of Parabolic Trough Concentrating Photovoltaic-Thermal System, *Procedia Technology*, vol. 24, 485–491.
- Michael, J. J. *et al.* (2015). Flat Plate Solar Photovoltaic-Thermal (PV/T) Systems: A reference guide. *Renewable Sustainable Energy Review*, vol. 51, 62–88.
- Natural Resources Canada (2013), “Canada – A Global Leader in Renewable Energy: Enhancing Collaboration on Renewable Energy Technologies,” *Energy and Mines Ministers Conference*, 1- 12.
- Riffat, S. B., and Cuce, E. (2011). A Review on Hybrid Photovoltaic/Thermal Collectors and Systems, *International Journal on Low-Carbon Technology*, vol. 6, 212–241.
- Tripanagnostopoulos, T. J. *et al.* (2007). Improved PV/T Solar Collectors with Heat Extraction by Forced or Natural Air Circulation, *Renewable Energy*, vol. 32, 623–637, 2007.
- U.S. Energy Information Administration (2010). *International Energy Outlook*, vol. 0484, 1-8.
- Yamada, T. *et al.* (2001). Reflection Loss Analysis by Optical Modeling of PV module. *Solar Energy Materials and Solar Cells*, vol. 67, 405–413.